National Technical University of Athens
School of Mechanical Engineering
Department of Mechanical Design & Automatic Control
Machine Design Laboratory

Analysis and patient-specific optimization of 3D printed scaffolds for guided regeneration of large femoral osseous defects

Diploma Thesis

Pelekis Matthaios

Supervisor: Professor Vasilios Spitas

Athens, 2024

Εθνικό Μετσόβιο Πολυτεχνείο
Σχολή Μηχανολόγων Μηχανικών
Τομέας Μηχανολογικών Κατασκευών & Αυτομάτου Ελέγχου
Εργαστήριο Στοιχείων Μηχανών

Ανάλυση και βελτιστοποίηση τρισδιάστατα εκτυπωμένων ικριωμάτων για την εξατομικευμένη αποκατάσταση μεγάλων οστικών ελλειμάτων μηριαίου

Διπλωματική Εργασία

Πελέκης Ματθαίος

Επιβλέπων: Καθηγητής Βασίλειος Σπιτάς

Αθήνα, 2024

Acknowledgements

I would like to express my sincere gratitude to my supervisor, Professor Vasilios Spitas, for his guidance and expertise in the fields of mechanical design and biomechanics, which have been invaluable to my thesis work. His advice and support throughout this project have been instrumental in its completion.

Special thanks are due to my project coordinators, Panagiotis Ntakos and Christos Kalligeros, whose dedicated involvement and exceptional problem-solving skills were fundamental to the success of my project. Their consistent readiness to provide insightful advice and resolve issues daily enriched my research experience and contributed significantly to my thesis.

I also appreciate the contributions of Dr. Athanasios Foukas, whose expertise in the medical aspects was indispensable. His guidance was always timely and profoundly influenced the quality of my work.

I would also like to thank my good friend and colleague, Alexandros Manios. We have collaborated on numerous projects throughout our studies. His support and motivation have been vital, encouraging me to engage in group projects that have significantly enhanced my knowledge and skills.

Lastly, my heartfelt thanks go to my partner, Ioanna, and my family—Manolis, Eirini, and Maria—for their support and understanding throughout my academic pursuits. Their encouragement has been essential to my studies.

Thank you all for your contributions and support, which have been vital to the completion of this thesis.

Solemn declaration for plagiarism and copyright theft

I have read and understood the rules for plagiarism and how to properly cite the sources contained in the Diploma Thesis writing guide. I declare that, as far as I know, the content of this Thesis is the product of my own work and there are references to all the sources I have used.

The views and conclusions contained in this Thesis are those of the author and should not be construed as representing the official positions of the School of Mechanical Engineering or the National Technical University of Athens.

Pelekis Matthaios

Table of Contents

Acknowledgements 4
Solemn declaration for plagiarism and copyright theft 5
Table of Contents 6
Table of Figures 9
List of Tables 13
Abstract 14
Περίληψη 15
Nomenclature, Greek Letters and Abbreviations 16
1. Introduction 19
2. Literature Review 21
2.1. Overview of Femoral Bone Defects 21
2.1.1. Structural Hierarchy and Composition of the Femoral Bone 21
2.1.2. Proximal Femoral Fractures 22
2.1.3. Femoral Shaft Fractures 24
2.1.4. Distal Femoral Fractures 26
2.1.5. Paprosky Classification of Bone Fractures 28
2.1.6. Causes and Epidemiology of Femoral Bone Fractures 30
2.2. Bone Fracture Healing Process 31
2.3. Conventional Treatment Methods 32
2.3.1. Femoral Plate Technologies 32
2.3.2. Femoral Nailing Techniques 37
2.3.3. Synergistic Integration of Femoral Plates and Nails 41
2.3.4. Limitations of Conventional Methods 42
2.4. Role of 3D Printing in Bone Regeneration 43
2.4.1. 3D Printing Technologies 43
2.4.2. 3D Printed Bone Scaffolds and TPMS Microarchitectures 44

2.4.3. Materials Used in 3D Printed Bone Scaffolds 47
2.4.4. Advantages over Traditional Methods 49
2.5. Homogenization in Composite Materials 50
2.6. Optimal Environment for Osteogenesis 51
2.6.1. Ideal Porosity Ranges 52
2.6.2. Ideal Strain Ranges 54
3. Homogenization Techniques in Scaffold Analysis 57
3.1. Robustness of Homogenization Softwares 57
3.1.1. Deterministic Homogenization: nTopology vs ANSYS Material Designer 57
3.1.2. Evaluation of Homogenization on Deterministic Lattices 63
3.2. Homogenization of Voronoi Stochastic Lattices 65
3.2.1. Materials Employed for Voronoi Homogenization 65
3.2.2. Field Driven Design and Homogenization Strategy 66
3.2.3. Indicative Detailed Results of Voronoi Homogenization at 80% Porosity 77
3.2.4. Summarized Voronoi Homogenization Results & Diagrams for 50-99% Porosities 82
3.3. Yield Stress of Voronoi Homogenized Materials 91
3.3.1. Analysis of Yield Stress in Ti-6Al-4V Voronoi Lattices 91
3.3.2. Yield Stress Plane Fit Assessment for Different Material Voronoi Lattices 93
4. Computer Aided Design of Bone and Implants 97
4.1. Porous Scaffold and Brackets 97
4.2. Retrograde Intramedullary Nail 99
4.3. Distal Femur Plate 100
4.4. Real Case Scenario CAD 101
5. Finite Element Analyses and Scaffold Optimization 102
5.1. Model Setup 102

5.1.1. Gait Analysis 102
5.1.2. FEM Boundary Conditions 105
5.1.3. FEM Mesh and Contacts 107
5.2. Scaffold Optimization Algorithm 108
5.2.1. Setup and Hyperparameters 108
5.2.2. Algorithm Functionality 111
5.3. Optimization Results and Discussion 114
5.3.1. Properties and Variable Parameters in Parametric Runs 114
5.3.2. Detailed Optimization Results of Benchmark Conditions 115
5.3.3. Summarized Parametric Weights Optimization Results 120
5.3.4. Parametric Fracture Gap Optimization Results 122
5.3.5. Summarized Parametric Reinforcement Methods Optimization Results 124
5.3.6. Real Case Scenario Detailed Optimization Results 126
5.4. Constraints and Limitations of the Optimization Methodology 130
6. Conclusion and Future Work 132
References 134
Appendix A.1 – Optimization Code 141
Appendix A.2 – Results Visualization Code 142

Table of Figures

Figure 1: Hierarchical structure of bone from macroscale to nanoscale 21
Figure 2: (a) The anterior and (b) the posterior surface of the proximal right femur .22
Figure 3: Fracture classification of proximal femur trochanteric region AO/OTA-31A23
Figure 4: Femoral bone.....24
Figure 5: Winquist classification of femoral shaft fractures 25
Figure 6: Spiral fracture of the femoral shaft.....26
Figure 7: (a) Anterior and (b) posterior surface of the distal right femur.....26
Figure 8: Seinsheimer Classification of Distal Femoral Fractures 27
Figure 9: Paprosky classification of femoral bone loss 28
Figure 10: Aetiology of fractures according to gender 30
Figure 11: Possible bone fracture formation due to tumor 31
Figure 12: Stages of Bone Fracture Healing 32
Figure 13: FEM of human femoral shaft with the application of a bone plate [17] 33
Figure 14: Femoral shaft plate implant 34
Figure 15: Stryker AxSOS 3 Ti distal lateral femur plating system 35
Figure 16: Treatment of distal femur fractures with locking plates 36
Figure 17: Articulated tension device.....36
Figure 18: Migration of a retrograde nail onto the knee joint after fracture of distal interlocking screws. A: Anteroposterior view. B: Lateral view. C: Merchant view 37
Figure 19: R/AFN intramedullary nailing system.....39
Figure 20: Percutaneous Insertion Handle for LFN and R/AFN. (a) Normal handle. (b) Handle for obese patients 40
Figure 21: R/AFN Arm for Proximal Aiming Device 40
Figure 22: Anteroposterior (A) and lateral (B) views demonstrate interlocking the Synthes (West Chester, PA) distal femur lateral locking plate (variable angle locks compression of condylar plate 4.5/5.0) and retrograde nail system.....41
Figure 23: Post operative radiographs of a ppatient managed with nail-plate fixation 42
Figure 24: Schematic of 3D printing of metal products with microporous structure and its application in biomedicine 44
Figure 25: Micro- and macroarchitectures of the scaffolds used in Maevskaia et al. bone augmentation model.....45

Figure 26: Solid Voronoi diagram generate process (A) probability sphere; (B) random seeds; (C) Voronoi diagram; (D) scaling; (F) generating scaffold; (G) Smooth treatment.....46
Figure 27: Regular method of modeling bionic structure via Voronoi diagram 46
Figure 28: Construction of porous gradient artificial bone: (1) Surface offset, (2) Spherical regions at UV isocurve intersections, (3) Irregular lattice formation.....47
Figure 29: A section of a 2D periodic microstructure consisting of two materials (white and black). The red line encloses a square unit cell, the blue a rectangular unit cell, and the green a parallelogram unit cell. 50
Figure 30: Defining parameters of Voronoi lattice. (a) Point spacing; (b) Strut radius52
Figure 31: Various porosities of voronoi lattices.....52
Figure 32: Boundaries of the biophysical stimuli for tissue formation 55
Figure 33: Cubic geometry with internal void structure by Chauhan et al. 57
Figure 34: Result of unit cell homogenization by Chauhan et al. at nTopology 58
Figure 35: Re-entrant honeycomb cell, showing geometric parameters 59
Figure 36: Result of unit cell homogenization by Sorohan et al. at nTopology 60
Figure 37: Honeycomb lattices under examination 63
Figure 38: Homogenization result for single honeycomb REV.....63
Figure 39: Homogenization result for four honeycomb REVs.....64
Figure 40: Homogenization result for nine honeycomb REVs 64
Figure 41: Bone tissue properties of each stage according to Kim et al. 65
Figure 42: nTopology limitation for 2-material homogenization.....66
Figure 43: Rectangular cell map alongside middle point 67
Figure 44: Thickness ramp using a point 68
Figure 45: Field driven design: thickness of the cell map on the defined point 68
Figure 46: Field driven design: thickness of the cell map at the edge 69
Figure 47: Field driven design: thickness of the cell map betwween the defined point and the edge.....69
Figure 48: Finalized implicit body based on ramped thickness.....70
Figure 49: Rectangular cell map alongside defined body 70
Figure 50: Thickness ramp using a volumetric body 71
Figure 51: Field driven design: thickness of the cell map on the volumetric body.....71
Figure 52: Field driven design: thickness of the cell map away from the volumetric body.....72
Figure 53: Indicative 60% porosity lattice alongside bounding box for field driven design.....72

Figure 54: Young's modulus ramp using a lattice....73
Figure 55: Field driven design: Young's modulus near the lattice at section view 73
Figure 56: Field driven design: Young's modulus away from the lattice at section view 74
Figure 57: Poisson's ratio and density ramps using the lattice....74
Figure 58: Field driven design: Poisson's ratio near the lattice at section view 75
Figure 59: Field driven design: Poisson's ratio away from the lattice at section view 75
Figure 60: Field driven design: Density near the lattice at section view....76
Figure 61: Field driven design: Density away from the lattice at section view....76
Figure 62: Voronoi lattice at 80% porosity....77
Figure 63: Granulation and Ti-6Al-4V lattice homogenized material at 80% porosity; Seed number 1 78
Figure 64: Granulation and Ti-6Al-4V lattice homogenized material at 80% porosity; Seed number 2 79
Figure 65: Granulation and Ti-6Al-4V lattice homogenized material at 80% porosity; Seed number 3 79
Figure 66: Cartilage and Ti-6Al-4V lattice homogenized material at 80% porosity 80
Figure 67: Immature and Ti-6Al-4V lattice homogenized material at 80% porosity ...81
Figure 68: Mature and Ti-6Al-4V lattice homogenized material at 80% porosity 81
Figure 69: Relationship between porosity and point spacing of seed points 84
Figure 70: Stiffness moduli as a function of porosity for the three granulation seed numbers....85
Figure 71: Relative standard deviation between varying seed number Voronoi lattices at granulation stage....88
Figure 72: Directional young's moduli as a function of porosity and tissue stage....89
Figure 73: Compression test results at Ti-6Al-4V Voronoi lattices....91
Figure 74: Plane fit of yield strength versus porosity and seed points in Voronoi lattices 92
Figure 75: Stress-strain curves for the biomimetic PLA Voronoi models....94
Figure 76: Number of seed points for 83% porosity according to Yue et al. 95
Figure 77: Experimental compressive stress-strain curves for AZ91 Voronoi lattices.95
Figure 78: Porous scaffold implant with brackets....97
Figure 79: Femoral bone with porous scaffold implant and brackets 98
Figure 80: Femoral bone with retrograde intramedullary nail 99
Figure 81: Femoral bone with distal femur plate.... 100
Figure 82: CAD of real case scenario and scaffold 101

Figure 83: Basic terminology describing the gait cycle 102
Figure 84: The hip joint is a ball-in-socket and allows movement in the transverse, sagittal and frontal 103
Figure 85: Muscles of the thigh - anterior view 104
Figure 86: The applied joint reaction and muscle forces 105
Figure 87: FEM Boundary Conditions for the 80kg benchmark weight 106
Figure 88: Femur FEM mesh 107
Figure 89: Flowchart for algorithm main process loop 111
Figure 90: Flowchart for region split and porosity initialization 112
Figure 91: Flowchart for assessing region eligibility for promotion and porosity change 113
Figure 92: Stiffness map of benchmark conditions 115
Figure 93: Scaffold strain contours - benchmark conditions (granulation-cartilage-immature-mature from top to bottom) 116
Figure 94: Scaffold stress contours - benchmark conditions (granulation-cartilage-immature-mature from top to bottom) 117
Figure 95: Stress contours near brackets at granulation stage 119
Figure 96: Parametric patient weight results 120
Figure 97: Parametric fracture gap results 122
Figure 98: Stiffness maps of parametric reinforcement methods 124
Figure 99: Stiffness map of real case scenario 126
Figure 100: Scaffold strain contours – real case (granulation-cartilage-immature-mature from top to bottom) 127
Figure 101: Scaffold stress contours – real case (granulation-cartilage-immature-mature from top to bottom) 128
Figure 102: Stress contours near brackets at granulation stage at real case scenario 129

List of Tables

Table 1: Ideal porosity range for osteogenesis 53
Table 2: Boundaries of the biophysical stimuli for tissue formation according to the various mechano-regulation algorithms investigated, including the three algorithms with only one stimulus 55
Table 3: Summarized strain boundaries at each stage 56
Table 4: Material properties used in paper by Chauhan et al. 58
Table 5: Chauhan et al unit cell homogenization results - ANSYS Material Designer..59
Table 6: Summarized homogenization results by Chauhan et al. 59
Table 7: Geometrical dimensions of re-entrant honeycomb cell by Sorohan et al. 60
Table 8: Material properties used in paper by Sorohan et al. 60
Table 9: Summarized homogenization results regarding the study by Sorohan et al. 62
Table 10: Bone tissue properties of each stage according to Ghiasi et al. 65
Table 11: Final bone tissue properties 66
Table 12: Ti-6Al-4V material properties 66
Table 13: Characteristics of the homogenized materials 82
Table 14: Properties of the biomimetic PLA Voronoi structures by Efstathiadis et al. 93
Table 15: Material properties of AZ91 94
Table 16: Properties and geometrical parameters of AZ91 Voronoi lattices.....95
Table 17: Components of the forces acting on the femur 105
Table 18: Mesh size and conforming method per model part..... 107
Table 19: Tissue stage naming scheme 108
Table 20: Benchmark conditions and variable parameters in parametric runs..... 114

Abstract

This thesis introduces a new method for developing and optimizing 3D-printed porous scaffolds specifically tailored for the repair of significant bone defects in the femur. The approach involves creating patient-specific scaffolds that closely match both the anatomical and mechanical characteristics of human bone. By utilizing Voronoi lattice models, this research simulates porous structures that replicate bone's natural cellular architecture, resulting in scaffolds that are both biocompatible and conducive to bone growth. A crucial element of this work is the application of homogenization theory to fine-tune the scaffold's mechanical attributes like stiffness and porosity, ensuring they meet necessary mechanical demands and closely match the properties of human bone. Additionally, the thesis introduces an automated algorithm that optimizes the properties of these scaffolds through mechanical simulations and iterative design adjustments. The automation of this process improves both the efficiency and consistency of producing customized bone scaffolds. The outcomes of this research indicate that 3D-printed porous scaffolds, optimized through these innovative methods, offer substantial potential for advancing the treatment of large bone defects in the femur.

Περίληψη

Η παρούσα μελέτη παρουσιάζει μια πρωτοπόρα μέθοδο για την ανάπτυξη και τη βελτιστοποίηση τρισδιάστατα εκτυπωμένων πορωδών ικριωμάτων για την εξατομικευμένη αποκατάσταση μεγάλων οστικών ελλειμάτων μηριαίου. Η προσέγγιση περιλαμβάνει τη δημιουργία εξατομικευμένων ικριωμάτων, τα οποία ανταποκρίνονται στενά τόσο στα ανατομικά όσο και στα μηχανικά χαρακτηριστικά του ανθρώπινου οστού. Χρησιμοποιώντας μοντέλα πλέγματος Voronoi, η έρευνα αυτή προσομοιώνει πορώδεις δομές που αναπαράγουν τη φυσική κυτταρική αρχιτεκτονική του οστού, με αποτέλεσμα να δημιουργούνται ικριώματα που είναι βιοσυμβατά και ευνοούν την ανάπτυξη του οστού. Ένα κρίσιμο στοιχείο αυτής της διπλωματικής εργασίας είναι η εφαρμογή της θεωρίας ομογενοποίησης για τη λεπτομερή ρύθμιση των μηχανικών χαρακτηριστικών του ικριώματος, όπως η το μέτρο ελαστικότητας και το πορώδες, διασφαλίζοντας ότι πληρούν τις απαραίτητες μηχανικές απαιτήσεις ενώ ταιριάζουν παράλληλα με τις ιδιότητες του ανθρώπινου οστού. Επιπλέον, η έρευνα αυτή εισάγει έναν αυτοματοποιημένο αλγόριθμο που βελτιστοποιεί τις ιδιότητες αυτών των ικριωμάτων μέσω μηχανικών προσομοιώσεων και επαναληπτικών προσαρμογών σχεδιασμού. Η αυτοματοποίηση της διαδικασίας αυτής βελτιώνει τόσο την αποτελεσματικότητα όσο και τη συνέπεια της παραγωγής προσαρμοσμένων οστικών ικριωμάτων. Τα αποτελέσματα της έρευνας δείχνουν ότι τα τρισδιάστατα εκτυπωμένα πορώδη ικριώματα, βελτιστοποιημένα μέσω της προτεινόμενης μεθόδου, προσφέρουν σημαντικές δυνατότητες για την προώθηση της θεραπείας μεγάλων οστικών ελλειμμάτων στο μηριαίο οστό.

Nomenclature, Greek Letters and Abbreviations

Nomenclature

Symbol	**Description**	**SI Units**
b	Depth	m
C	Stiffness matrix	Pa
D$strut$	Strut diameter	mm
E	Young's Modulus	Pa
E_{ijkl}^{H}	Elasticity tensor	Pa
E_{pqrs}	Local stiffness tensor	Pa
e	Deviation	%
F_{abd}	Abductors force	N
F_{lp}	Iliopsoas force	N
F_{vl}	Vastus lateralis force	N
G	Shear modulus	Pa
K	Stiffness matrix	Pa
$L_{fracture}$	Fracture gap length	m
l, h	Length	m
N	Number of seed points	$-$
R_{strut}	Strut radius	mm
S	Compliance matrix	Pa^{-1}
T	Simulation run time	s
t	Thickness	m

V	Volume	m^3
W	Patient weight	kg
X	X direction	–
Y	Y direction	–
Z	Z direction	–

Greek Letters

Symbol	**Description**	**SI Units**
ε	Mechanical strain	–
ϵ_{ij}	Locally varying strain fields	–
ϵ_{ij}^0	Prescribed macroscopic strain fields	–
θ	Angle	rad
λ, μ	Lamé's parameters	–
μ_x	Sample mean	–
ν	Poisson's ratio	–
ρ	Density	kg/m^3
σ	Mechanical stress	Pa
σ_x	Standard deviation	–
σ_y	Yield strength	Pa
Φ	Porosity	%

Abbreviations

Symbol	**Description**	**SI Units**
CCE	Convergence Cube Edge	mm
FEA	Finite Element Analysis	$-$
FEM	Finite Element Model	$-$
JRF	Joint Reaction Force	$-$
MTA	Motor Traffic Accident	$-$
PS	Point Spacing	mm
REV	Representative Volume Element	$-$
RF	Relaxation Factor	$\%$
RTA	Road Traffic Accident	$-$

1. Introduction

Bone defects represent significant challenges within orthopedic medicine, fundamentally due to the essential role of the skeletal system in biomechanical support, protection of vital organs, and facilitation of mobility. The treatment of bone defects, particularly those occurring in load-bearing areas such as the distal femur, is critical due to the complex mechanical and biological demands placed on these regions. Distal femoral defects are among the most challenging to manage effectively because of the femur's crucial role in weight-bearing and its exposure to high biomechanical forces during movement. The are also one of the most common ones, due to several factors, such as the prevalence of high-energy trauma (e.g., vehicular accidents), the susceptibility of the elderly to falls, and the area's involvement in various types of cancer [1]. These defects pose significant treatment challenges, often requiring complex interventions and long time periods in order to fully restore function and prevent disability.

Bone regeneration is a natural process where the body replaces damaged bone tissue with new bone. This involves an initial inflammatory response, followed by the formation of new bone tissue through cellular processes.

The traditional approaches to managing these defects involve the use of orthopedic devices such as plates and nails [2], [3]. Plates provide rigid support and are used to bridge gaps in the bone, ensuring alignment and stability during the healing process. Nails, inserted into the bone marrow cavity, offer internal support and are typically used for long bone fractures. While effective, these methods can have limitations, including risks of infection, improper bone healing, and the need for removal surgeries once healing has occurred.

Innovations in bone regeneration have led to the use of 3D-printed porous scaffolds that mimic the structure of natural bone [4]. These scaffolds are designed based on the Voronoi lattice, a model that simulates the random, yet organized, cellular structure of bone tissue. The design of these scaffolds aims to facilitate the integration of the scaffold with natural bone, promoting vascularization and bone growth throughout the structure, which is critical for successful implantation and integration.

The concept of homogenization in materials science is particularly crucial in research areas that demand high computational resources [5]. Homogenization allows for the creation of a material with uniform properties by averaging the varied characteristics of composite materials. In the context of bone scaffolds, this process is essential for efficiently simulating the equivalent mechanical properties such as stiffness, density,

and porosity. This approach significantly reduces the computational resources by providing a simplified yet accurate representation of the scaffold's behavior under physiological conditions.

These lead to the more feasible development of patient-specific and optimized bone scaffolds. This would be beneficial to be done using automated methodologies and algorithms represents a significant advancement in personalized medicine. By tailoring the scaffold to the specific anatomical and functional requirements of each patient, these techniques promise improved outcomes, shorter recovery times, and reduced incidence of complications. Automation in the design and manufacturing processes enables the efficient production of these customized implants.

This thesis seeks to contribute to the field of biomechanical engineering by providing a novel, efficient, and patient-specific approach to the treatment of one of the most challenging scenarios in bone healing and regeneration. The primary objective is to develop, analyze and explore an automated method for the design and optimization of 3D-printed porous scaffolds in various scenarios, specifically in the context of treating large femoral osseous defects. By integrating patient-specific data, biomechanical analyses, and advanced manufacturing techniques, this work aims to create scaffolds that not only support effective bone regeneration but also adapt precisely to the mechanical demands and biological environment of the human body.

2. Literature Review

2.1. Overview of Femoral Bone Defects

2.1.1. Structural Hierarchy and Composition of the Femoral Bone

The femoral bone's structure spans from the macroscale to the nanoscale, displaying complex organization across varying magnifications. At the broadest level, the bone comprises trabecular (spongy) and cortical (compact) regions. The trabeculae within the spongy area form a network-like structure vital for stress absorption. Further examination reveals the osteon system in cortical bone, critical for remodeling and nutrient transport, consisting of concentric lamellae. Zooming in further, each lamella is made up of collagen fibers arranged in a helical pattern around a central canal, providing strength and flexibility. At the microscopic level, the bone consists of a collagen-mineral composite with tightly packed collagen and hydroxyapatite crystals, enhancing hardness and compression resistance. Each finer scale reveals more about the bone's resilience and biological complexity, essential for understanding its strength, susceptibility to disease, and repair mechanisms [6].

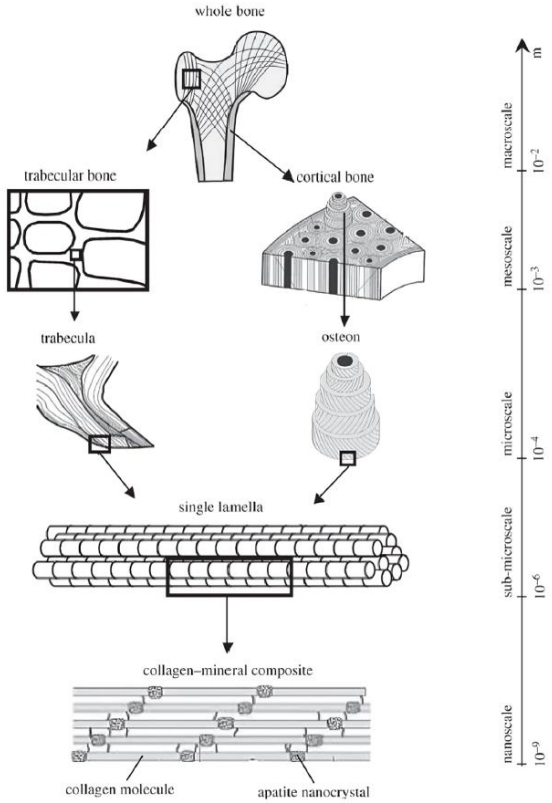

Figure 1: Hierarchical structure of bone from macroscale to nanoscale

Structurally, the femur is segmented into three distinct parts: the proximal end, the shaft, and the distal end. This article delves into the detailed anatomy of the femur, exploring its various attachments and bony landmarks, and discusses the clinical implications associated with it.

2.1.2. Proximal Femoral Fractures

The proximal end of the femur interacts with the acetabulum of the pelvis, forming the hip joint. This section of the femur includes several key components: the head and neck, along with two prominent projections known as the greater and lesser trochanters. Additionally, there are two bony ridges that link these trochanters: the intertrochanteric line on the anterior side and the trochanteric crest on the posterior side [7].

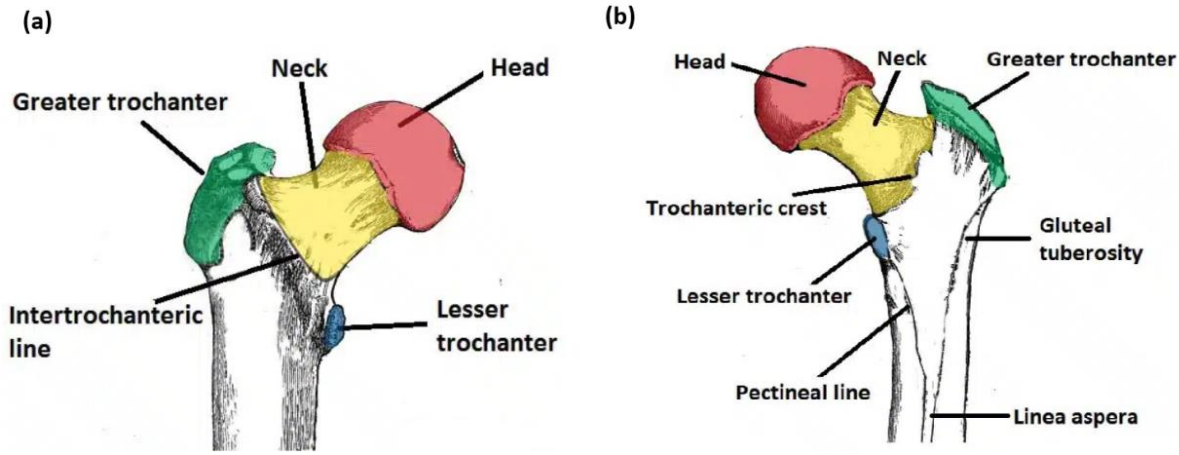

Figure 2: (a) The anterior and (b) the posterior surface of the proximal right femur

The proximal femoral bone regions include:

- **Head:** Fits into the acetabulum forming the hip joint, mostly covered with articular cartilage, except the fovea where the ligamentum teres attaches.
- **Neck:** Cylindrical, connects the head and shaft of the femur, oriented at approximately 135 degrees to allow significant hip joint mobility.
- **Greater Trochanter:** Prominent lateral bone projection near the neck, providing muscle attachments including the gluteus medius and piriformis. Susceptible to avulsion fractures.
- **Lesser Trochanter:** Located posteromedially below the neck-shaft junction, smaller than the greater trochanter, and serves as the attachment point for the iliopsoas muscle.

- **Intertrochanteric Line:** A ridge running inferomedially on the femur's anterior, linking the trochanters and providing attachment for the iliofemoral ligament and the hip joint capsule.
- **Intertrochanteric Crest:** A posterior ridge similar to the intertrochanteric line, featuring a quadrate tubercle where the quadratus femoris muscle attaches.

The AO/OTA classification system for fractures in the proximal femur trochanteric region (AO/OTA-31A) provides a detailed framework to categorize these injuries based on specific anatomical features and fracture characteristics. [8]. The classification features four types:

- **Type A1:** Simple two-part fractures. These involve minimal fragmentation and are generally considered stable.
- **Type A2:** Fractures with a lesser trochanter fragment and potentially additional posterior coronal fragments, indicating more complexity and typically associated with a higher risk of instability.
- **Type A3:** Characterized by reverse obliquity and transverse fractures, often involving complete lateral wall disruption, which significantly affects the structural integrity and stability.
- **Type A4:** The most severe category, involving medial wall comminution and loss of the anteromedial cortex, critical for load transmission and stability.

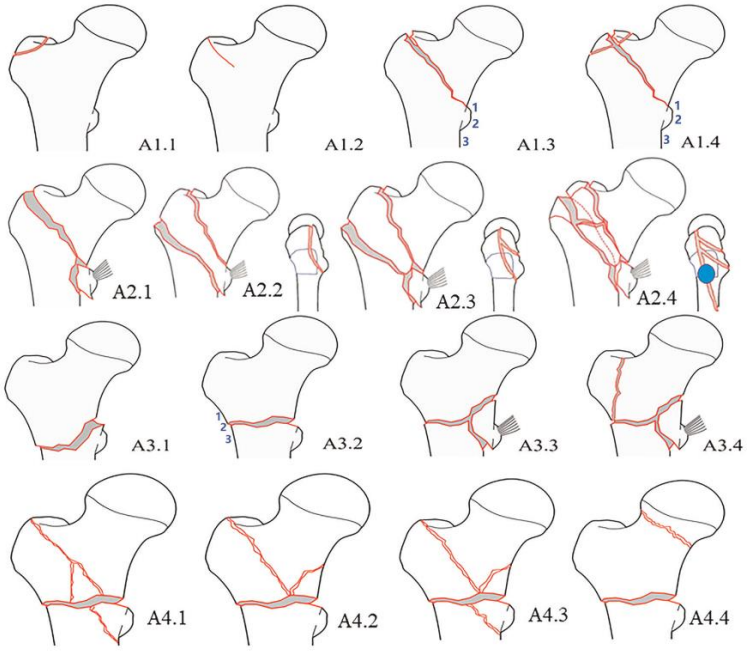

Figure 3: Fracture classification of proximal femur trochanteric region AO/OTA-31A

2.1.3. Femoral Shaft Fractures

The femoral shaft extends medially as it descends, aligning the knees closer to the body's center of gravity, thus enhancing stability. In its middle, the cross-sectional shape of the shaft is circular, tapering flatter towards the proximal and distal ends [7].

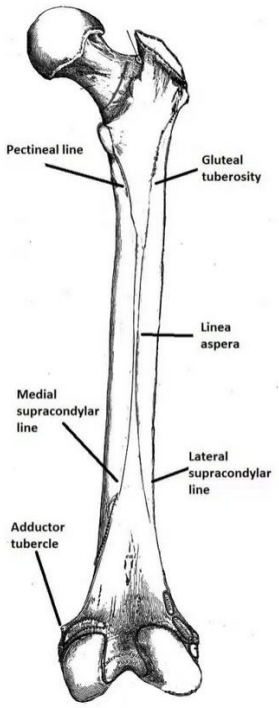

Figure 4: Femoral bone

The posterior aspect of the femoral shaft features raised, roughened strips of bone known as the linea aspera, which translates from Latin to 'rough line'. This structure bifurcates distally into the medial and lateral supracondylar lines, with the flat popliteal surface nestled between them. Towards the top, the medial edge of the linea aspera transitions into the pectineal line, while the lateral edge forms the gluteal tuberosity, which serves as the attachment point for the gluteus maximus muscle. Towards the bottom, the linea aspera expands and underpins the floor of the popliteal fossa, with its borders continuing as the medial and lateral supracondylar lines. The medial line concludes at the adductor tubercle, where the adductor magnus muscle attaches.

According to the Winquist Classification of Femoral Shaft Fractures [9], these can be divided into 5 distinct types.

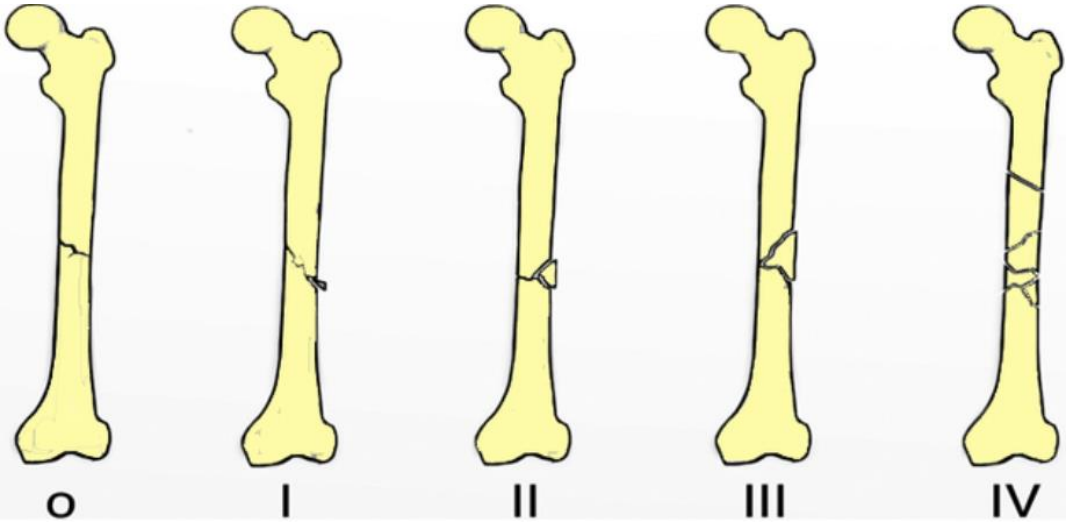

Figure 5: Winquist classification of femoral shaft fractures

- **Type O:** Features either no comminution or a minor butterfly fragment constituting less than 25% of the bone's width.
- **Type I:** Includes a small butterfly fragment, also making up less than 25% of the bone's width.
- **Type II:** Characterized by a butterfly fragment that comprises 50% or less of the bone's width.
- **Type III:** Involves a comminuted structure with a substantial butterfly fragment exceeding 50% of the bone's width.
- **Type IV:** Exhibits severe comminution, affecting an entire segment of the bone (known as segmental comminution).

Fractures along the femoral shaft are generally the result of high-energy trauma but may also occur in elderly individuals due to low-energy falls. Such fractures are frequently spiral in nature, leading to leg shortening as the bone fragments are displaced by the pulling forces of the attached muscles. Given the typical high-energy nature of these injuries, adjacent soft tissues may also sustain damage. Important neurovascular structures like the femoral nerve and artery are particularly vulnerable. A closed fracture of the femoral shaft can lead to significant hemorrhage, potentially resulting in the loss of 1000 to 1500 milliliters of blood.

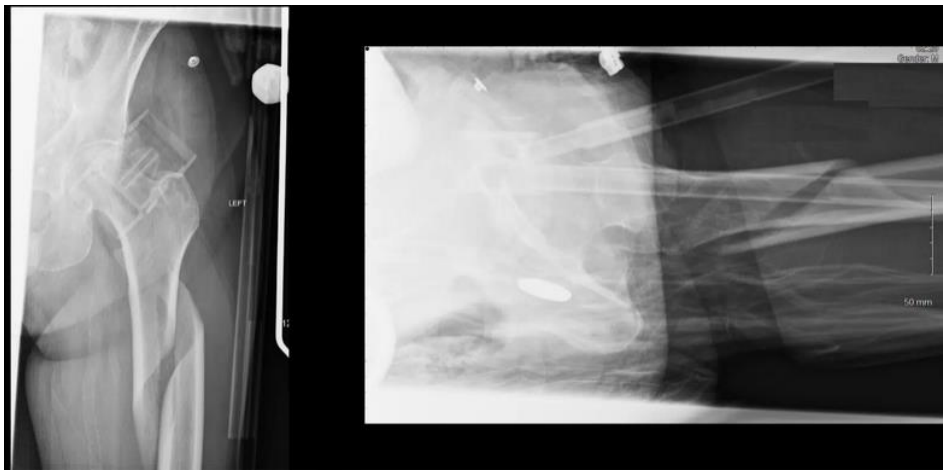

Figure 6: Spiral fracture of the femoral shaft

2.1.4. Distal Femoral Fractures

The distal portion of the femur features the medial and lateral condyles, which engage with the tibia and patella to form the knee joint [7].

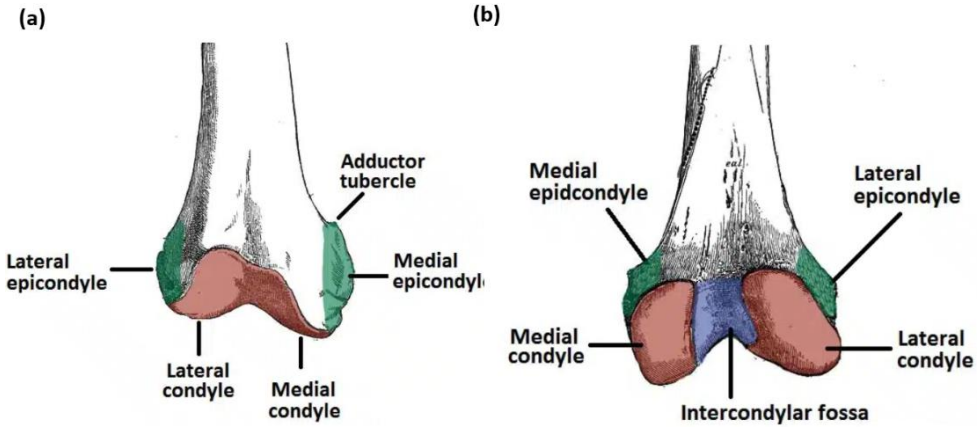

Figure 7: (a) Anterior and (b) posterior surface of the distal right femur

- **Medial and Lateral Condyles:** These are rounded protrusions found at the femur's end. The posterior and inferior surfaces of these condyles interact with the tibia and the menisci of the knee, whereas the anterior surfaces connect with the patella. The lateral condyle, being more pronounced, helps in stabilizing the patella against natural lateral shifts; conversely, a less prominent condyle may lead to an increased risk of patellar dislocation.
- **Medial and Lateral Epicondyles:** These are bony projections located on the non-articulating portions of the condyles. The medial epicondyle is notably

larger than the lateral. The knee's medial and lateral collateral ligaments originate from these respective epicondyles.

- **Intercondylar Fossa:** Situated on the posterior aspect of the femur between the two condyles, this deep groove accommodates facets that serve as attachment points for the knee's intracapsular ligaments; the anterior cruciate ligament (ACL) connects to the medial side of the lateral condyle, and the posterior cruciate ligament (PCL) attaches to the lateral side of the medial condyle.

According to the Seinsheimer Classification of Femoral Condylar Fractures, these fractures can be classified as illustrated in Figure 8 [10].

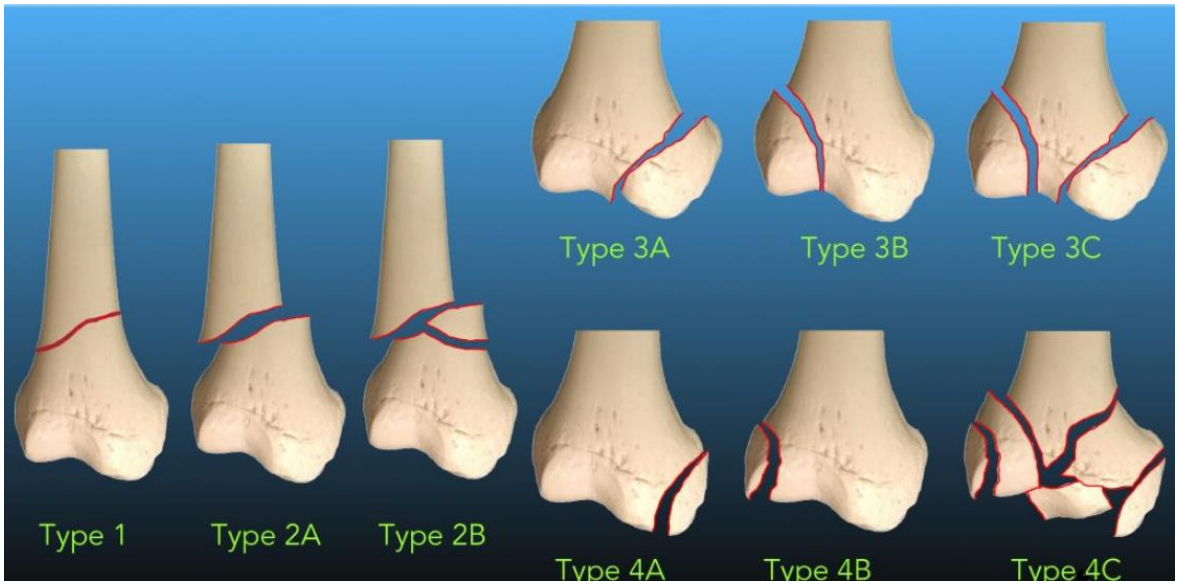

Figure 8: Seinsheimer Classification of Distal Femoral Fractures

- **Classification 1:** Non-displaced fractures.
- **Classification 2A:** Bifragmentary fractures involving the patellofemoral articular surface, common in osteoporotic patients.
- **Classification 2B:** Comminuted fractures affecting the patellofemoral articular surface, also seen in osteoporotic patients.
- **Classification 3A:** Fractures of the medial condyle extending into the intercondylar notch, affecting the patellofemoral but not the femorotibial articular surface.
- **Classification 3B:** Fractures of the lateral condyle extending into the intercondylar notch, similarly involving the patellofemoral but not the femorotibial articular surface.

- **Classification 3C:** Fractures involving both condyles extending into the intercondylar notch, impacting the patellofemoral but not the femorotibial surface.
- **Classification 4A:** Fractures of the medial condyle extending to the femorotibial articular surface.
- **Classification 4B:** Fractures of the lateral condyle extending to the femorotibial articular surface.
- **Classification 4C:** Complex, comminuted fractures involving any combination of the above-described patterns.

2.1.5. Paprosky Classification of Bone Fractures

A bone defect occurs when there is an absence of bone in places where it is normally found. Such defects can result from trauma, tumors, or infections such as osteomyelitis. The surgical repair of these defects poses a considerable challenge to orthopedic surgeons. Often, bone defects resulting from trauma or the surgical removal of infected tissue are associated with significant injuries to the surrounding soft tissues, including muscles, tendons, and joints.

Furthermore, in treating the bone defect, surgeons must also consider the adjacent soft tissues to optimize the functional outcome for the patient. Achieving union in large bone defects can be challenging, potentially leading to complications such as deformities, infections, and differences in limb length. Addressing these issues is crucial during the treatment process.

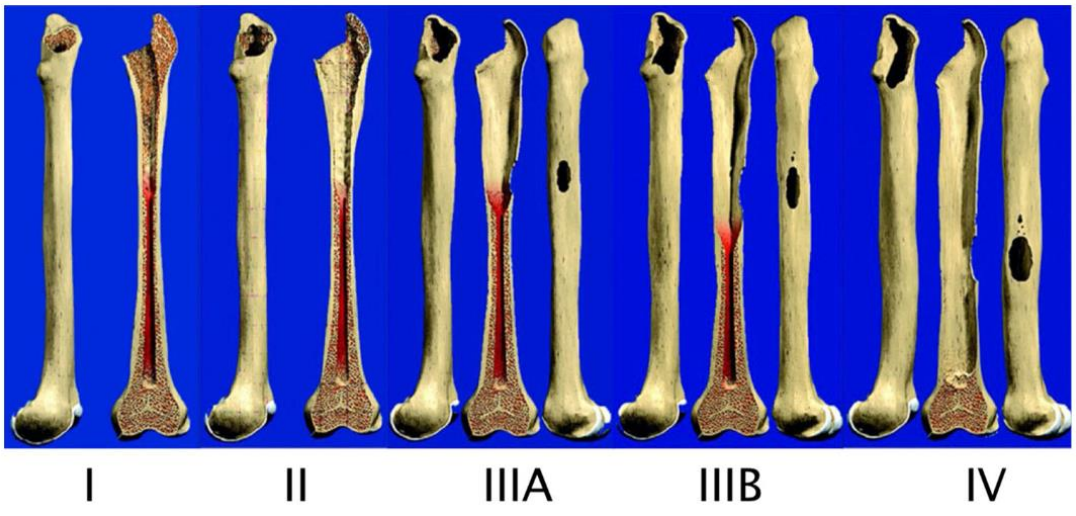

Figure 9: Paprosky classification of femoral bone loss

The Paprosky classification of femoral bone loss categorizes the severity and location of bone defects in the femur, which is crucial for planning surgical interventions. This system identifies several types of femoral bone loss, each corresponding to specific anatomical and structural challenges [11].

- **Type I:** This type involves minimal metaphyseal bone loss while maintaining the proximal femoral geometry. It generally occurs following the removal of an uncemented implant with a narrow metaphyseal design or an implant with limited proximal in-growth potential. These defects can often be managed with cylindrical extensively porous-coated stems or tapered proximally porous-coated stems if sufficient metaphyseal bone remains for osteointegration.
- **Type II:** Characterized by notable damage to the proximal metaphyseal bone which may not support a proximally fitting implant nor allow reliable proximal biologic fixation. This type is often seen after the removal of a cemented femoral implant or a proximally fitting stem with a broad femoral geometry. The recommended treatment usually involves the use of a femoral implant that engages the diaphysis with an ongrowth or porous ingrowth surface.
- **Type III:** Severe cases where the proximal metaphysis is completely unsupportive and the endosteal bone is highly deficient or absent, typically resulting from chronically loose femoral stems or posttraumatic conditions. Type III is subdivided into:
    - **Type IIIA:** Where at least 6 cm of diaphyseal scratch-fit (contact between cortical bone and stem) is achievable, allowing for certain types of extensively porous-coated stems.
    - **Type IIIB:** Less than 6 cm of diaphyseal scratch-fit is possible due to more extensive bone loss, usually necessitating the use of tapered stems designed for rotational stability and possibly requiring different surface finishes for successful implantation.
- **Type IV:** Represents the most severe form of bone loss with extensive damage to both metaphyseal and diaphyseal regions and a non-supportive isthmus. This type often involves significant ectasia (expansion) of the femoral canal with substantial cortical thinning, making uncemented fixation unreliable. Options for reconstruction are limited and may include proximal femoral replacements or impaction grafting with a cemented stem.

2.1.6. Causes and Epidemiology of Femoral Bone Fractures

Characterized by an absence or loss of bone tissue in the femur, these defects can arise from various causes such as trauma, infections or tumors. Road traffic accidents also contribute notably to these injuries. The causes can sometimes even extend to gunshot wounds. Younger individuals are most commonly affected by femur shaft fractures, often resulting from high-energy traumas like traffic accidents. Conversely, in the elderly population, falls from standing height are the predominant cause, leading typically to proximal femur fractures. This bifurcation in the mechanism of injury with age underscores the varied etiological factors contributing to femur fractures across different life stages [12].

Road traffic accidents (RTAs) and falls as the primary causes of femur fractures. RTAs predominantly affect males under the age of 30, whereas falls are more common among females and the elderly over 50. Mid-shaft femur fractures are the most frequently diagnosed type in both males and females [13].

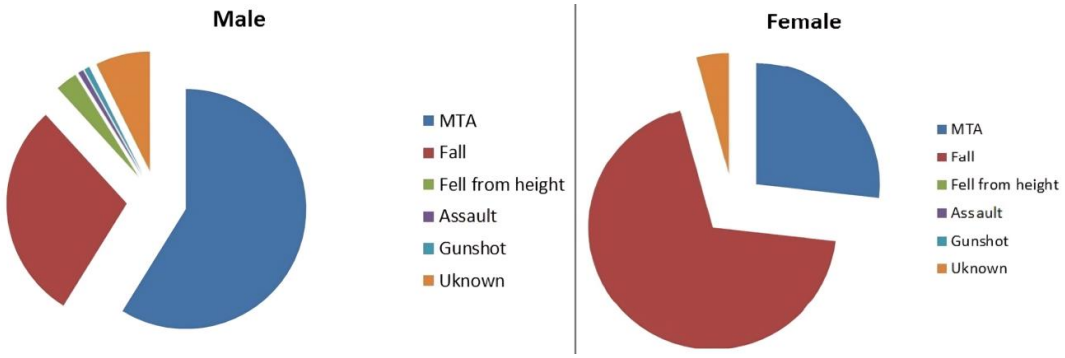

Figure 10: Aetiology of fractures according to gender

Bone tumors, both benign and malignant, can lead to significant bone defects due to the destructive nature of tumor growth within the bone structure. As tumors develop, they can disrupt the normal bone architecture by replacing healthy bone tissue with abnormal cells. This process not only weakens the bone, making it susceptible to fractures, but can also interfere with the bone's blood supply, further impairing bone health and integrity. In cases of malignant tumors like osteosarcoma or metastatic cancers, the rapid growth of cancerous cells exacerbates the extent of bone damage, often leading to extensive bone loss that poses considerable challenges in surgical management and reconstruction. These defects significantly affect the mechanical stability and functional capacity of the bone, necessitating complex interventions to restore form and function [14].

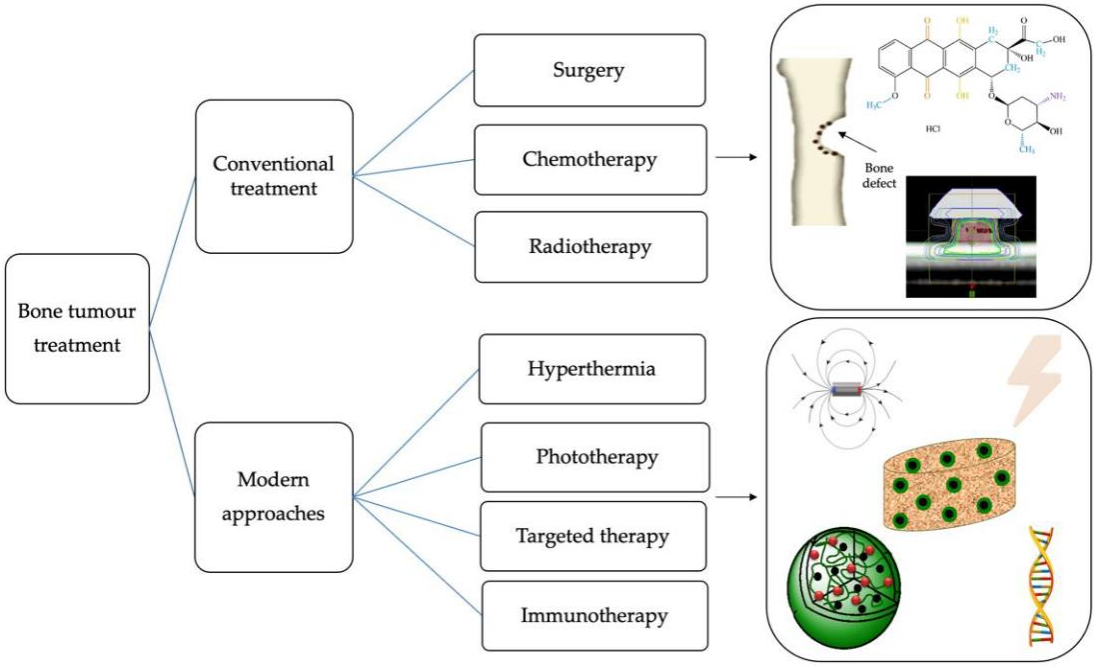

Figure 11: Possible bone fracture formation due to tumor

2.2. Bone Fracture Healing Process

Bone fracture healing is a complex regenerative process aimed at restoring the damaged bone to its pre-injury state. The healing process progresses through several distinct but overlapping stages [15], [16]:

- **Hematoma Formation:** Immediately post-fracture, disrupted blood vessels at the site lead to a hematoma, which forms a clot that lays the foundation for healing.
- **Granulation Tissue Formation:** Within about two weeks, platelets and inflammatory cells stimulate the formation of granulation tissue and initiate angiogenesis, setting the stage for subsequent healing phases.
- **Bony Callus Formation:** Mesenchymal stem cells differentiate into chondrocytes, creating a fibrocartilaginous bridge across the fracture site.
    - The initial *"soft callus"* gradually transitions to a *"hard callus"* through endochondral ossification
- **Bone Remodeling:** Over months to years, the newly formed bone is remodeled. Osteoclasts resorb old or damaged bone, and osteoblasts deposit new bone, refining the structure and adapting it to mechanical stress.

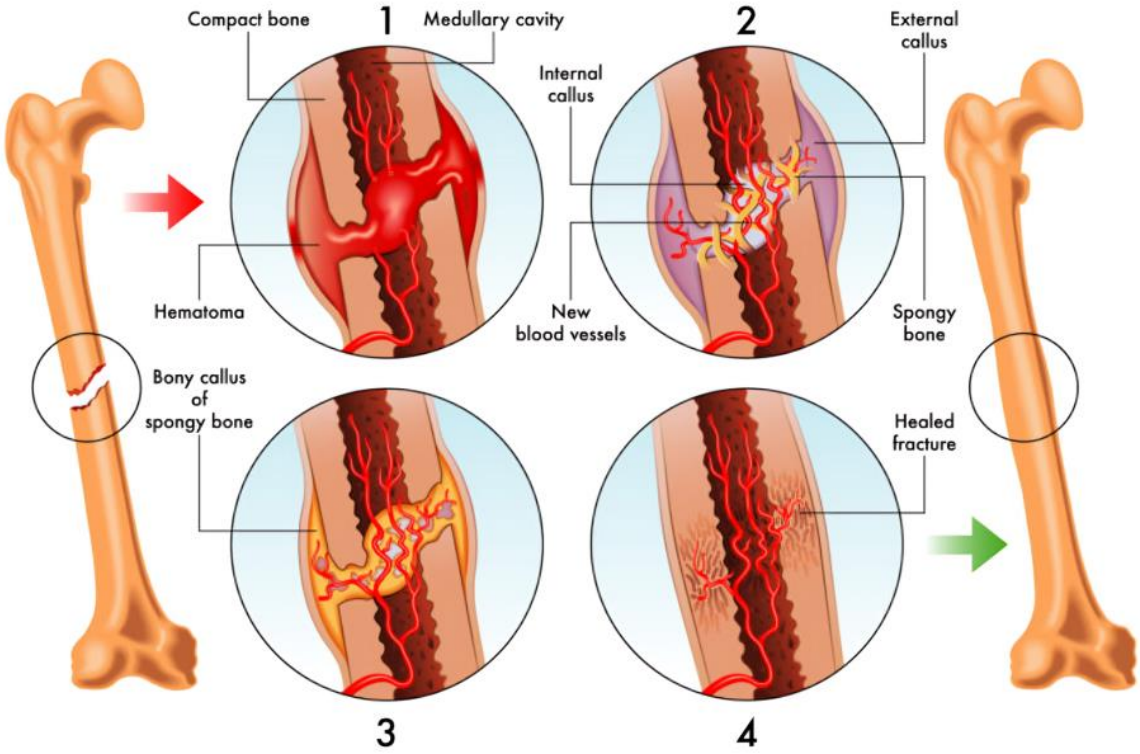

Figure 12: Stages of Bone Fracture Healing

2.3. Conventional Treatment Methods

This chapter delves into the conventional treatment methodologies for the healing of femoral bone fractures, a critical area in the field of biomechanical engineering. Emphasis will be placed on two predominant approaches: femoral plates and femoral nails. Through a detailed examination of these techniques, the chapter aims to explain their mechanisms, applications, and effectiveness in the treatment process. The combination of these two methods will also be discussed.

2.3.1. Femoral Plate Technologies

The analysis of femoral plates in bone fracture healing highlights the critical impact of material choice on biomechanical outcomes and recovery. Carbon/epoxy and glass/polypropylene composites, with a modulus closer to natural bone than stainless steel, reduce stress shielding—often caused by stiffer materials—which disrupts natural healing by unbalancing stress at the fracture site. Simulations show that composites promote a more beneficial biological response by allowing slight movements crucial for secondary bone healing. Furthermore, these materials not only

minimize stress shielding but also enhance mechanical stimulation, crucial in the initial stages of bone regeneration. Iterative modeling also demonstrates that adjusting the composite material's stacking sequence can optimize healing, aligning mechanical properties closely with natural bone behavior [17].

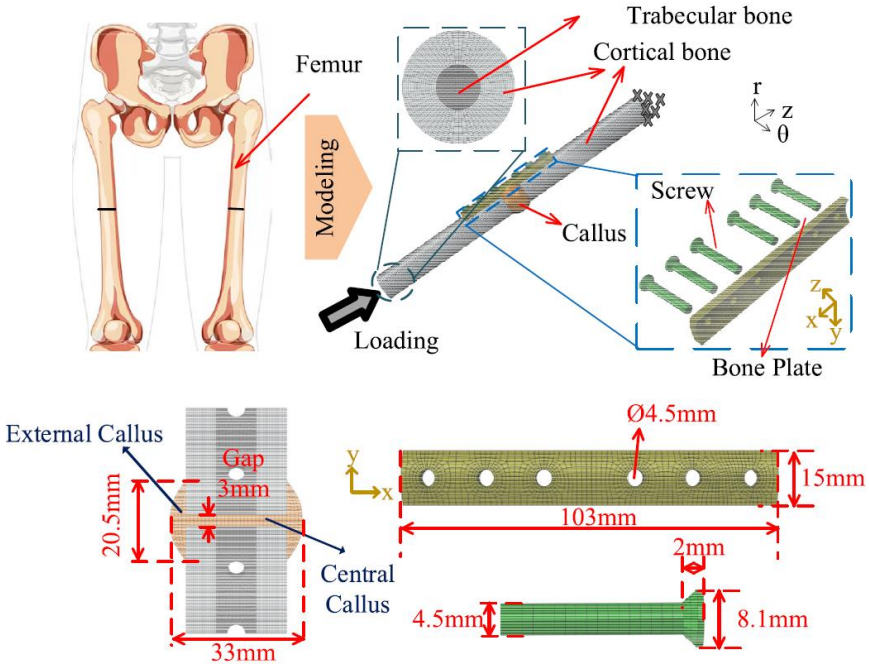

Figure 13: FEM of human femoral shaft with the application of a bone plate [17]

It is interesting to also investigate the effects of the impact that the plate's material has on its efficiency. The study by Soni et al. investigates a customized fixation plate for femoral shaft fractures using reverse engineering and finite-element analysis, focusing on three biocompatible materials: titanium alloy (Ti6Al4V), stainless steel (SS-316L), and cobalt-chromium-molybdenum alloy (Co–Cr–Mo). The research reveals that all materials maintain low stress levels under static physiological loads, suggesting effective stress distribution and minimal deformation. This indicates that the customized plates provide stable fixation, potentially improving fracture union outcomes. The stress is mainly concentrated near the screw threads closest to the fracture site, which is a common site for stress accumulation. Despite these stresses, they remain well below the materials' yield and ultimate strengths, indicating a robust design capable of withstanding physiological loads without failure. The deformation analysis shows slight differences among the materials, with titanium alloy experiencing the most deformation, followed by stainless steel and cobalt-chromium-molybdenum alloy, yet all within acceptable limits for clinical applications. These findings support the use of customized implants tailored to individual anatomical

needs, enhancing fixation stability and reducing surgery time and post-operative complications [18].

Building on the previous discussion on conventional and custom biocompatible fixation methods, the study by Chandra et al. explores the design and implications of using biodegradable materials for femoral shaft fracture fixation. Emphasizing the potential of biodegradable Mg-alloys, the study demonstrates how these materials not only support the fractured bone but also naturally degrade post-healing, negating the need for a second surgery. A biodegradable implant plate and screws were designed with a focus on achieving optimal dimensions that ensure uniform degradation and sufficient mechanical stability throughout the healing process [19].

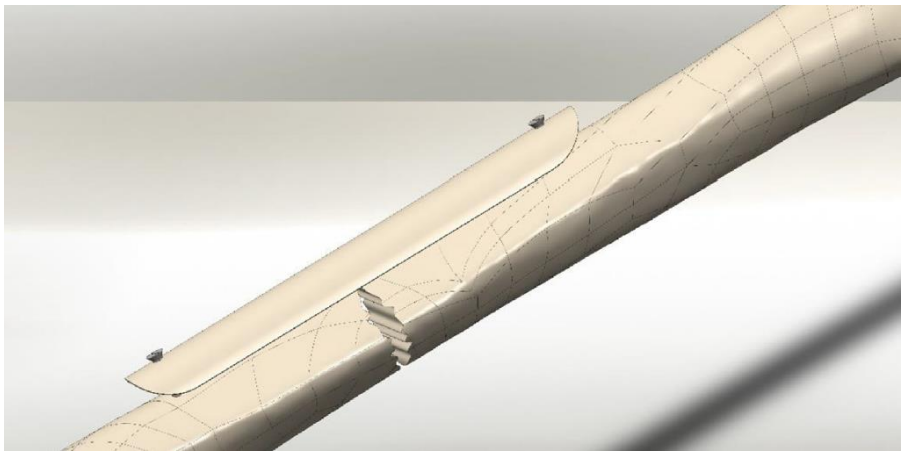

Figure 14: Femoral shaft plate implant

The research reveals that the chosen Mg-alloy plates exhibit consistent degradation over a six-month period, matching the typical healing timeframe, with degradation rates tailored to maintain mechanical integrity until healing is complete. The study utilizes finite element analysis to optimize the plate design, ensuring it withstands physiological loads while minimizing risks like stress shielding and premature degradation. This approach allows for a gradual transfer of load back to the healing bone, promoting natural bone growth without the complications associated with non-degradable materials. The findings advocate for a broader application of biodegradable materials in orthopedics, highlighting their benefits in enhancing patient outcomes and reducing healthcare costs associated with post-treatment interventions [19].

Distal femur plates feature a locking mechanism that ensures a secure and stable connection to the bone. The design of these plates includes a flat, elongated upper

section similar to standard locking plates, while the lower part has a unique geometry tailored to the contours of the femoral condyle. This specific design ensures precise alignment with the bone's complex structure, optimizing support and stability during recovery. Additionally, these plates are compatible with articulated tension devices, allowing for applied pretension to enhance stability and secure the fit further. There are various orthopedic distal femur fixation plates available in the market, designed to address a range of bone fractures.

These include the AxSOS 3 Titanium plates by Stryker, which stand out for their comprehensive application in long bone fracture fixation. These plates are specifically intended for use in a variety of conditions including diaphyseal, metaphyseal, and epiphyseal fractures, as well as extra- and intra-articular fractures. They are suitable for addressing non-unions and malunions, and are effective in both normal and osteopenic bones. Additionally, they are used in osteotomies and for periprosthetic fractures of the femur and proximal tibia. The AxSOS 3 Titanium Waisted Compression Plates extend their utility to pediatric patients for the fixation of diaphyseal and metaphyseal areas of long bones. They are also indicated for periprosthetic fractures and specifically include applications such as fixation of the scapula and the pelvis, showcasing their versatility and wide-ranging applications in orthopedic surgery [20], [21].

Figure 15: Stryker AxSOS 3 Ti distal lateral femur plating system

Figure 16: Treatment of distal femur fractures with locking plates

An articulated tension device is used in minimally invasive osteosynthesis (MIO) bridge plating for segmental, intact, distal 1/3 femoral fractures to apply precise compression across the fracture site. This device is particularly beneficial when direct handling of the fracture could disrupt vascular supply to the bone fragments. By preserving the soft tissue attachments and maintaining alignment through indirect reduction tools, the device aids in achieving stable fracture fixation conducive to natural healing processes without necessitating direct manipulation of the fracture zone. This method is critical for maintaining blood supply and promoting satisfactory indirect bone healing via callus formation [22].

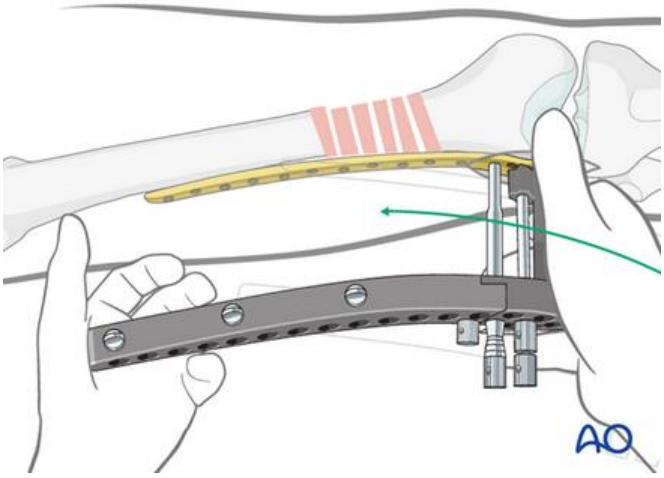

Figure 17: Articulated tension device

2.3.2. Femoral Nailing Techniques

This subchapter delves into femoral nailing techniques, a critical approach in orthopedic surgery for securing femoral fractures. This method is essential for promoting rapid healing and maintaining precise bone alignment, offering both antegrade and retrograde approaches. Antegrade nailing involves insertion of the nail at the hip and is commonly used for fractures in the femoral shaft, while retrograde nailing starts at the knee and is preferred for certain types of distal fractures or when the hip anatomy is disrupted. Retrograde nailing, where the nail is inserted through the intercondylar notch of the knee, and antegrade nailing, inserted through the piriformis fossa, are both well-established methods, each presenting unique advantages depending on the patient's condition and specific fracture characteristics.

Retrograde Nailing is often favored for distal femoral shaft fractures or cases with additional proximal fractures due to its minimally invasive approach at the knee, potentially reducing hip complications but increasing knee-related issues [23]. Conversely, retrograde nailing is preferred for more distal fractures or in situations where the hip region is not optimal for surgical access, such as in obese patients or those with multiple injuries. While retrograde nailing generally leads to higher instances of knee pain postoperatively, it offers better control and fixation of distal fractures, which is advantageous in complex cases [24], [25].

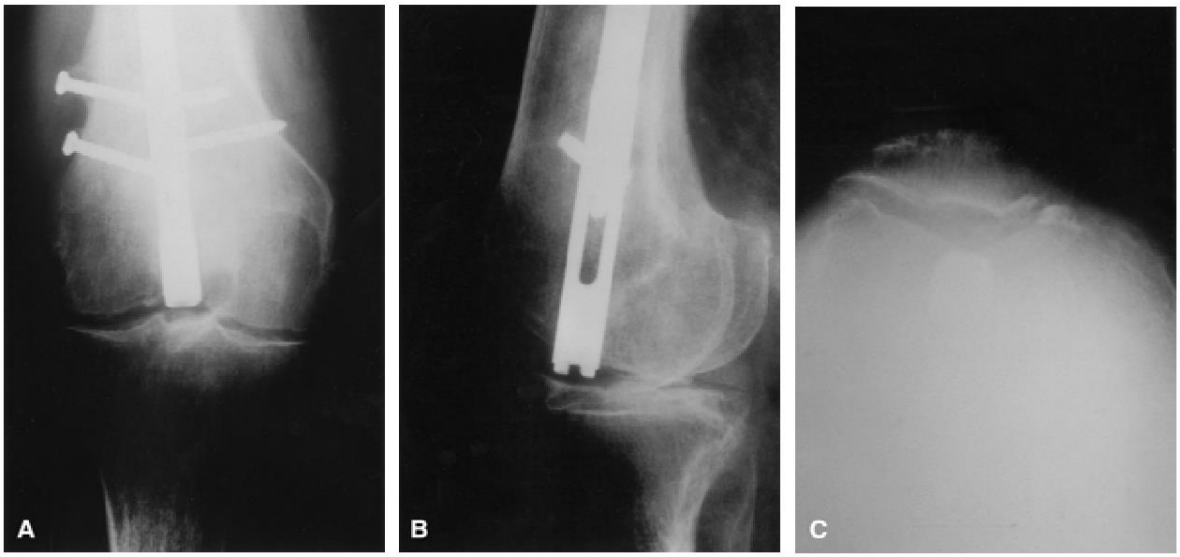

Figure 18: Migration of a retrograde nail onto the knee joint after fracture of distal interlocking screws. A: Anteroposterior view. B: Lateral view. C: Merchant view

Antegrade Nailing, on the other hand, is typically preferred for diaphyseal fractures. It is noted for potentially causing heterotopic ossification around the hip and may risk injury to the pudendal nerve. [23]. Antegrade femoral nailing, where the nail is inserted at the hip (either through the piriformis fossa or the greater trochanter), is typically chosen for fractures located more proximally on the femur. This method can result in complications such as hip pain and heterotopic ossification due to the surgery's proximity to the hip muscles and joints. Notably, the trochanteric entry, compared to the piriformis entry, significantly reduces the operative duration by approximately 14 minutes and shows a tendency towards less hip pain and complications [24], [25].

Ricci et al. found that both techniques demonstrated high union rates with no significant difference in overall healing or incidence of malunion between the groups. However, retrograde nailing showed a higher incidence of knee pain (36% in cases without direct knee injury), which was significantly greater than the 9% in the antegrade group. Conversely, antegrade nailing led to more hip pain in the absence of direct hip injuries. In the study, there were comparable rates of malunion between the two groups, with 11% in the retrograde group and 13% in the antegrade group. Both methods provided satisfactory results with similar union and malunion rates. However, the choice of technique might be influenced by the specific needs related to the site of fracture and potential complications, such as the increased knee complications observed with retrograde nailing compared to the hip issues with antegrade nailing [23]. Across some studies, no significant differences were observed in major outcomes like union rates or malalignment between antegrade and retrograde nailing, indicating both techniques are similarly effective in promoting fracture healing. However, each technique exhibits distinct profiles of minor complications and postoperative pain, influenced by the surgical approach and anatomical entry points. For instance, antegrade nailing tends to involve more significant hip and thigh pain, while retrograde nailing is associated with more frequent knee pain [24], [25].

The R/AFN system by Synthes is designed as a versatile solution for the treatment of femoral fractures, enabling both antegrade and retrograde nailing. This dual approach caters to a broad spectrum of femoral injuries, including diaphyseal and distal fractures, by allowing the nails to be inserted either from the hip (antegrade) or knee (retrograde). With its universal design, the R/AFN accommodates both the right and left femur and incorporates an anatomical bend to aid insertion. The system features

a variety of locking options, such as spiral blade and standard locking, which enhance stability especially in fractures involving the femoral condyles.

The R/AFN nails come in a range of diameters and lengths to suit different anatomical needs, with specific lengths designated for either antegrade or retrograde insertion. This flexibility is further supported by a newly designed instrument set that facilitates a more percutaneous technique, reducing tissue damage. Compared to Synthes' Distal Femoral Nail, the R/AFN offers additional locking configurations and is compatible with both antegrade and retrograde approaches, showcasing its adaptability and comprehensive application in treating femoral fractures [26], [27].

Figure 19: R/AFN intramedullary nailing system

To address surgical challenges in obese patients, percutaneous insertion handles for the LFN and R/AFN have been lengthened. Standard handles are often too short for the thick soft tissue in these patients, necessitating a longer handle to facilitate more proximal incisions and reduce the need for deep tissue dissection. This modification requires longer connecting screws and a hexagonal screwdriver for effective operation. However, this handle is specifically designed for obese patients, as its length may impede procedures in non-obese individuals by affecting surrounding tissues [26].

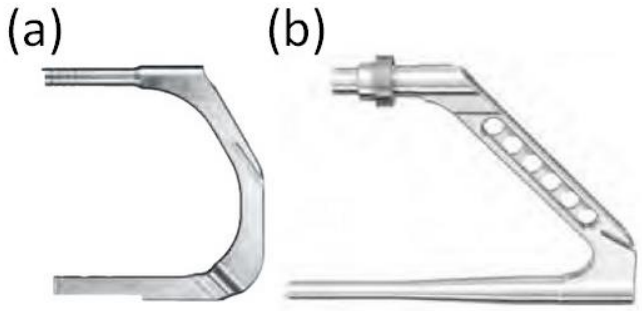

Figure 20: Percutaneous Insertion Handle for LFN and R/AFN. (a) Normal handle. (b) Handle for obese patients

The R/AFN Arm for Proximal Aiming Device (PAD) significantly enhances the precision and efficiency of femoral nail locking processes. This device allows surgeons to achieve both distal and proximal locking of the nail entirely without the need for fluoroscopic guidance. By accurately calibrating the PAD to the specified nail length, the proximal guide component ensures proper alignment and positioning of the nail's locking holes. This system facilitates the drilling and placement of screws using a guided method akin to using a conventional aiming arm, offering a streamlined alternative to the more labor-intensive free-hand technique [26].

Figure 21: R/AFN Arm for Proximal Aiming Device

2.3.3. Synergistic Integration of Femoral Plates and Nails

It is essential to also explore the efficacy of combining femoral nail and plate fixation for treating distal femoral fractures. This hybrid approach is suggested to improve outcomes by maximizing the strengths of both fixation methods, enhancing stability, and promoting fracture union, allowing for early weight-bearing. The analysis confirms the benefits of this method, particularly for high-risk patients prone to nonunion or those requiring robust stabilization due to poor bone quality. However, the technique involves longer surgical and fluoroscopy times, potentially leading to greater blood loss compared to traditional single-method treatments [28].

Figure 22: Anteroposterior (A) and lateral (B) views demonstrate interlocking the Synthes (West Chester, PA) distal femur lateral locking plate (variable angle locks compression of condylar plate 4.5/5.0) and retrograde nail system

This combined approach, initiated due to concerns over high failure rates with single plate fixation, aimed to enhance fracture stabilization and enable early weight-bearing. Results indicate significantly better outcomes with the combined method, including higher fracture union rates and reduced metalwork failures, particularly beneficial in osteoporotic fractures. The combined approach allowed earlier weight-bearing, thereby potentially reducing immobilization-related complications and improving patient outcomes in fracture treatment [20]. The combined method also offers superior mechanical stability, potentially leading to improved healing rates compared to single-method approaches. Patients treated with both nails and plates are often also able to bear weight earlier, which is crucial for rehabilitation and reducing the risk of complications associated with prolonged immobility [29], [30].

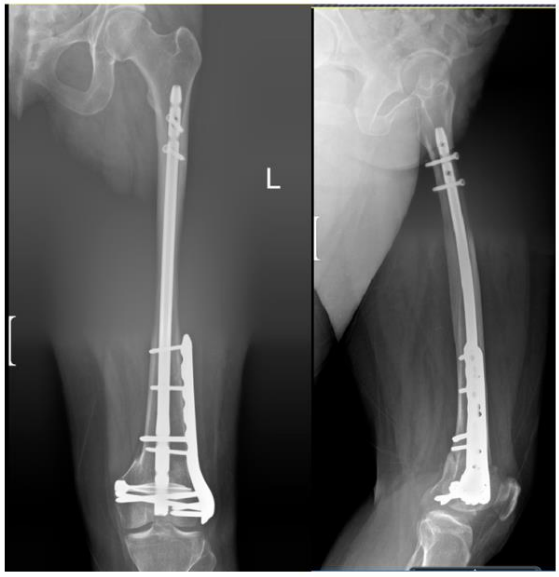

Figure 23: Post operative radiographs of a ppatient managed with nail-plate fixation

While offering advantages, the combined approach requires careful surgical planning and higher proficiency to manage the increased complexity of the procedure. Moreover, the combined use may increase the risk of surgical complications, such as infection or hardware interference [29], [30].

2.3.4. Limitations of Conventional Methods

Conventional methods for treating distal femoral fractures, such as plates and nails, face significant limitations that highlight the need for technological advancements in orthopedic trauma care. These methods often struggle with ensuring adequate mechanical stability, particularly in patients with osteoporotic bones or those with complex fracture patterns, leading to high rates of nonunion and implant failure. The limitations in torsional and axial load resistance can impede early mobilization and weight-bearing, crucial for patient recovery. Additionally, these fixation techniques require precise alignment and can result in extended surgical times and increased exposure to fluoroscopy, raising the risk of complications. This underscores the urgent need for developing more effective, adaptable, and less invasive stabilization systems that can provide reliable fixation, promote faster healing, reduce the risk of complications, and accommodate the varying anatomical and biological needs of patients across different age groups and bone quality scenarios [20], [28], [29], [30]. Additionally, patients with extra weight face further complications, as conventional

methods like plates and nails require more intensive adjustments to ensure stability. This often necessitates additional surgical interventions to prevent failure [26].

2.4. Role of 3D Printing in Bone Regeneration

This chapter explores the significance of 3D printing and its role in bone regeneration. The advantages of 3D printing over traditional methods are highlighted, focusing on customization capabilities, the reduction of surgical times, and the integration of growth factors to enhance healing.

2.4.1. 3D Printing Technologies

Also known as additive manufacturing, 3D printing creates physical objects from a geometrical representation by successively adding materials layer by layer. 3D printing encompasses several technologies, each with unique processes and applications [31]:

- **Binder Jetting:** Binder jetting involves depositing a liquid binding agent selectively to join powder particles. This process is simple, fast, and cost-effective, making it suitable for producing casting patterns, raw sintered products, and large-volume products from materials like metals, sands, polymers, hybrids, and ceramics.
- **Directed Energy Deposition:** This complex process is used to repair or add material to existing components. It offers high control over grain structure and is typically used with metals, ceramics, and polymers.
- **Material Extrusion:** In material extrusion, thermoplastic filament is heated and extruded layer by layer to build parts. Fused Deposition Modelling (FDM) is a prominent example, commonly used for printing plastics, food, or living cells due to its low cost and ability to produce fully functional parts.
- **Material Jetting:** This process involves selectively depositing droplets of photosensitive material that solidify under UV light. Material jetting produces parts with smooth surfaces and high dimensional accuracy, using materials such as polymers, ceramics, composites, biologicals, and hybrids.
- **Powder Bed Fusion:** Techniques like Selective Laser Sintering (SLS) and Electron Beam Melting (EBM) use lasers or electron beams to fuse material powder. This method is suitable for creating metal, plastic, and ceramic objects with high precision and varied surface finishes.
- **Sheet Lamination:** This process bonds sheets of materials to produce a part. It is cost-effective and time-efficient, capable of producing complex geometrical

parts. Laminated Object Manufacturing (LOM) and Ultrasound Additive Manufacturing (UAM) are notable examples.

- **Vat Photopolymerization:** This widely used technique involves curing photo-reactive polymers with a laser or UV light. Stereolithography (SLA) and Digital Light Processing (DLP) are common methods, producing high-quality, detailed products.

2.4.2. 3D Printed Bone Scaffolds and TPMS Microarchitectures

Vertical bone augmentation and osteoconduction are crucial procedures in implantology aimed at increasing the height of the alveolar ridge and facilitating the ingrowth of new bone tissue, respectively. Despite numerous studies exploring various materials and techniques, there remains debate over the optimal procedures and materials. Recently, triply periodic minimal surface (TPMS) microarchitectures have emerged as promising candidates due to their lightweight yet robust properties, mimicking the natural bone structure [32].

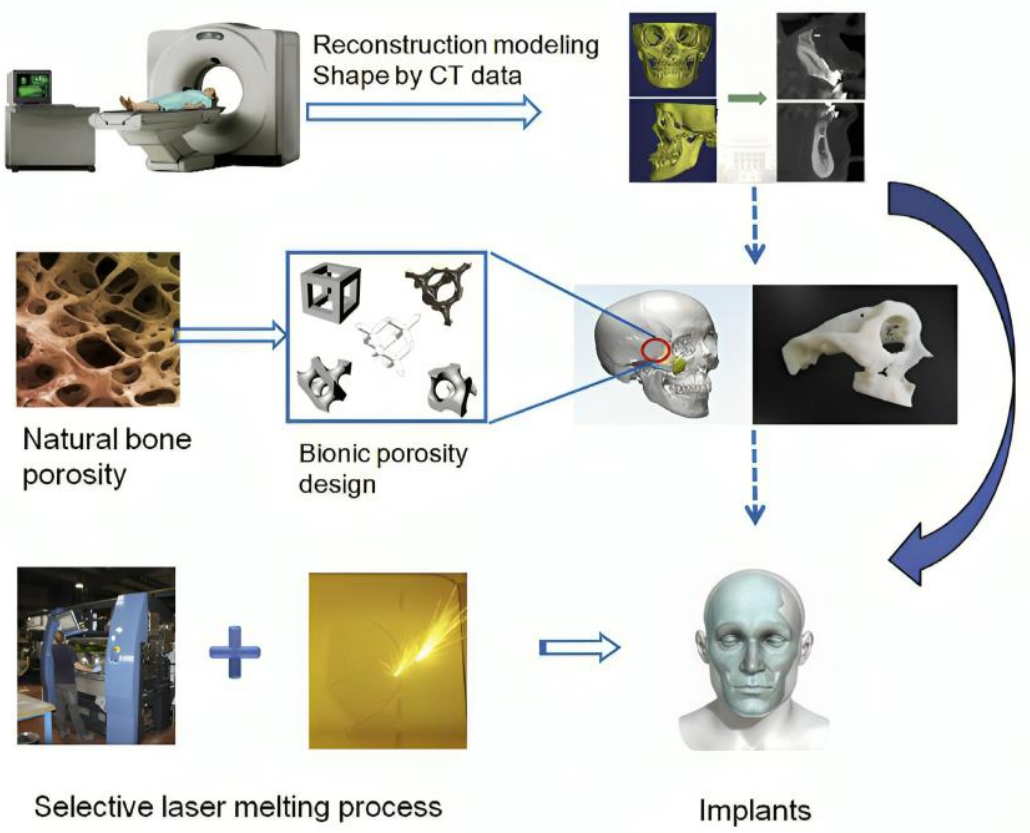

Figure 24: Schematic of 3D printing of metal products with microporous structure and its application in biomedicine

The study by Maevskaia et al. explore the lattice structures of D-diamond, G-gyroid, and P-primitive, produced through 3D printing with hydroxyapatite, for their potential in bone augmentation and osteoconduction [33].

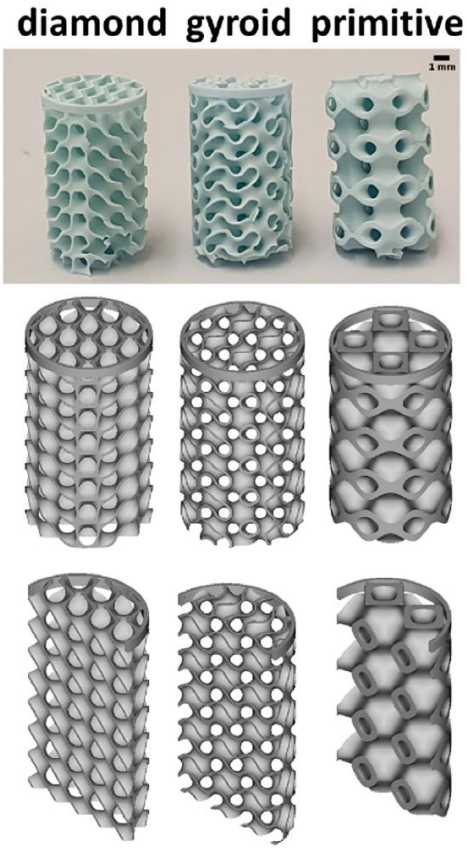

Figure 25: Micro- and macroarchitectures of the scaffolds used in Maevskaia et al. bone augmentation model

Voronoi lattices are characterized by their irregular, non-repetitive porous structures, which closely mimic the natural architecture of bone. In the generation of Voronoi lattices, random seeds and points are crucial for creating a stochastic, or randomly distributed, lattice structure. The process begins by placing random seed points within a defined space. These seed points act as the nuclei for the Voronoi cells. Each point generates a cell comprising all locations closer to it than to any other seed point. The random placement of these seeds results in cells of various shapes and sizes, contributing to a highly irregular and natural-looking lattice. This stochastic distribution ensures that the Voronoi lattice can adapt to different requirements, providing a unique and non-repetitive structure each time. The variability in the cell size and shape, inherent to the random seed placement, is key to the versatility and effectiveness of Voronoi lattices in applications like material science and structural engineering [34].

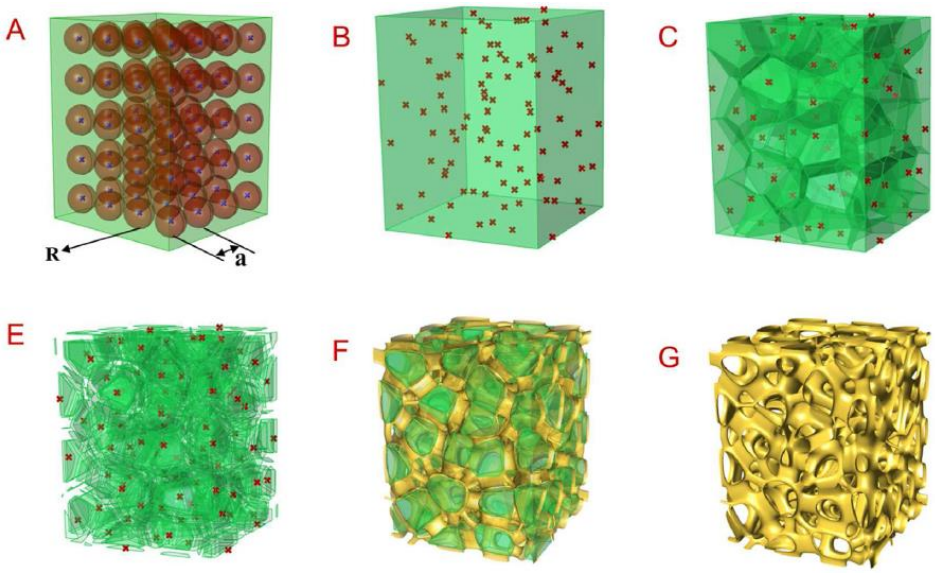

Figure 26: Solid Voronoi diagram generate process (A) probability sphere; (B) random seeds; (C) Voronoi diagram; (D) scaling; (F) generating scaffold; (G) Smooth treatment.

Voronoi lattices, with their irregular structure, distribute stress more evenly, reducing stress concentration and implant failure risks. Unlike regular lattices, which can cause stress shielding due to higher elastic modulus, Voronoi designs align with natural bone stress distribution, enhancing compatibility. Their porous nature improves permeability, allowing better nutrient flow and waste removal, crucial for cell growth. Studies show Voronoi scaffolds offer superior permeability, supporting better biological integration and faster bone healing compared to regular lattice structures. [34].

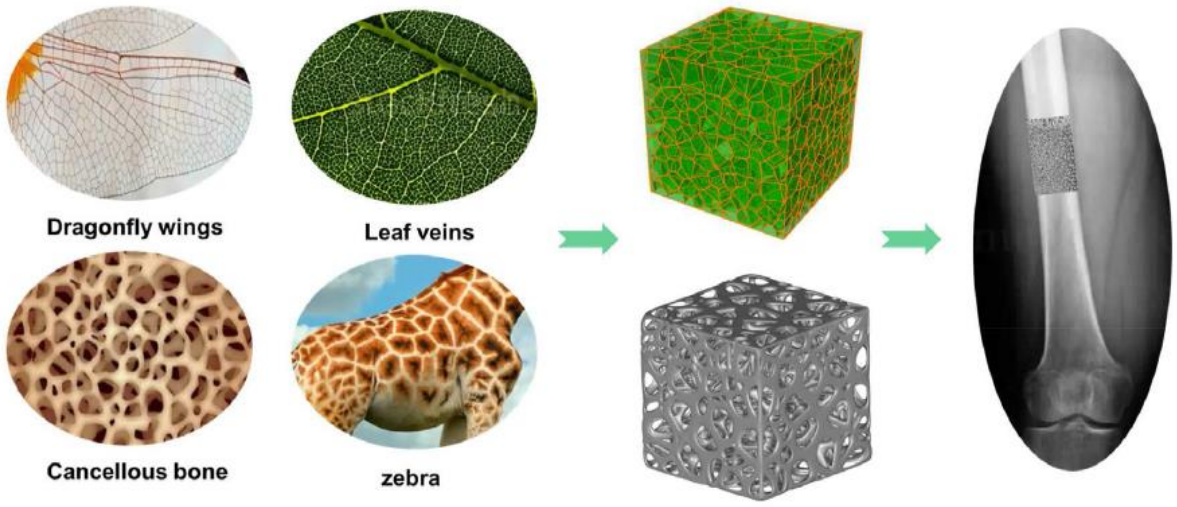

Figure 27: Regular method of modeling bionic structure via Voronoi diagram

Wang et al. recommend a method for constructing artificial bones with porous gradient structures, a significant innovation in bone tissue engineering. The process begins by offsetting the surface of the bone model by incremental distances to create a layered effect. Next, spherical regions are generated based on the intersection points of UV isocurves, creating a precise and organized pattern. Finally, an irregular lattice structure is developed within these spherical regions, resulting in a porous gradient that closely mimics the natural architecture of bone. This approach enhances the structural integrity and biological compatibility of the artificial bone, making it a promising solution for effective bone repair and regeneration, as demonstrated in Figure 28 [35].

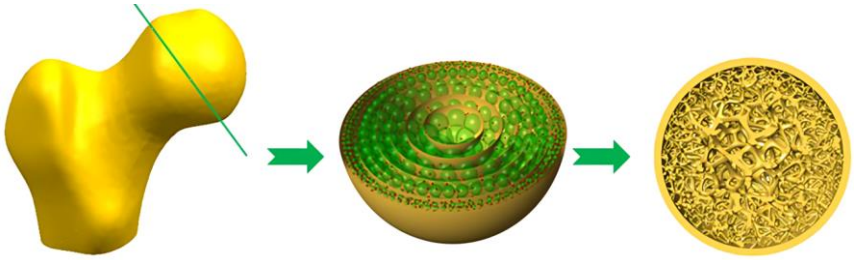

Figure 28: Construction of porous gradient artificial bone: (1) Surface offset, (2) Spherical regions at UV isocurve intersections, (3) Irregular lattice formation

2.4.3. Materials Used in 3D Printed Bone Scaffolds

The choice of materials for 3D printed bone scaffolds is crucial in ensuring biocompatibility, mechanical strength, and the ability to support bone regeneration. The study conducted by Li et al. provides an in-depth analysis of the materials used in 3D printed bone scaffolds, focusing on their properties, advantages, and applications [36].

Metallic Materials

Metallic materials have long been favored for bone implants due to their strength and durability. Titanium and its alloys are the most widely used metals in medical implants. They offer high strength, low density, and excellent corrosion resistance, which are essential for long-term stability in the human body. Pure titanium and alloys such as Ti6Al4V, Ti-13Nb-13Zr, and Ti-35Nb-5Ta-7Zr have been extensively studied and used [32], [34], [35], [36], [37], [38]. These materials can be designed with a porous structure to match the elastic modulus of natural bone, thus avoiding the stress shielding effect that can lead to implant failure. The biocompatibility of titanium and its alloys is well-established, promoting osseointegration and long-term success of the implants.

Magnesium and its alloys represent another class of metal materials used in bone scaffolds [36], [39], [40]. These materials are known for their high strength, low density, and biodegradability. Magnesium alloys gradually degrade in the body, being replaced by natural bone over time, which is ideal for load-bearing applications where temporary support is needed. However, the poor corrosion resistance of magnesium alloys remains a challenge, and ongoing research aims to enhance their performance through alloying and surface treatments.

Tantalum is recognized for its excellent biocompatibility and osteoconductivity, making it a valuable material for bone repair, especially in large bone defects. Known as the "biophilic metal," tantalum promotes significant bone ingrowth and forms a strong bond with the surrounding bone tissue. This material's high porosity and favorable mechanical properties make it suitable for creating highly integrated bone scaffolds.

Bio-Ceramic Materials

Bio-ceramic materials, particularly hydroxyapatite (HAp) and β-tricalcium phosphate (β-TCP), play a pivotal role in bone tissue engineering due to their chemical similarity to natural bone. Hydroxyapatite is highly biocompatible and both osteoconductive and osteoinductive, promoting the natural bone healing process. It is commonly used in bone grafts and as a coating for metal implants to enhance their integration with bone tissue.

β-Tricalcium phosphate, on the other hand, is highly resorbable and provides a temporary scaffold that is gradually replaced by new bone. This property makes it ideal for applications where scaffold resorption and replacement by natural bone are desired. Bioactive glasses are another group of bio-ceramics that have gained attention for their high strength, toughness, and bioactivity. These materials can bond with bone and stimulate new bone growth, and their degradation rates can be tailored by incorporating different ions.

Polymer Materials

Natural and synthetic polymers are widely used in 3D printed bone scaffolds due to their biocompatibility and ability to degrade in the body. Natural polymers like gelatin and collagen offer excellent biocompatibility and biodegradability. Gelatin is non-immunogenic and promotes cell proliferation, making it suitable for soft tissue engineering. Collagen, a major component of natural bone, supports cell attachment and growth, enhancing the biological integration of the scaffold.

Synthetic polymers such as polycaprolactone (PCL), polylactic acid (PLA), and poly-ether-ether-ketone (PEEK) provide additional benefits [36], [41], [42]. PCL is known for its excellent mechanical properties and biodegradability, making it a preferred material for bone scaffolds. PLA is widely used in tissue engineering due to its biocompatibility and ease of processing. PEEK, although non-degradable, offers mechanical properties similar to human bone and can be combined with other materials to improve its bioactivity.

Composite Materials

Composite materials combine the benefits of different materials to create scaffolds with enhanced properties. Inorganic-organic composites, such as silk fibroin combined with β-tricalcium phosphate (SF/β-TCP) or hydroxyapatite (SF/HAp), improve mechanical strength and promote cell attachment and proliferation. These composites harness the mechanical properties of ceramics and the biological benefits of polymers, making them ideal for bone tissue engineering.

Degradable composite scaffolds, such as those made from hydroxyapatite and polycaprolactone (HA/PCL) or polylactic acid and hydroxyapatite (PLA/HA), are designed to degrade at a controlled rate, matching the natural bone healing process. These materials provide temporary mechanical support while enhancing osteogenesis and allowing for the gradual replacement by natural bone.

2.4.4. Advantages over Traditional Methods

3D printed bone scaffolds offer significant advantages over conventional methods such as femoral plates and nails, primarily due to their ability to closely mimic the natural structure and function of bone. Traditional methods often involve metallic implants that, while providing the necessary mechanical support, can lead to complications such as stress shielding, where the implant bears most of the load instead of the bone. This can result in bone resorption and weakening over time. In contrast, 3D printed scaffolds can be designed with tailored porosity and mechanical properties that match the patient's bone, promoting natural load distribution and reducing the risk of stress shielding.

Moreover, 3D printing technology allows for the creation of patient-specific implants, customized to fit the exact geometry of the bone defect. This personalized approach enhances the integration of the scaffold with the surrounding bone tissue, promoting faster and more effective healing. The use of biocompatible and biodegradable materials in 3D printed scaffolds further supports bone regeneration by providing a

temporary structure that gradually degrades as new bone forms, eliminating the need for a second surgery to remove the implant. Additionally, the incorporation of bioactive materials such as hydroxyapatite can stimulate osteogenesis, further enhancing the healing process. These capabilities make 3D printed bone scaffolds a superior alternative to conventional femoral plates and nails, offering improved functional and biological outcomes for patients.

2.5. Homogenization in Composite Materials

For this study, nTopology software has been utilized to conduct homogenization analyses on the bone scaffold, enabling more efficient simulations while significantly reducing computational resource requirements. This software is based on the methodologies detailed in the paper by Andreassen et al., which will be thoroughly explained in this chapter [43].

Homogenization is a critical computational technique used to determine the effective macroscopic properties of composite materials by analyzing their microstructure. This method is particularly valuable in the field of material science and engineering, where materials with complex microstructures are used to achieve desired mechanical properties. Homogenization is a numerical technique employed to compute the effective properties of a heterogeneous material by averaging the properties of its micro-constituents. This is especially applicable to composite materials, where different materials are combined to create a material with superior properties. The process involves creating a representative volume element (RVE), which is a small, periodic unit cell of the material's microstructure. By analyzing this unit cell, the overall macroscopic properties can be inferred.

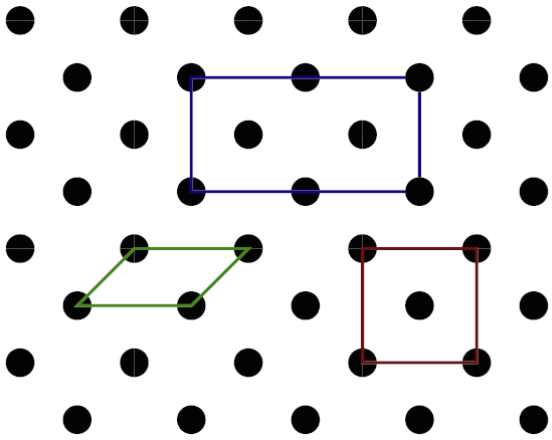

Figure 29: A section of a 2D periodic microstructure consisting of two materials (white and black). The red line encloses a square unit cell, the blue a rectangular unit cell, and the green a parallelogram unit cell.

The effective macroscopic properties of a periodic composite material can be determined using the elasticity tensor, denoted as E^H_{ijkl}. According to the theory of homogenization, this tensor is calculated as follows [43]:

$$E^H_{ijkl} = \frac{1}{|V|}\int_V E_{pqrs}\left(\epsilon^0_{ij} - \epsilon_{ij}\right)\left(\epsilon^0_{kl} - \epsilon_{kl}\right)\, dV \tag{1}$$

Where |V| is the volume of the unit cell, E_{pqrs} is the local stiffness tensor, ϵ^0_{ij} are the prescribed macroscopic strain fields, and ϵ_{ij} are the locally varying strain fields. The strain fields are derived from the displacement fields by solving the elasticity equations with the prescribed macroscopic strain.

The paper provides a detailed implementation of numerical homogenization using MATLAB. The process starts by discretizing the unit cell into finite elements. Each element is characterized by its material properties, which are specified by Lamé's parameters (λ and μ). The unit cell's geometry and the indicator matrix, which specifies the material in each element, are also defined. The element stiffness matrix K and load vectors are computed using the finite element method (FEM). The stiffness matrix is assembled by summing the contributions from all elements, while the load vectors correspond to macroscopic volumetric straining. The global stiffness matrix and load vectors are then used to solve for the displacement fields. Once the displacement fields are obtained, the homogenized elasticity tensor is computed. This involves integrating the strain and displacement fields over the volume of the unit cell, yielding the macroscopic properties of the composite material.

2.6. Optimal Environment for Osteogenesis

This chapter delves into the definition and optimization of 3D printed scaffolds, crucial for effective bone regeneration. This chapter discusses key design considerations such as pore size, strut radius, scaffold geometry, and the mechanical properties required to support cell growth and bone healing. It also examines various optimization techniques, including computational modeling and finite element analysis, which are used to tailor scaffold designs to meet patient-specific needs. The focus is on how these design parameters can be manipulated to enhance the biological functionality and structural integrity of the scaffolds, ultimately improving patient outcomes.

2.6.1. Ideal Porosity Ranges

Porosity is a critical factor in scaffold design as it affects both mechanical strength and biological performance. Voronoi lattices allow for a variable porosity design, which can be tailored to match the specific requirements of different bone regions, based on the number of seed points and on the radius of the strut.

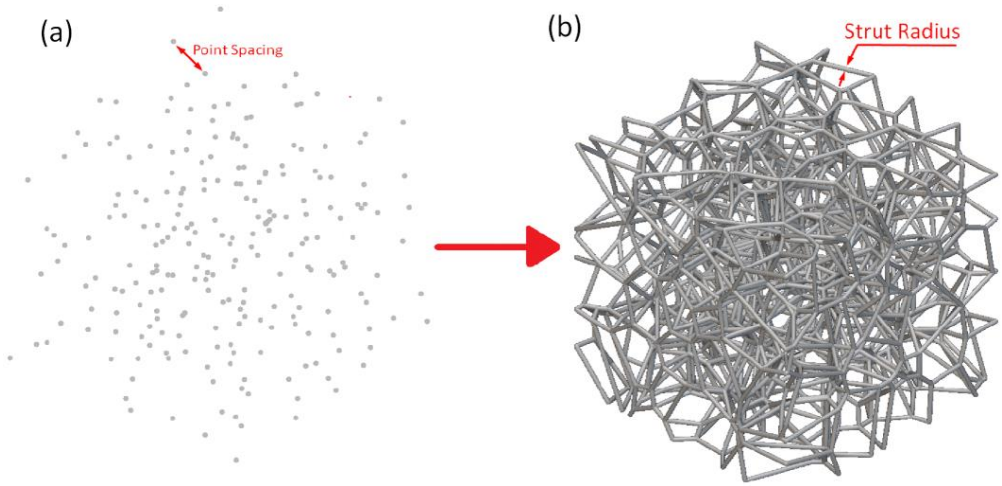

Figure 30: Defining parameters of Voronoi lattice. (a) Point spacing; (b) Strut radius

The porosity of a lattice is defined through the following expression:

$$\Phi = 1 - \frac{\rho_{Lattice}}{\rho_{Solid}} \cdot 100\% \quad (2)$$

Research indicates that Voronoi structures can achieve a balance between high porosity and sufficient mechanical strength, making them ideal for complex bone implant scenarios [35].

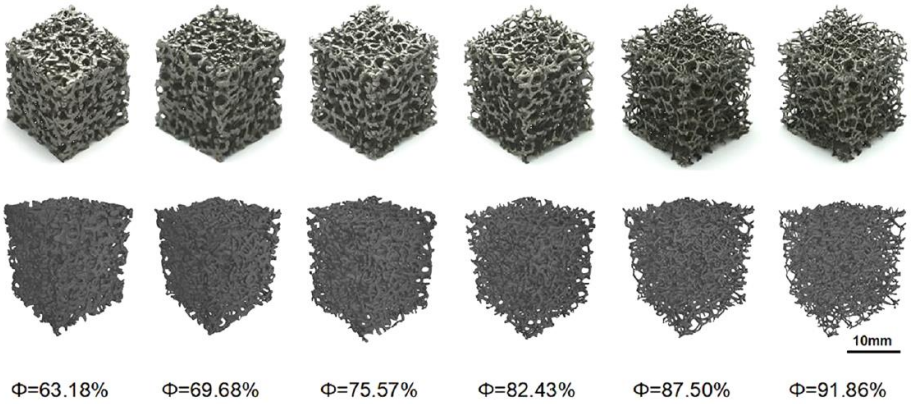

Figure 31: Various porosities of voronoi lattices

The porosity of bone scaffolds also plays a crucial role in the process of osteogenesis, which is the formation of new bone tissue. According to the paper by Vassilis Karageorgiou and David Kaplan, the ideal porosity range for bone scaffolds are the following:

Table 1: Ideal porosity range for osteogenesis

$\Phi_{ideal,low}$	$\Phi_{ideal,up}$
50%	90%

This range is optimal for several reasons related to the mechanical properties, cell migration, and vascularization essential for effective bone regeneration. A porosity range of 50% to 90% is deemed ideal because it balances the mechanical strength of the scaffold with the biological needs for bone formation. Higher porosity allows for better cell infiltration and nutrient flow, which are essential for the growth and maintenance of new bone tissue. It also facilitates vascularization, which is the formation of new blood vessels. This process is crucial for providing oxygen and nutrients to the growing bone tissue and removing metabolic waste products [44].

The primary reasons for maintaining scaffold porosity within this range include:

- **Cell Migration and Proliferation:** High porosity provides sufficient space for osteoblasts (bone-forming cells) and mesenchymal stem cells to migrate into the scaffold and proliferate. This is essential for the initial stages of bone formation.
- **Nutrient and Waste Exchange:** Adequate porosity ensures that cells within the scaffold receive sufficient nutrients and oxygen. It also allows for the efficient removal of waste products, which is critical for cell survival and function.
- **Mechanical Properties:** While high porosity is beneficial for biological reasons, it can compromise the mechanical strength of the scaffold. Therefore, the porosity should be optimized to provide sufficient mechanical support while allowing biological processes to occur effectively. The 50% to 90% range strikes this balance well.
- **Vascularization:** Larger pores within the scaffold enhance vascularization, which is vital for long-term bone health and regeneration. Vascularized bone tissue can maintain itself and integrate more effectively with the surrounding bone.

Although 50% to 90% is the recommended range, it is acceptable for the porosity to vary slightly above or below this range depending on the specific application and the type of bone being regenerated. Slight variations in porosity can still provide the necessary environment for osteogenesis, although they may impact the rate or quality of bone formation to some extent.

2.6.2. Ideal Strain Ranges

Mechanical strain is also an integral to the bone healing process, particularly in the differentiation of tissues within the fracture callus. Following a fracture, the initial formation of granulation tissue sets the stage for subsequent tissue differentiation. This granulation tissue provides a scaffold that is sensitive to mechanical loading. Studies have shown that the application of appropriate mechanical strain can enhance the healing process by promoting the formation of fibrous tissue, cartilage, and eventually bone.

High shear strain and fluid flows within the tissue deform precursor cells, stimulating the formation of fibrous connective tissue. As the strain and fluid flow decrease, these stimuli favor the differentiation of chondrocytes, leading to the formation of cartilage. Further reduction in strain and fluid flow creates a conducive environment for osteoblast differentiation and ossification, thus forming new bone.

The magnitude and type of mechanical strain applied are critical for effective tissue differentiation. Deviatoric strain, which refers to the differential stress that changes the shape of the tissue without changing its volume, has been shown to be a significant mechanical parameter guiding tissue differentiation. High deviatoric strain promotes the formation of fibrous tissue, while lower deviatoric strains are conducive to cartilage and bone formation.

Fluid flow within the fracture callus also plays a pivotal role. Interstitial fluid flow increases biomechanical stress on cells, enhancing the deformation and mechanical stimuli experienced by the cells. High fluid flow rates can elevate the shear stress on cells even when the solid phase strain is low, thereby influencing tissue differentiation patterns. This fluid-induced stress is essential for the initial stages of tissue differentiation, particularly in forming fibrous connective tissue and cartilage.

Deviatoric strain, as mentioned, influences the formation of fibrous tissue. Conversely, hydrostatic compressive stress, which refers to stress applied equally in all directions, is known to stimulate chondrogenesis (the formation of cartilage). The precise balance and interaction between these strains dictate the progression of tissue differentiation. For instance, high hydrostatic stress correlates with cartilage formation, whereas low

hydrostatic stress facilitates bone formation. The two prevalent studies concern the studies published by Lacroix et al. and Isaksson et al. [45], [46].

Table 2: Boundaries of the biophysical stimuli for tissue formation according to the various mechano-regulation algorithms investigated, including the three algorithms with only one stimulus

Predicted tissue type	Carter		Claes and Heigele		Lacroix and Prendergast		Single parameter studies		
	Principal tensile strain (%)	Hydrostatic stress (MPa)	Principal strain (%)	Hydrostatic pore pressure (MPa)	Deviatoric strain % (SS)	Fluid flow μm/s (FF)	Deviatoric strain (%)	Fluid flow (μm/s)	Pore pressure (MPa)
					$i = SS/3.75 + FF/3$				
Fibrous tissue	>5	⩽0.2	>15 >5	>0.15 >−0.15 < −0.15	$i>3$		>5	>5	>0.6
Cartilage or Endochondral ossification	⩽5	>0.2	⩽15	>0.15	$i>1$		>2.5	>2.5	>0.4
Bone or Intramembranous ossification									
Immature bone					$i>0.267$		>0.05	>0.6	>0.1
Mature bone	⩽5	⩽0.2	⩽5	<±0.15	$i>0.010$		>0.005	>0.03	>0.03
Resorption					$i⩽0.010$		⩽0.005	⩽0.03	⩽0.03

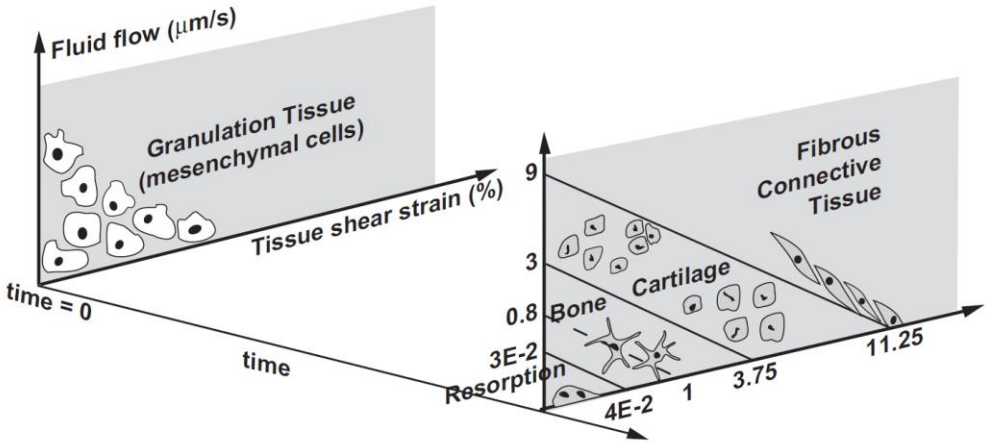

Figure 32: Boundaries of the biophysical stimuli for tissue formation

Although the literature emphasizes deviatoric strain in bone tissue differentiation, the current study utilizes equivalent von Mises stress. Derived from the deviatoric components of the stress tensor, von Mises stress provides a scalar measure of distortion energy within the material. This measure effectively captures the mechanical environment cells experience, crucial for simulating tissue differentiation processes. By using von Mises stress, the simulations can account for the overall stress state without explicitly incorporating fluid dynamics, thereby representing more closely the mechanical stimuli relevant to bone healing.

Furthermore, strain theory includes shear strain and the dynamics of fluid velocity within the porous structure of bone. The velocity of fluid within these pores results from changes in the volume of a finite element; expanding elements “drain” fluid,

while contracting ones “expel” fluid. This phenomenon is tied directly to deformation-related volume changes.

Although fluid flow is not explicitly simulated, these fluid dynamics are significant and are represented through these volume changes. Additionally, shear strain, which describes changes in shape, also plays a pivotal role. Integrating both volume change and shape change in the analysis, the use of equivalent strain provides a more comprehensive understanding of the mechanical conditions essential for tissue differentiation.

The total strain is defined through the formula below [47], [48].

$$\sigma_{total} = \frac{2}{3} \cdot \sigma_{deviatoric} + \frac{1}{3} \cdot \sigma_{hydrostatic} \tag{3}$$

The first term represents the deviatoric strain, which accounts for the distortion or shape change in the solid material. The second term corresponds to the hydrostatic strain, which describes the volumetric change in the semi-fluid tissue that develops. For simplicity, fluid flow has been neglected in this model. Consequently, the total strains are conventionally modeled through the equivalent total strain, encompassing both the deviatoric and hydrostatic components.

Considering all the above, through an extensive review of the literature, the equivalent strain boundaries have been summarized as follows:

Table 3: Summarized strain boundaries at each stage

Current Tissue	**Next Tissue**	$\boldsymbol{\varepsilon_{low}}$ $\left(\frac{\boldsymbol{mm}}{\boldsymbol{mm}}\right)$	$\boldsymbol{\varepsilon_{max}}$ $\left(\frac{\boldsymbol{mm}}{\boldsymbol{mm}}\right)$
Granulation	Cartilage	0.025	0.05
Cartilage	Immature	0.025	0.01
Immature	Mature	0.01	0.0004
Mature	–	–	–

3. Homogenization Techniques in Scaffold Analysis

3.1. Robustness of Homogenization Softwares

This chapter examines the robustness of the homogenization techniques being employed. It focuses on evaluating the consistency and accuracy of these methods across different structural configurations and materials. This exploration aims to identify key factors influencing the performance of homogenization methods.

3.1.1. Deterministic Homogenization: nTopology vs ANSYS Material Designer

This section explores the concept of deterministic lattice homogenization by conducting analyses on a unit cell using nTopology and comparing the results to those obtained from ANSYS Material Designer. Homogenization is performed on the same unit cell in both software platforms to evaluate their accuracy and reliability. The results are then compared to established data from the literature to further validate the findings and ensure the robustness of the homogenization techniques employed.

For all the following homogenization analyses, the application of periodic boundary conditions was considered. Periodic boundary conditions involve replicating the unit cell in all directions to simulate an infinite material. This approach ensures that the mechanical response of the unit cell is representative of the entire material by eliminating edge effects and providing a more accurate depiction of the material's behavior under load. Applying these conditions helps in achieving more reliable and consistent results in homogenization studies.

The first unit cell being tested, concerns a simple cubic geometry with internal void structure by Chauhan et al. [49].

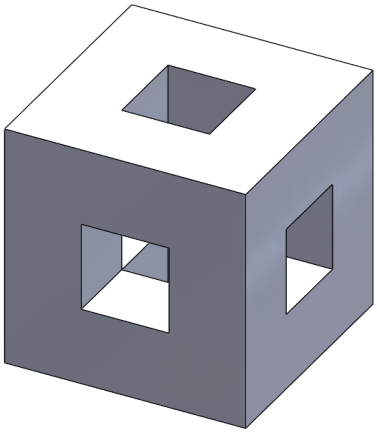

Figure 33: Cubic geometry with internal void structure by Chauhan et al.

The material used in the paper, and as an extent to the analyses, is presented in Table 4.

Table 4: Material properties used in paper by Chauhan et al.

$\boldsymbol{E}$ $\boldsymbol{(GPa)}$	$\boldsymbol{\nu}$
70	0.3

According to the table provided by this study, it is expected that this particular unit cell with a porosity of $\Phi = 30\%$ has a relative effective young's modulus of approximately:

$$E_{relative,literature} = \frac{E_{homogenized}}{E_{original,material}} = 0.4926 \quad (4)$$

A homogenization is thus conducted in nTopology, using the aforementioned material properties and geometry as presented in Figure 33 and Table 4.

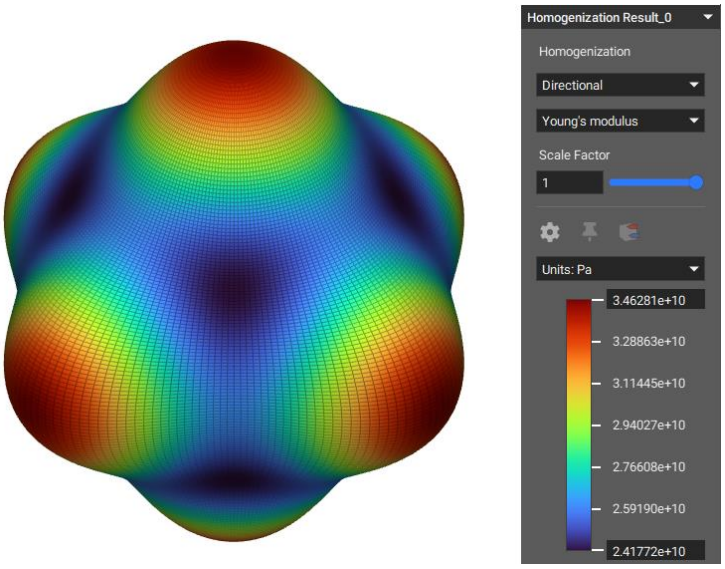

Figure 34: Result of unit cell homogenization by Chauhan et al. at nTopology

The relative effective young's modulus of this unit cell, according to nTopology, is thus:

$$E_{relative,nTop} = \frac{E_{homogenized}}{E_{original,material}} = \frac{3.46 \cdot 10^{10}\ (Pa)}{7 \cdot 10^{10}\ (Pa)} = 0.4942 \quad (5)$$

The same geometry and material properties were input in ANSYS Material Designer. The results are presented in Table 5.

Table 5: Chauhan et al unit cell homogenization results - ANSYS Material Designer

$E_1\ (GPa)$	$E_2\ (GPa)$	$E_3\ (GPa)$	$G_{12}\ (GPa)$	$G_{23}\ (GPa)$	$G_{31}\ (GPa)$	ν_{12}	ν_{13}	ν_{23}
34.913	34.914	34.915	9.460	9.463	9.460	0.2	0.2	0.2

The relative effective young's modulus of this unit cell, according to ANSYS Material Designer, is thus:

$$E_{relative,nTop} = \frac{E_{homogenized}}{E_{original,material}} = \frac{3.49 \cdot 10^{10}\ (Pa)}{7 \cdot 10^{10}\ (Pa)} = 0.4986 \qquad (6)$$

The results are summarized in Table 6, alongside the relative error of each simulation software when compared to the respective value referenced in the literature.

Table 6: Summarized homogenization results by Chauhan et al.

	$E_{relative}$	$e_{relative}\ (\%)$
Chauhan et al.	0.4926	–
nTopology	0.4942	0.32
ANSYS Material Designer	0.4986	1.22

The analysis of the simple cubic structure demonstrates that both software platforms yield similar results, indicating their reliability, accuracy and robustness.

However, it would be beneficial to also examine more complex and anisotropic geometries. This is done in the form of the studies conducted by Sorohan et al. and Miller et al. [50], [51]. These papers study a re-entrant honeycomb REV.

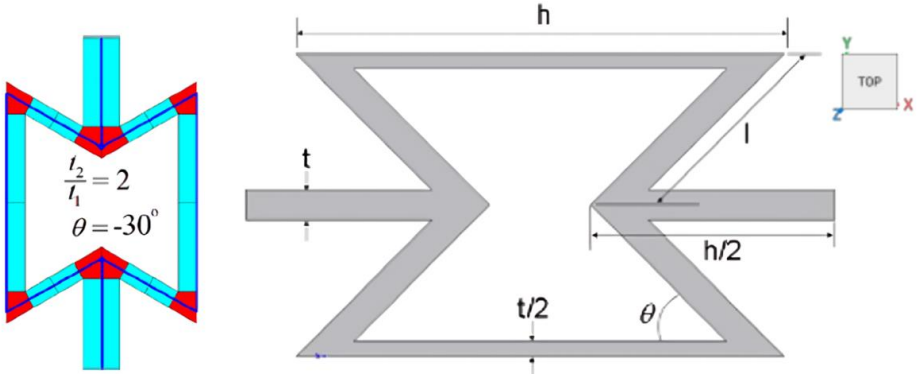

Figure 35: Re-entrant honeycomb cell, showing geometric parameters

The geometrical dimensions used are summarized below.

Table 7: Geometrical dimensions of re-entrant honeycomb cell by Sorohan et al.

$t\ (mm)$	$l\ (mm)$	$h\ (mm)$	$b\ (mm)$	$\theta\ (^o)$
3	19.45	34.26	20	-45

The material used in the paper, and as an extent to the analyses, is presented in Table 8.

Table 8: Material properties used in paper by Sorohan et al.

E (GPa)	ν	ρ (kg/m^3)
2.5	0.35	1000

A homogenization is thus conducted in nTopology, using the aforementioned material properties and geometry as presented in Figure 35, Table 7 and Table 8.

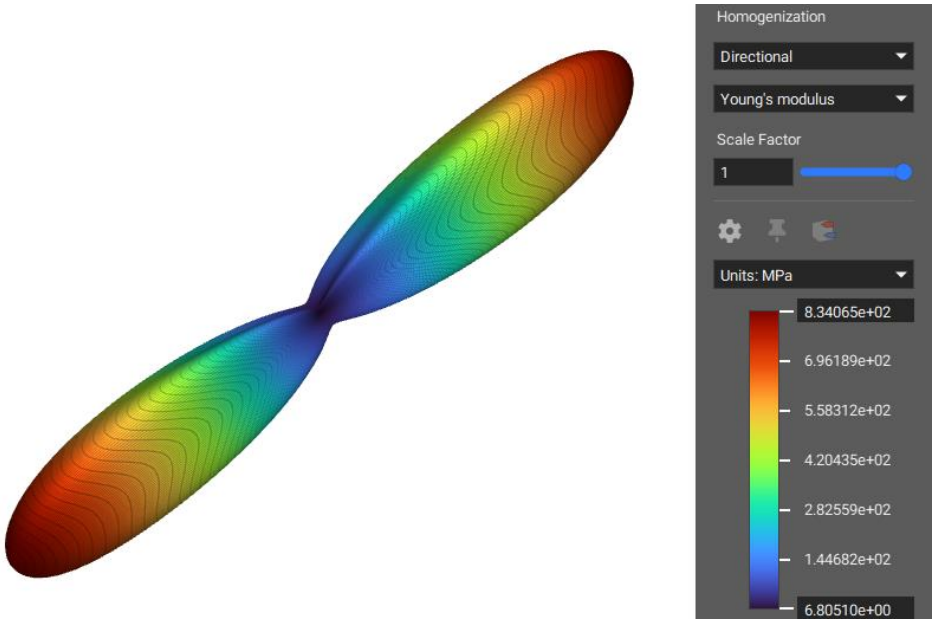

Figure 36: Result of unit cell homogenization by Sorohan et al. at nTopology

In the stiffness matrix, the presence of many zeros in the non-diagonal elements typically indicates that the material exhibits isotropic properties. This means that the material's mechanical properties are uniform in all directions. For anisotropic materials, like this one, the stiffness matrix contains non-zero elements in the non-diagonal positions. These non-zero elements reflect the material's directional

dependencies, indicating that the response to a vertical force involves not only vertical deformation but also rotations and shear deformations.

In this case, the unit cell is anisotropic, and thus the derivation of the directions Young's Moduli is not straightforward in nTopology. Thus, the stiffness matrix is being utilized in this case, directly as extracted from nTopology.

$$C = \begin{bmatrix} 1.43 \cdot 10^{8} & -8.97 \cdot 10^{7} & 1.86 \cdot 10^{7} & 7.12 & 127.24 & -74.76 \\ -8.96 \cdot 10^{7} & 7.64 \cdot 10^{7} & -4.57 \cdot 10^{6} & -182.19 & -57.26 & 100.63 \\ 1.86 \cdot 10^{7} & -4.57 \cdot 10^{6} & 8.39 \cdot 10^{8} & -391.07 & -262.07 & 421.01 \\ 7.12 & -182.19 & -391.07 & 2.23 \cdot 10^{6} & -51.88 & 122.59 \\ 127.24 & -57.26 & -262.89 & -51.88 & 9.8 \cdot 10^{7} & -906.46 \\ -74.76 & 100.63 & 421.01 & 122.59 & -906.46 & 6.44 \cdot 10^{7} \end{bmatrix} \quad (7)$$

Then, it is required to calculate the compliance matrix, which is defined as follows [52].

$$S = C^{-1} \quad (8)$$

Thus:

$$S = \begin{bmatrix} 2.65 \cdot 10^{-8} & 3.11 \cdot 10^{-8} & -4.19 \cdot 10^{-10} & 2.38 \cdot 10^{-12} & -1.74 \cdot 10^{-14} & -1.50 \cdot 10^{-14} \\ 3.11 \cdot 10^{-8} & 4.95 \cdot 10^{-8} & -4.19 \cdot 10^{-10} & 3.87 \cdot 10^{-12} & -1.25 \cdot 10^{-14} & -3.86 \cdot 10^{-14} \\ -4.19 \cdot 10^{-10} & -4.19 \cdot 10^{-10} & 1.20 \cdot 10^{-9} & 1.77 \cdot 10^{-13} & 3.52 \cdot 10^{-15} & -7.67 \cdot 10^{-15} \\ 2.38 \cdot 10^{-12} & 3.87 \cdot 10^{-12} & 1.77 \cdot 10^{-13} & 4.48 \cdot 10^{-7} & 2.37 \cdot 10^{-13} & -8.54 \cdot 10^{-13} \\ -1.74 \cdot 10^{-14} & -1.25 \cdot 10^{-14} & 3.52 \cdot 10^{-15} & 2.37 \cdot 10^{-13} & 1.02 \cdot 10^{-8} & 1.44 \cdot 10^{-13} \\ -1.50 \cdot 10^{-14} & -3.86 \cdot 10^{-14} & -7.67 \cdot 10^{-15} & -8.54 \cdot 10^{-13} & 1.44 \cdot 10^{-13} & 1.55 \cdot 10^{-8} \end{bmatrix} \quad (9)$$

To determine the directional Young's moduli E_x, E_y, and E_z along the X, Y, and Z axes, respectively, the inverse of this stiffness matrix C was computed to obtain the compliance matrix S. The elements S_{11}, S_{22}, and S_{33} of the compliance matrix directly provide the reciprocals of the directional Young's moduli. The calculations yielded the following values [52]:

$$E_x = \frac{1}{S_{11}} = \frac{1}{2.653 \times 10^{-8}} \approx 37.7 \times 10^{6} \text{ Pa} \quad (10)$$

$$E_y = \frac{1}{S_{22}} = \frac{1}{4.956 \times 10^{-8}} \approx 20.2 \times 10^{6} \text{ Pa} \quad (11)$$

$$E_z = \frac{1}{S_{33}} = \frac{1}{1.198 \times 10^{-9}} \approx 834.1 \times 10^{6} \text{ Pa} \quad (12)$$

The Poisson's ratios ν_{xy}, ν_{xz}, and ν_{yz} are calculated to assess the material's response under uniaxial stress, indicating the negative ratio of transverse strain to axial strain in perpendicular directions. For an anisotropic material represented by the compliance matrix S, these ratios are defined as follows:

$$\nu_{xy} = -\frac{S_{12}}{S_{11}} = -1.172 \tag{13}$$

$$\nu_{xz} = -\frac{S_{13}}{S_{11}} = 0.016 \tag{14}$$

$$\nu_{yz} = -\frac{S_{23}}{S_{22}} = 0.008 \tag{15}$$

A homogenization analysis is also performed using the same geometry and material properties in ANSYS Material Designer. In this software, the results are provided directly, eliminating the need for additional calculations. The results of all the aforementioned strategies are summarized in Table 9.

Table 9: Summarized homogenization results regarding the study by Sorohan et al.

	nTopology	**ANSYS Material Designer**	**Sorohan et al.**
$\boldsymbol{E_x = E_2\ (MPa)}$	37.7	34.7	$20 - 40$
$\boldsymbol{E_y = E_1\ (MPa)}$	20.2	18.2	$11 - 27$
$\boldsymbol{E_z = E_3\ (MPa)}$	834.1	849	$896 - 973$
$\boldsymbol{\rho\ (kg/m^3)}$	340	340	$360 - 400$
$\boldsymbol{\nu_{xy}}$	-1.172	-1.2	$(-1) - (-1.2)$
$\boldsymbol{\nu_{xz}}$	0.016	0.014	$0.0104 - 0.04$
$\boldsymbol{\nu_{yz}}$	0.008	0.0075	$0.0078 - 0.016$

Both ANSYS Material Designer and nTopology have yielded results that are consistent with the literature, demonstrating their robustness in homogenization analysis.

However, nTopology is selected for further analysis because it offers the option to model stochastic Voronoi lattices, a feature that is not available in ANSYS Material Designer. This capability is crucial for the specific requirements of the study.

3.1.2. Evaluation of Homogenization on Deterministic Lattices

First, it was verified that deterministic structures, such as honeycomb lattices converge in homogenization. Specifically, this involves confirming that a single deterministic representative volume element (REV) produces the same homogenization results as multiple units. It is important that the relative volume, defined as the ratio of lattice to bounding box volume, remains constant regardless of the lattices number.

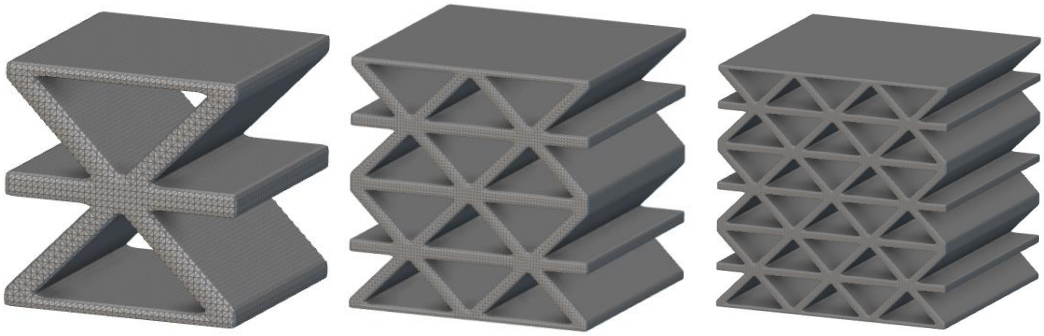

Figure 37: Honeycomb lattices under examination

The directional homogenization result for the single honeycomb REV is shown below.

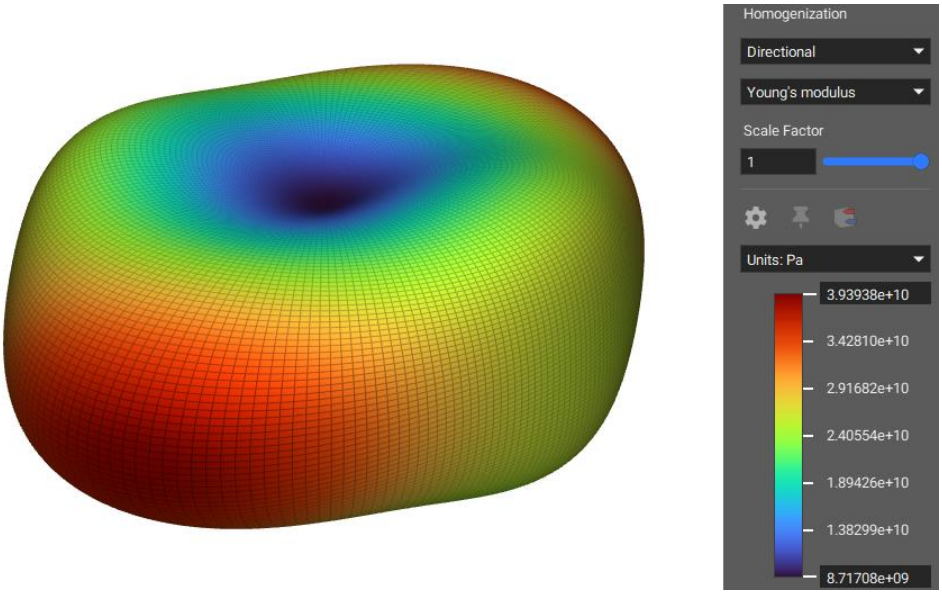

Figure 38: Homogenization result for single honeycomb REV

The directional homogenization result for the four honeycomb REVs is shown below.

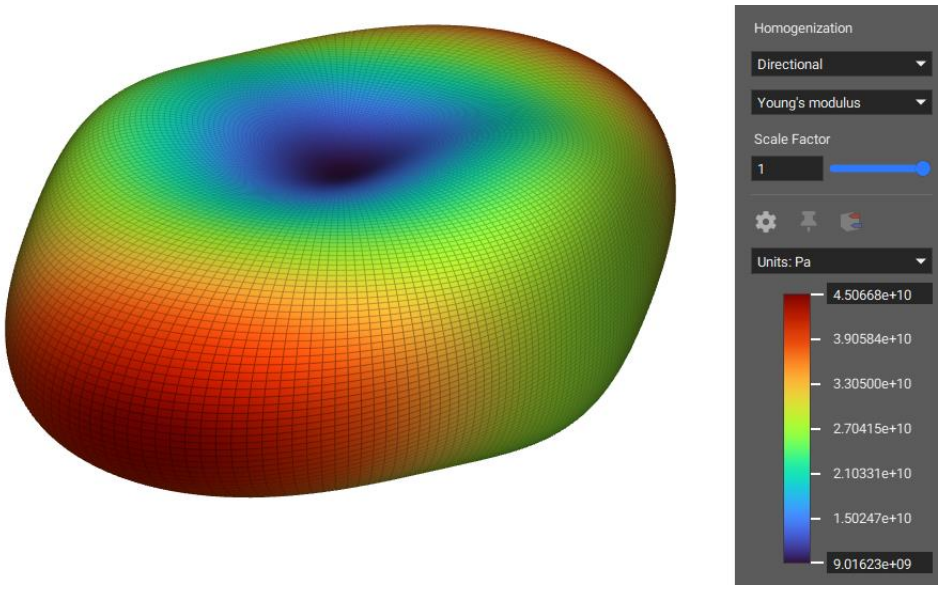

Figure 39: Homogenization result for four honeycomb REVs

The directional homogenization result for the nine honeycomb REVs is shown below.

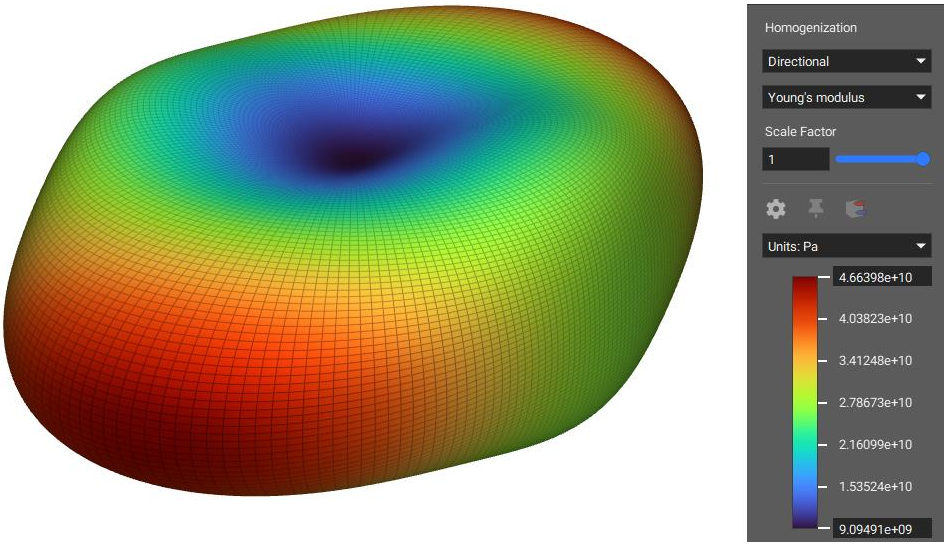

Figure 40: Homogenization result for nine honeycomb REVs

3.2. Homogenization of Voronoi Stochastic Lattices

3.2.1. Materials Employed for Voronoi Homogenization

The same verification was necessary for Voronoi structures, which are inherently stochastic and thus more complex. Initially, a direct simulation without homogenization was considered, but this approach proved impractical due to the enormous computational power required.

A detailed study was conducted to determine the density required for a Voronoi "unit cell" to achieve stiffness convergence, establishing these as the unit cells. It was essential to achieve nondimensionalization of the seed number to ensure that the representative volume element (REV) had converged. Smaller bounding boxes of the REV did not meet this criterion, as the variation was too significant and the lattice density was insufficient for convergence. Due to limited computational resources, a trial-and-error approach was employed for all tissue stages. This involved starting with a specific cube size and testing various seed numbers of Voronoi. If convergence was not achieved, the cube size was increased, resulting in a denser Voronoi lattice, and the process was repeated until convergence was observed. The converged lattice is expected to be orthotropic, exhibiting approximately the same stiffness in the XYZ directions.

First, it is important to retrieve the properties that describe each tissue stage. To this end, the study by Ghiasi et al. and by Kim et al. are investigated and presented below [53], [54].

Table 10: Bone tissue properties of each stage according to Ghiasi et al.

	Cortical Bone	Marrow	Granulation Tissue	Fibrous Tissue	Cartilage	Immature Bone	Mature Bone
Elastic Modulus (MPa)	20,000	2	0.001–2	2	10	1000	6000
Permeability (m^4/Ns)	1E-17	1E-14	1E-14	1E-14	5E-15	1E-13	3.7E-13
Poisson's Ratio	0.3	0.17	0.17	0.17	0.17	0.3	0.3
Solid bulk modulus (MPa)	20,000	2300	2300	2300	3400	20,000	20,000
Fluid bulk modulus (MPa)	2300	2300	2300	2300	2300	2300	2300
Porosity	0.04	0.8	0.8	0.8	0.8	0.8	0.8

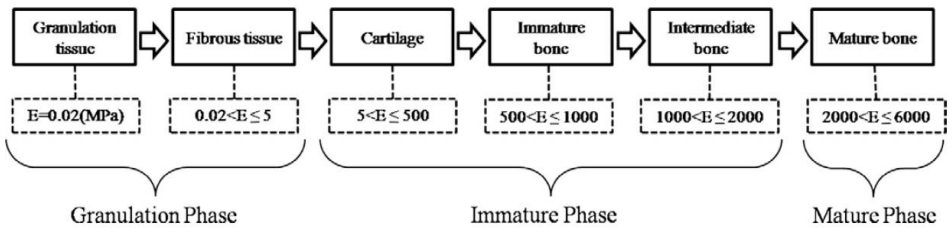

Figure 41: Bone tissue properties of each stage according to Kim et al.

According to the aforementioned studies, the material properties that have been taken into consideration for this study are summarized below.

Table 11: Final bone tissue properties

	$E\ (MPa)$	ν	$\rho\ (kg/m^3)$
Granulation	0.02	0.17	1100
Cartilage	250	0.17	1100
Immature	750	0.3	1800
Mature	4000	0.3	2000

Additionally, it is crucial to consider the material properties of Ti-6Al-4V, as the lattice structure is composed of this material. The material properties have been directly taken from the nTopology material library, and are summarized below.

Table 12: Ti-6Al-4V material properties

$E\ (MPa)$	ν	$\rho\ (kg/m^3)$
113800	0.342	4430

3.2.2. Field Driven Design and Homogenization Strategy

The nTopology software lacks the inherent capability to perform homogenization analysis with multiple materials, leading to significant challenges.

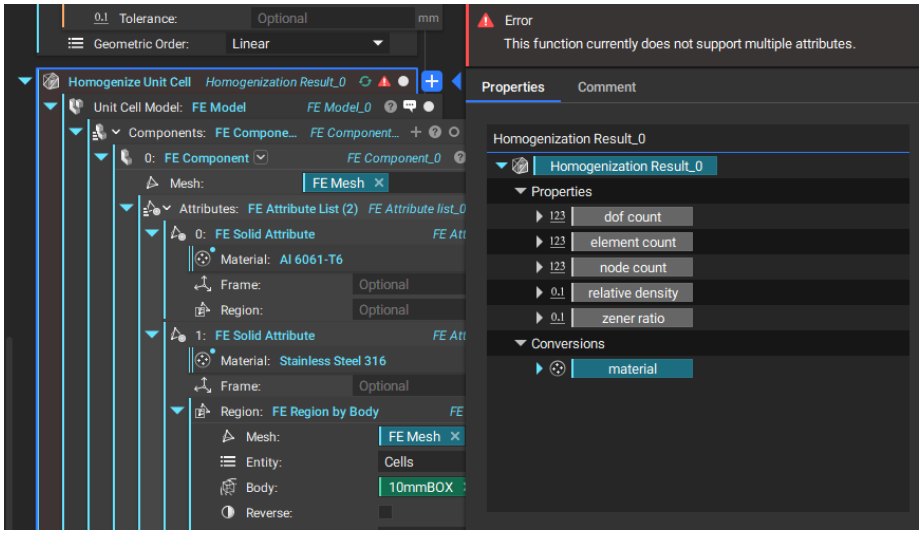

Figure 42: nTopology limitation for 2-material homogenization

To address this limitation, a sophisticated methodology was employed to make nTop perceive the homogenization as being performed on a single material instead of two. A custom material was created with ramped material properties, allowing the inner region to adopt the characteristics of one material and the outer region another. This was achieved using the "ramp" function provided by nTopology, which enables differentiation of a model property as a function of topology. This approach was used in conjunction with the field-driven design offered by nTop. For visualization purposes, the principle of operation will first be explained using the thickness property, and then extended to varying Young's modulus, which is of particular interest in this application.

For clarity, the concept will first be explained using thicknesses and then applied to material properties. A rectangular cell map for the demonstration of the methodology is created, which will then be converted into an implicit body. A point is defined near the center, which is essential in order to define the boundaries of the field driven design.

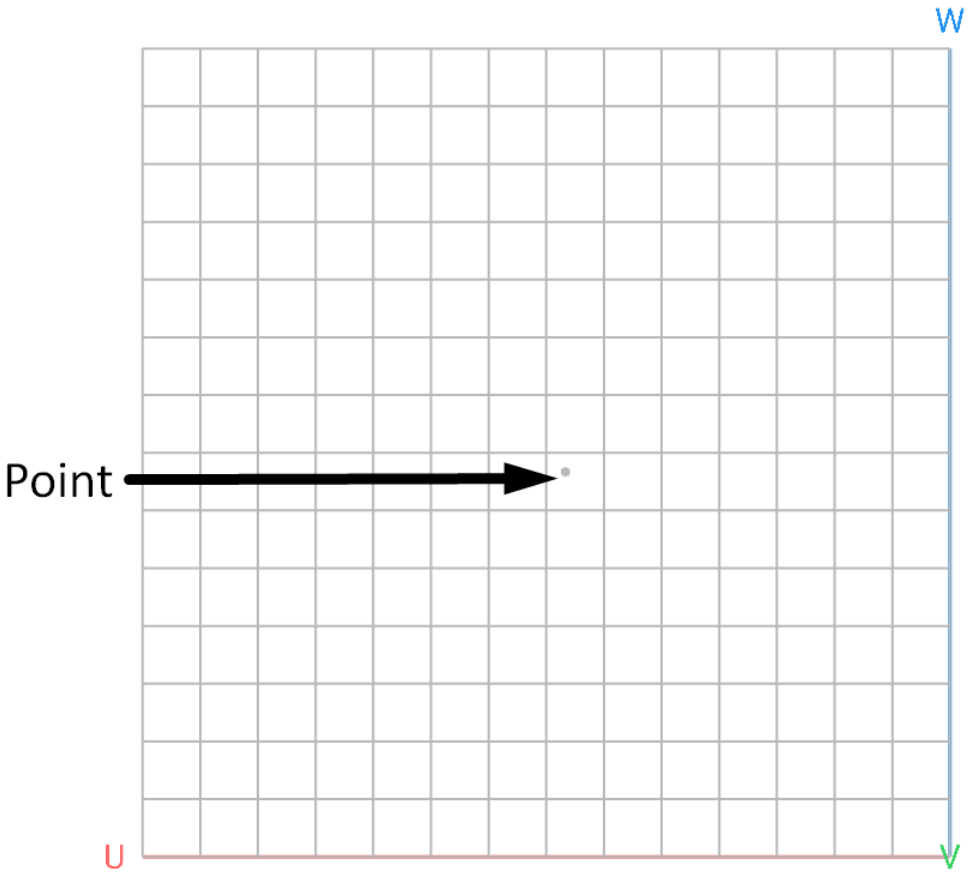

Figure 43: Rectangular cell map alongside middle point

This point can be defined as a reference for the thickness of the cell map, using the "ramp" function.

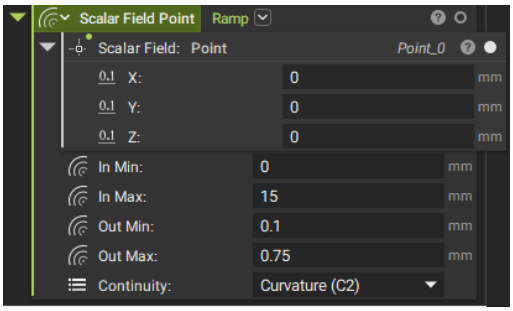

Figure 44: Thickness ramp using a point

In the above image, nTopology is instructed that at a distance of 0mm from a specified point (input minimum), the thickness will be 0.1mm (output minimum). Similarly, at a distance of 15mm from the specified point (input maximum), the thickness will be 0.75mm (output maximum). All intermediate points are adjusted accordingly, using the Curvature (C2) continuity type to ensure a smooth transition. nTopology allows visualization of this process through a field that provides the corresponding value using a probe. For example, in the current case, the described process is illustrated.

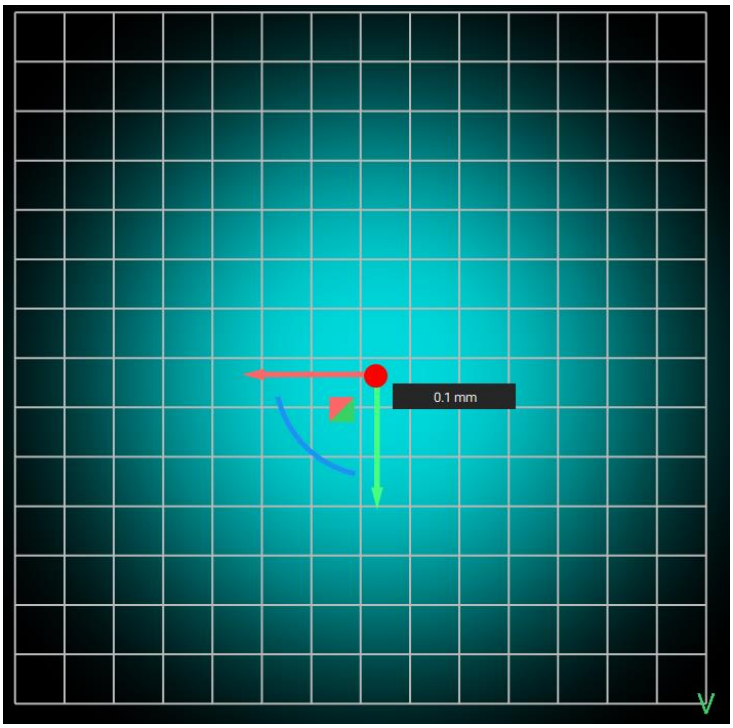

Figure 45: Field driven design: thickness of the cell map on the defined point

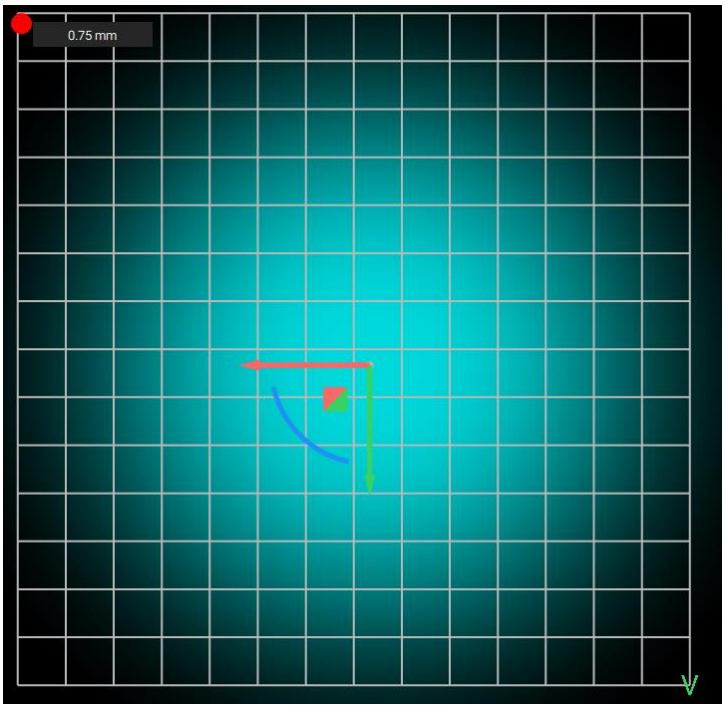

Figure 46: Field driven design: thickness of the cell map at the edge

Figure 47: Field driven design: thickness of the cell map betwween the defined point and the edge

Based on this methodology, the resulting thickness values for the area of interest are as shown below.

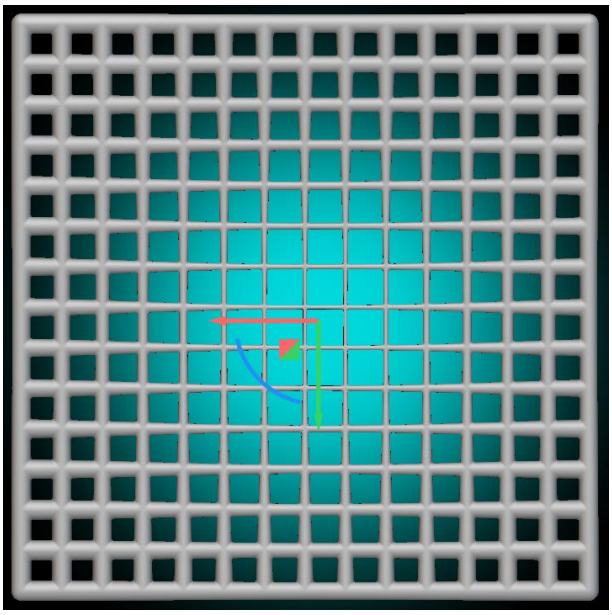

Figure 48: Finalized implicit body based on ramped thickness

The focus will now shift to its application on a volumetric model, which is pertinent to our analysis of Young's modulus, as detailed below. The body highlighted in red is defined accordingly.

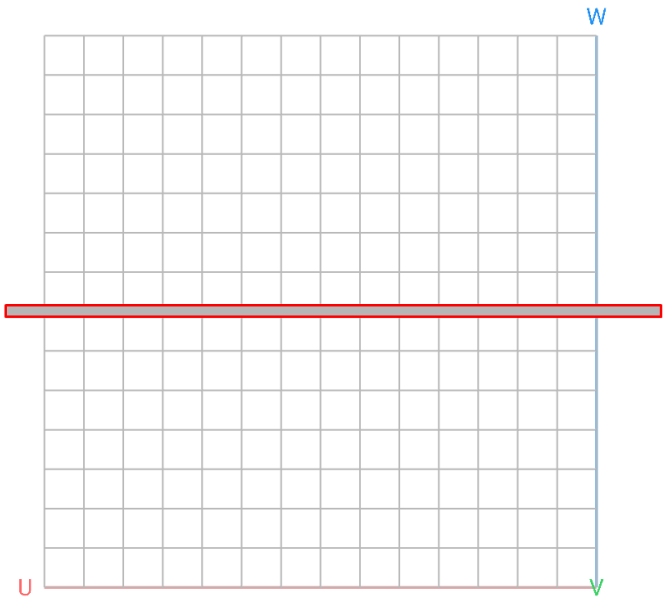

Figure 49: Rectangular cell map alongside defined body

This body can, in a similar manner, be defined as a reference for the thickness of the cell map, using the “ramp” function.

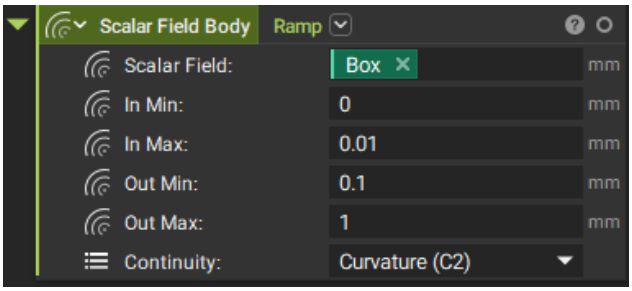

Figure 50: Thickness ramp using a volumetric body

In the image above, nTopology is instructed that at a distance of 0mm from the specified point (input minimum), the thickness will be 0.1mm (output minimum). Similarly, at a distance of 0.01mm from the specified point (input maximum), the thickness will be 0.75mm (output maximum). All intermediate points are adjusted accordingly, utilizing the Curvature (C2) continuity type to ensure a smooth transition.

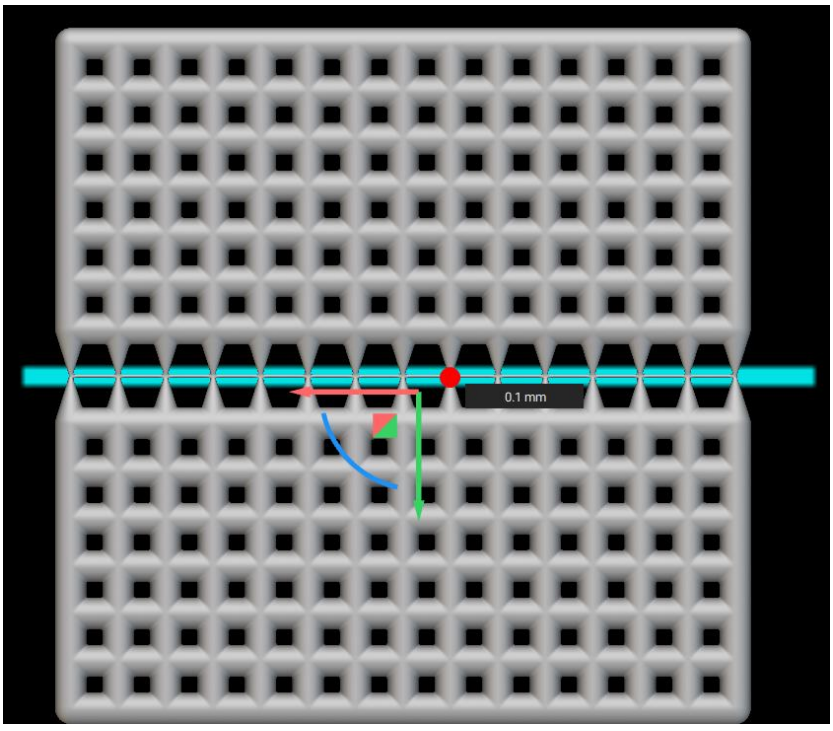

Figure 51: Field driven design: thickness of the cell map on the volumetric body

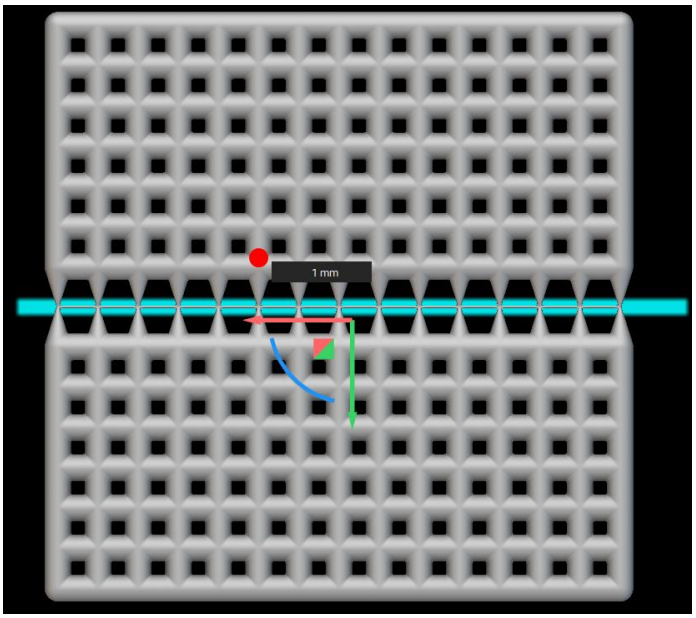

Figure 52: Field driven design: thickness of the cell map away from the volumetric body

This is the exact logic that is followed and applied to model the tissue ingrowth. First, the lattice is defined. In this case, the 60% porosity lattice will be indicatively used.

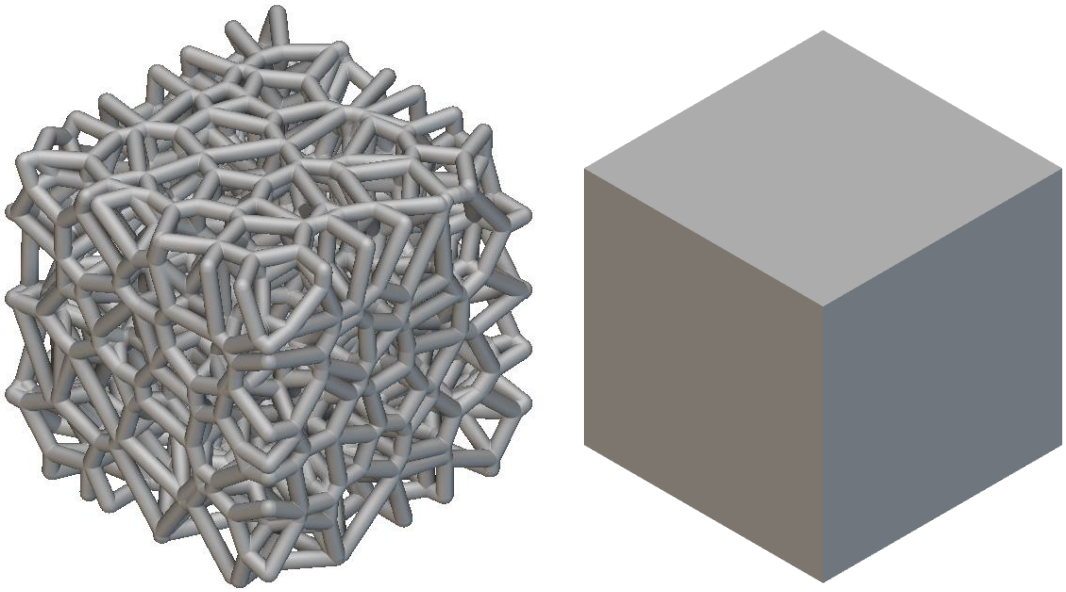

Figure 53: Indicative 60% porosity lattice alongside bounding box for field driven design

To adhere to this logic, a solid cube is used in the homogenization process. nTop is instructed to adjust the cube's properties based on the different Voronoi implicit body. Consequently, Young's Modulus is defined in the ramp function as follows.

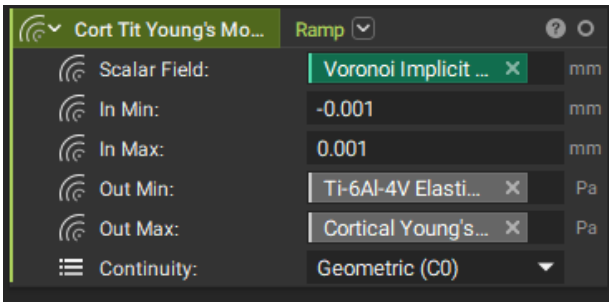

Figure 54: Young's modulus ramp using a lattice

In the image above, nTopology is instructed that at a distance of -0.001mm from the Voronoi Implicit Body (input minimum), the Young's Modulus will be equal to the Ti-6Al-4V Elastic Modulus (output minimum). Similarly, at a distance greater than 0.001mm from the Voronoi Implicit Body (input maximum), the Young's Modulus will correspond to the Cortical Bone's Young's Modulus (output maximum). All intermediate points are adjusted accordingly, utilizing Geometric continuity (C0) to ensure a steep transition, effectively simulating the presence of two distinct materials.

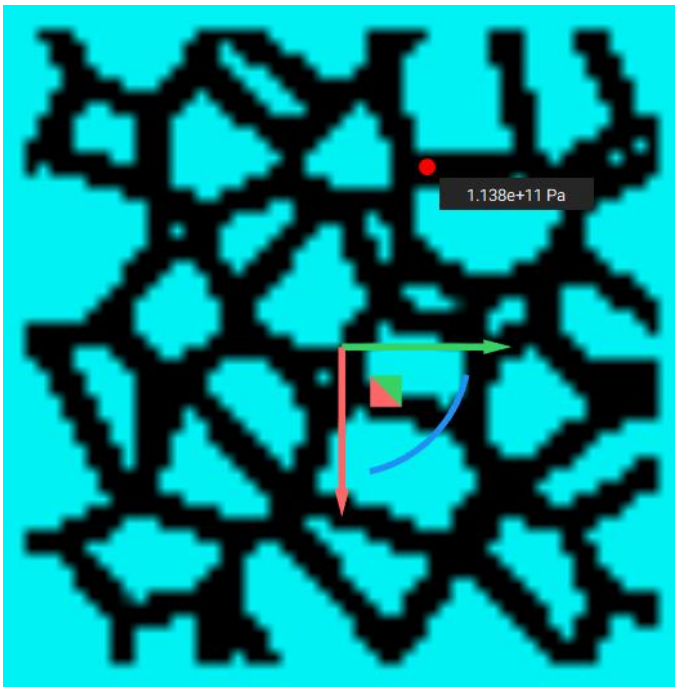

Figure 55: Field driven design: Young's modulus near the lattice at section view

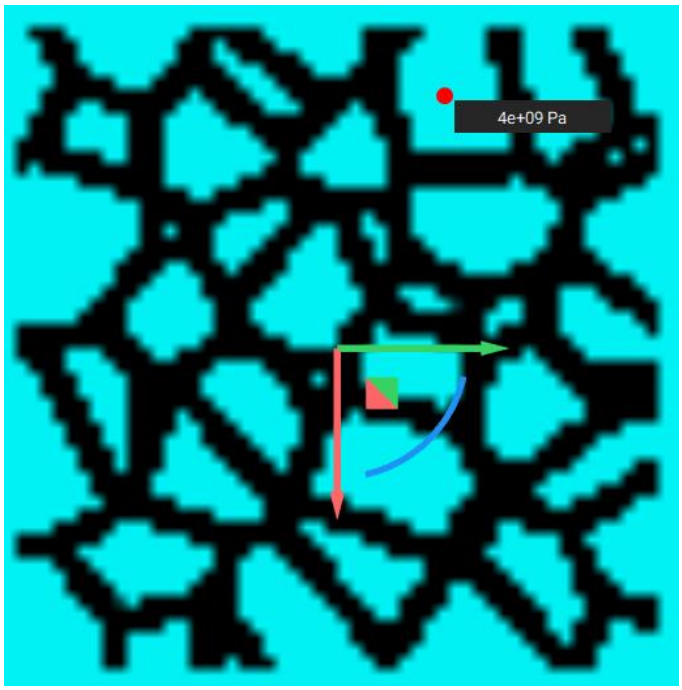

Figure 56: Field driven design: Young's modulus away from the lattice at section view

At the Voronoi site, the Young's Modulus of Ti-6Al-4V has been successfully defined, while the outer regions correspond to that of bone. The black color indicates the Young's Modulus of Ti-6Al-4V, while the blue represents that of bone. Verification confirms that the black profile accurately follows the Voronoi geometry, demonstrating the effectiveness of the methodology.

The same concept was applied to the magnitudes of Poisson's ratio and density.

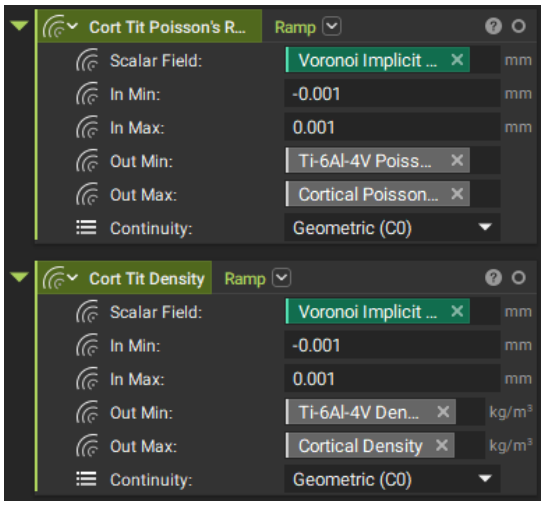

Figure 57: Poisson's ratio and density ramps using the lattice

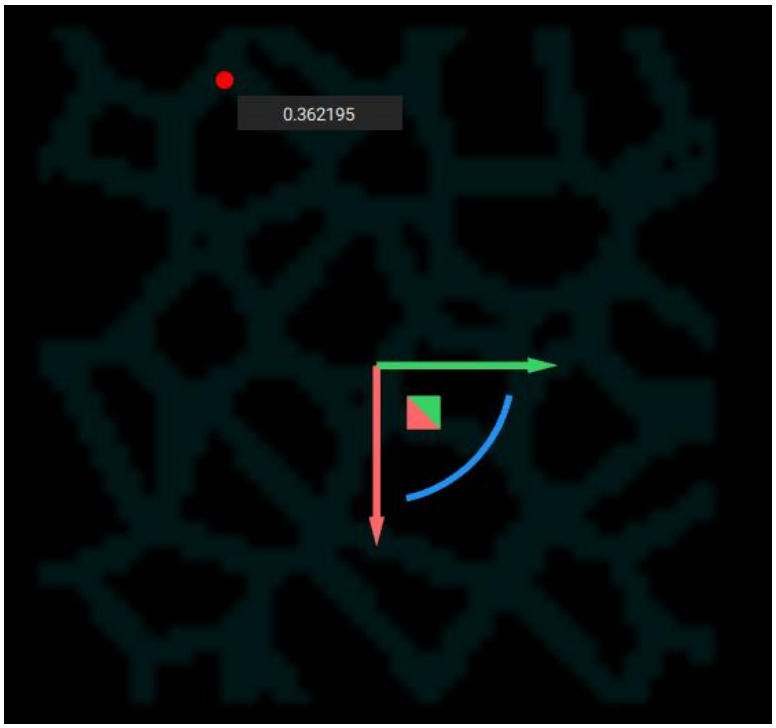

Figure 58: Field driven design: Poisson's ratio near the lattice at section view

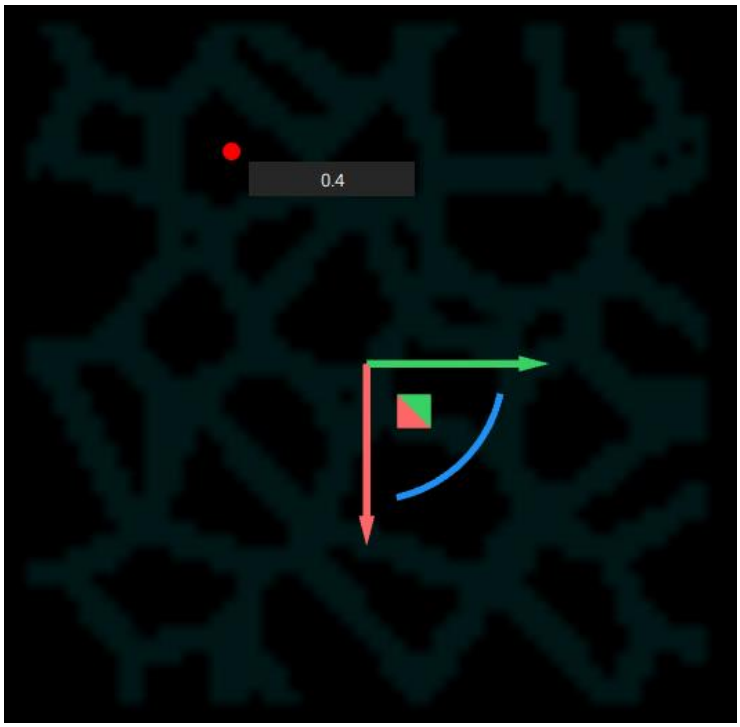

Figure 59: Field driven design: Poisson's ratio away from the lattice at section view

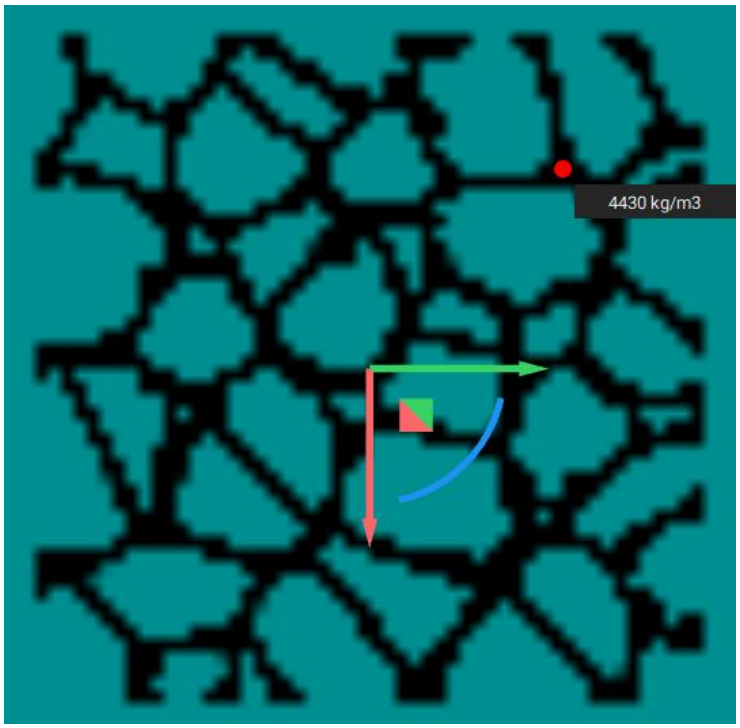

Figure 60: Field driven design: Density near the lattice at section view

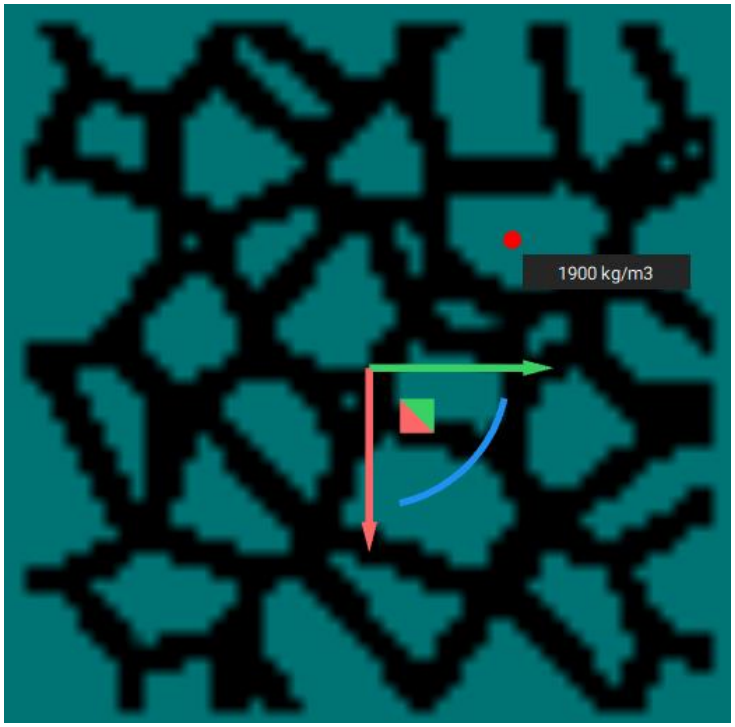

Figure 61: Field driven design: Density away from the lattice at section view

The idea is that with a minimal assumption, it is possible to define the desired properties within a single implicit body (the cube) and a unified geometry by using variable properties around the Voronoi lattice topology. This approach effectively guides nTop into performing dual-material homogenization correctly. The limitation of this method is not applicable for homogenization involving three or more materials.

3.2.3. Indicative Detailed Results of Voronoi Homogenization at 80% Porosity

The field-driven design technique was subsequently applied to all tissue stages. In this section, a representative porosity of 80% is selected to analyze and discuss the results in detail.

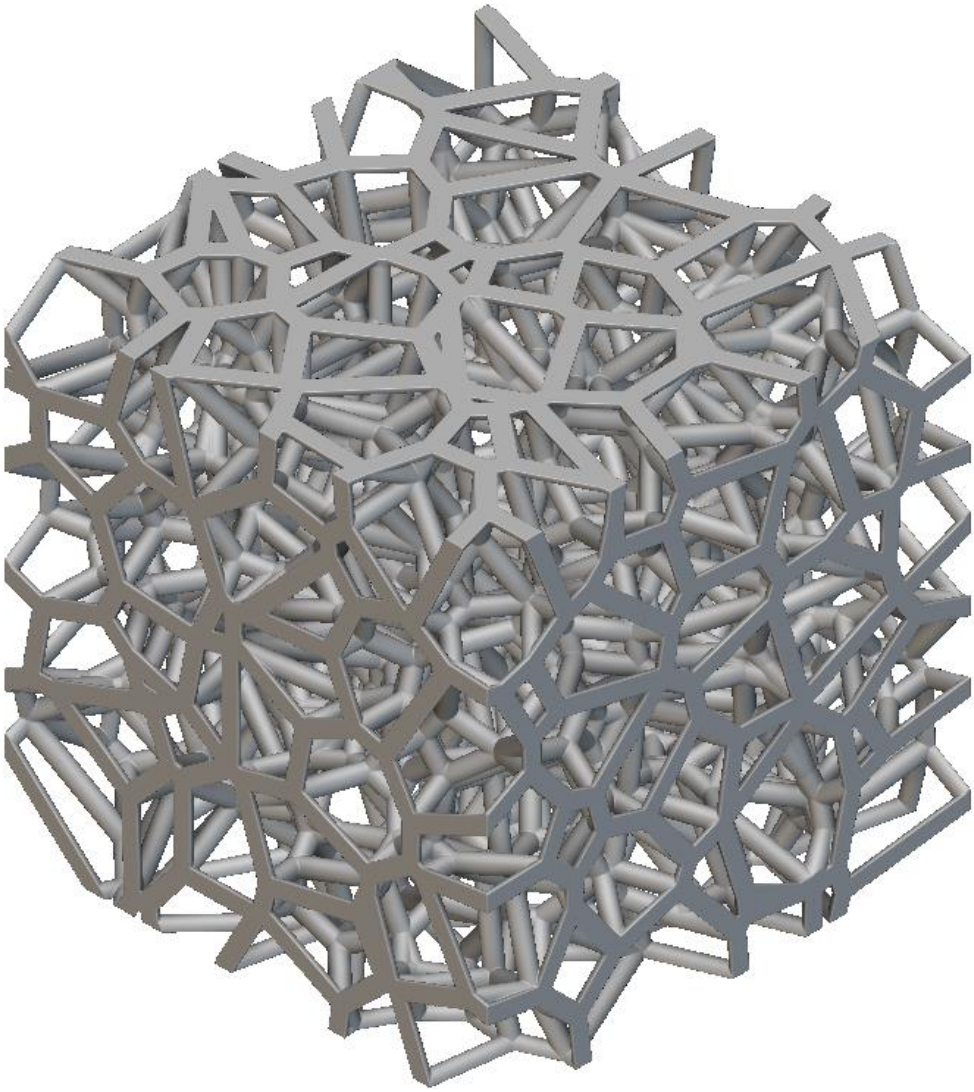

Figure 62: Voronoi lattice at 80% porosity

Initially, three random seeds are selected within a cube with a side length of 14.5mm at the granulation stage. The objective is to determine whether the cube is sufficiently large and dense to achieve homogenization convergence of the Young's moduli of the stochastic lattice.

The logic of this method is that achieving convergence during the granulation phase suggests that later stages, when the tissue hardens, will similarly show convergence. This assumption bolsters confidence in the consistent behavior of the material throughout all phases of bone maturation.

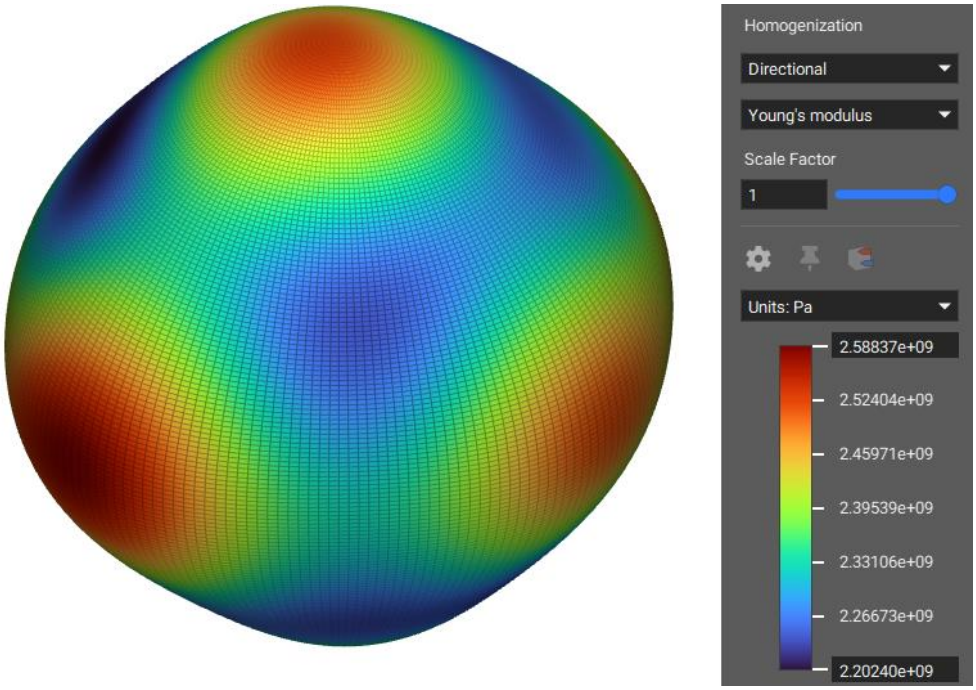

Figure 63: Granulation and Ti-6Al-4V lattice homogenized material at 80% porosity; Seed number 1

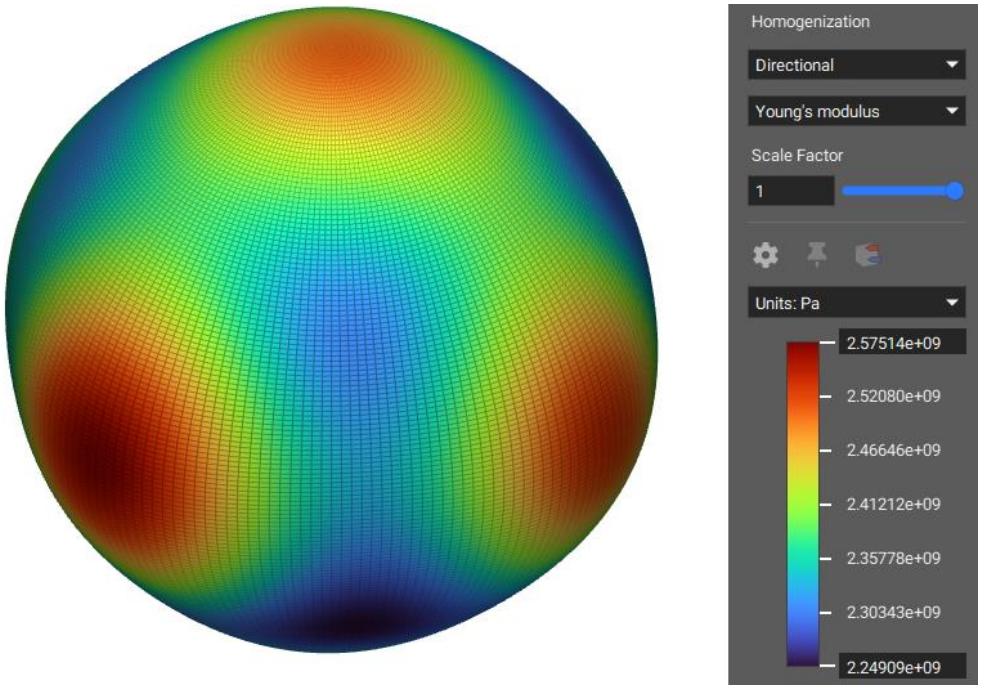

Figure 64: Granulation and Ti-6Al-4V lattice homogenized material at 80% porosity; Seed number 2

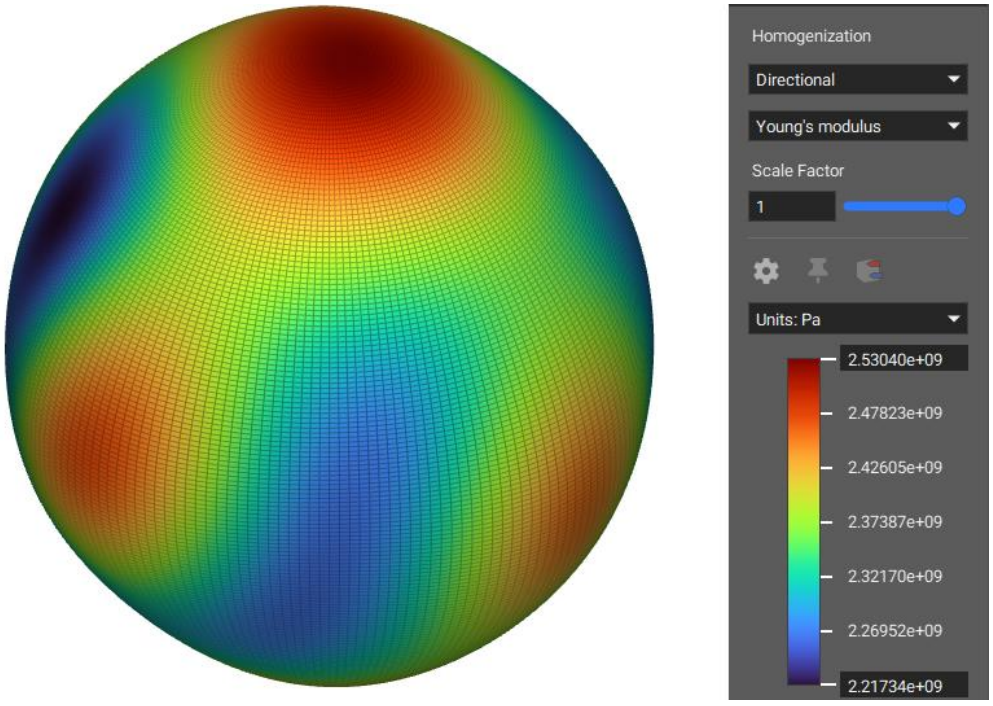

Figure 65: Granulation and Ti-6Al-4V lattice homogenized material at 80% porosity; Seed number 3

From the homogenized materials, it is observed that they exhibit isotropic properties, indicating that Young's modulus is uniform in the X, Y, and Z directions. The similarity of results across these directions underscores the robustness of the homogenization strategy, confirming that the cube's size is adequate for the Voronoi model to achieve convergence. These findings not only validate the effectiveness of the method but also highlight the cube's sufficiency in ensuring accurate simulations. The detailed comparison and further discussion of these results will be presented in the next section, where they will be analyzed relative to one another to draw more comprehensive conclusions.

After verifying convergence in the granulation phase, it is deemed safe to proceed to the cartilage, immature, and mature tissue stages with confidence in their likely convergence. This progression suggests that the methodologies applied are robust across different stages of tissue development, ensuring reliable simulations. The results from these subsequent stages, which are expected to demonstrate similar convergence, are presented below. This consistency reinforces the efficacy of the approach throughout the various phases of tissue maturation.

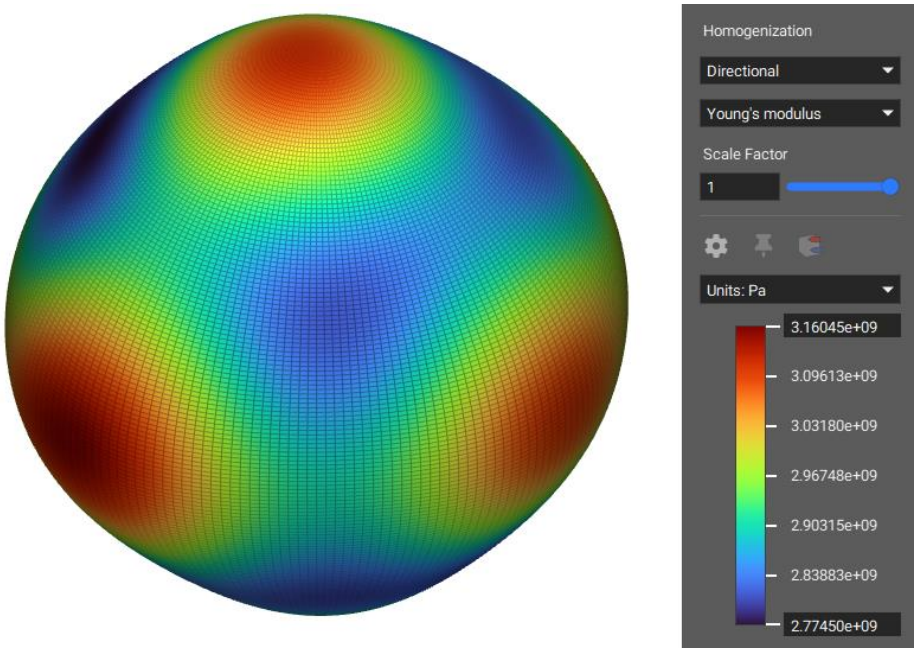

Figure 66: Cartilage and Ti-6Al-4V lattice homogenized material at 80% porosity

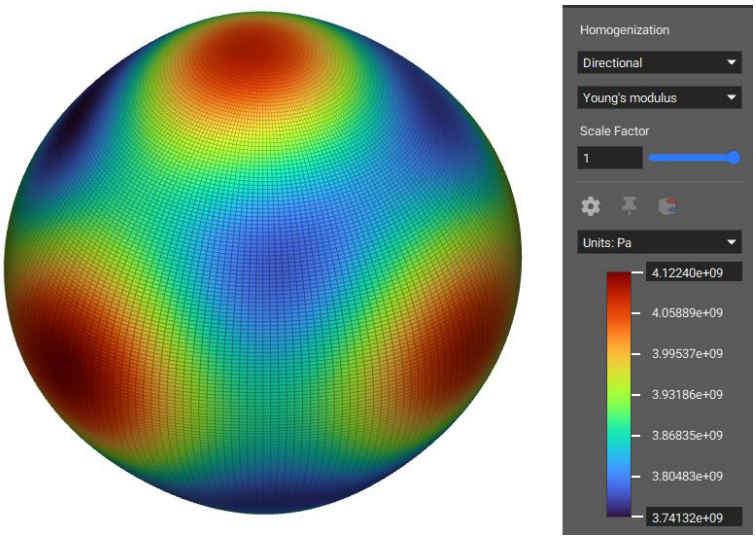

Figure 67: Immature and Ti-6Al-4V lattice homogenized material at 80% porosity

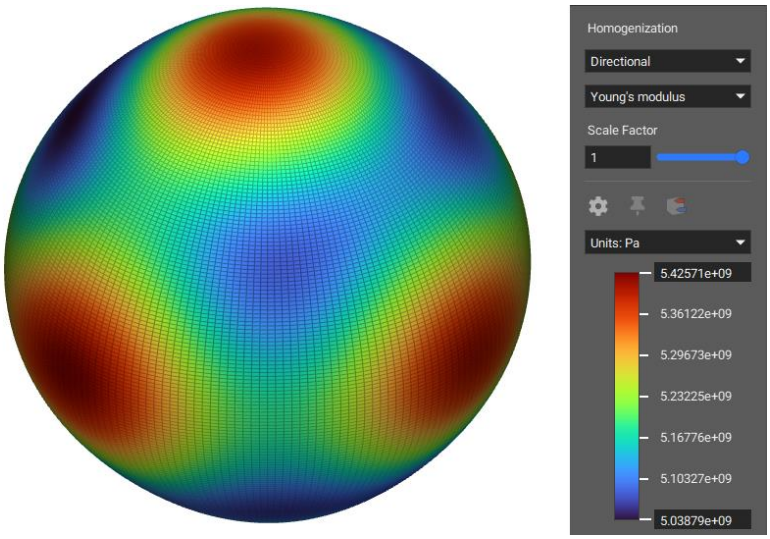

Figure 68: Mature and Ti-6Al-4V lattice homogenized material at 80% porosity

As the tissue progresses through different stages of hardening, the material demonstrates increasing isotropy and stiffness, further substantiating the effectiveness of the applied homogenization approach. This trend towards isotropy with the hardening of the tissue indicates a uniform response in mechanical properties across all spatial directions, which is crucial for the integrity and functionality of the material in biological applications. Such consistent behavior not only validates the homogenization methods used but also underscores the reliability of using these materials in real-world scenarios where isotropic properties are often essential.

3.2.4. Summarized Voronoi Homogenization Results & Diagrams for 50-99% Porosities

It is important to note that the diameter of the struts remained unchanged throughout all simulations to maintain the feasibility of printing the lattices [55]. This approach also allowed for focusing on the lattice structure without delving into further complexities of 3D printing technology. The diameter of the strut was constant, and considered equal to:

$$D_{strut} = 0.5\ mm \tag{16}$$

Therefore, the critical factor for evaluating lattice convergence is the variation in point spacing among the seed points. The results are presented below, where CCE the Convergence Cube Edge.

Table 13: Characteristics of the homogenized materials

$\boldsymbol{\Phi}$ (%)	PS (mm)	CCE (mm)
50	1.48	10
51	1.485	10
52	1.51	10
53	1.5325	10
54	1.545	10
55	1.56	10
56	1.6	10
57	1.62	10
58	1.6385	10
59	1.6625	10
60	1.725	10
61	1.735	10
62	1.76	10
63	1.795	11
64	1.82	11
65	1.84	11
66	1.89	12
67	1.93	12

68	1.965	12
69	1.98	12
70	2	13.5
71	2.075	13.5
72	2.125	13.5
73	2.175	13.5
74	2.2	13.5
75	2.275	14.5
76	2.315	14.5
77	2.4	14.5
78	2.45	14.5
79	2.525	14.5
80	2.6	14.5
81	2.7	14.5
82	2.8	14.5
83	2.9	14.5
84	2.95	14.5
85	3.0	14.5
86	3.2	14.5
87	3.4	14.5
88	3.6	15
89	3.8	15
90	3.9	15
91	4.0	15
92	4.2	15
93	4.4	15
94	4.6	15
95	4.8	15.5
96	5.0	16.5
97	6.5	17
98	7	17
99	7.5	17

The relationship between the porosity and the point spacing of the seed points is demonstrated below.

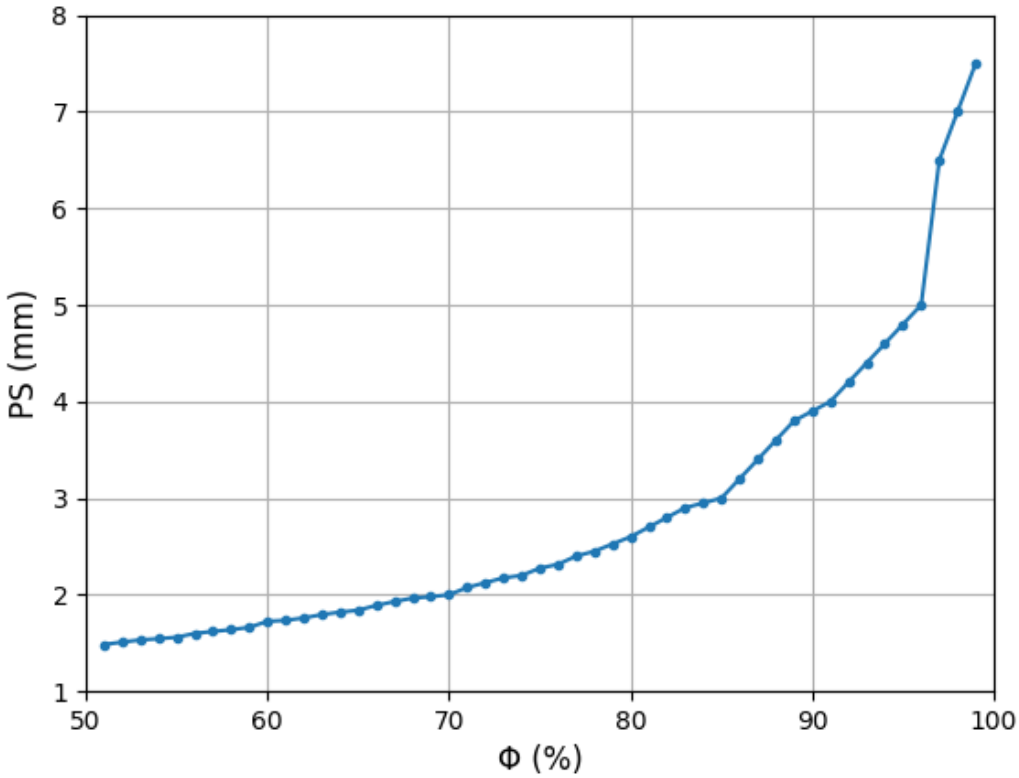

Figure 69: Relationship between porosity and point spacing of seed points

The study focuses on porosity levels ranging from 50% to 90% because, at 50% porosity, the Young's modulus values were approximately 20 GPa, which is comparable to the Young's modulus of natural mature bone. This range was chosen to ensure the material's mechanical properties remain within a biomechanically relevant range, mirroring the stiffness of bone tissue. By maintaining the Young's modulus around 20 GPa, the material is expected to provide adequate support and integration within the bone, avoiding excessively high stiffness that could lead to stress shielding or excessively low stiffness that could compromise structural integrity.

It is important to note that homogenization convergence was only studied in the granulation phase. The rationale behind this approach is that if convergence is achieved in the granulation phase, subsequent stages, where the tissue becomes harder, will also exhibit convergence. This assumption ensures confidence in the material's behavior across all stages of bone maturation. The selected cube sizes for sufficient convergence for each porosity are indicated in Table 13. For the convergence study, 3 different Voronoi seed numbers have been selected.

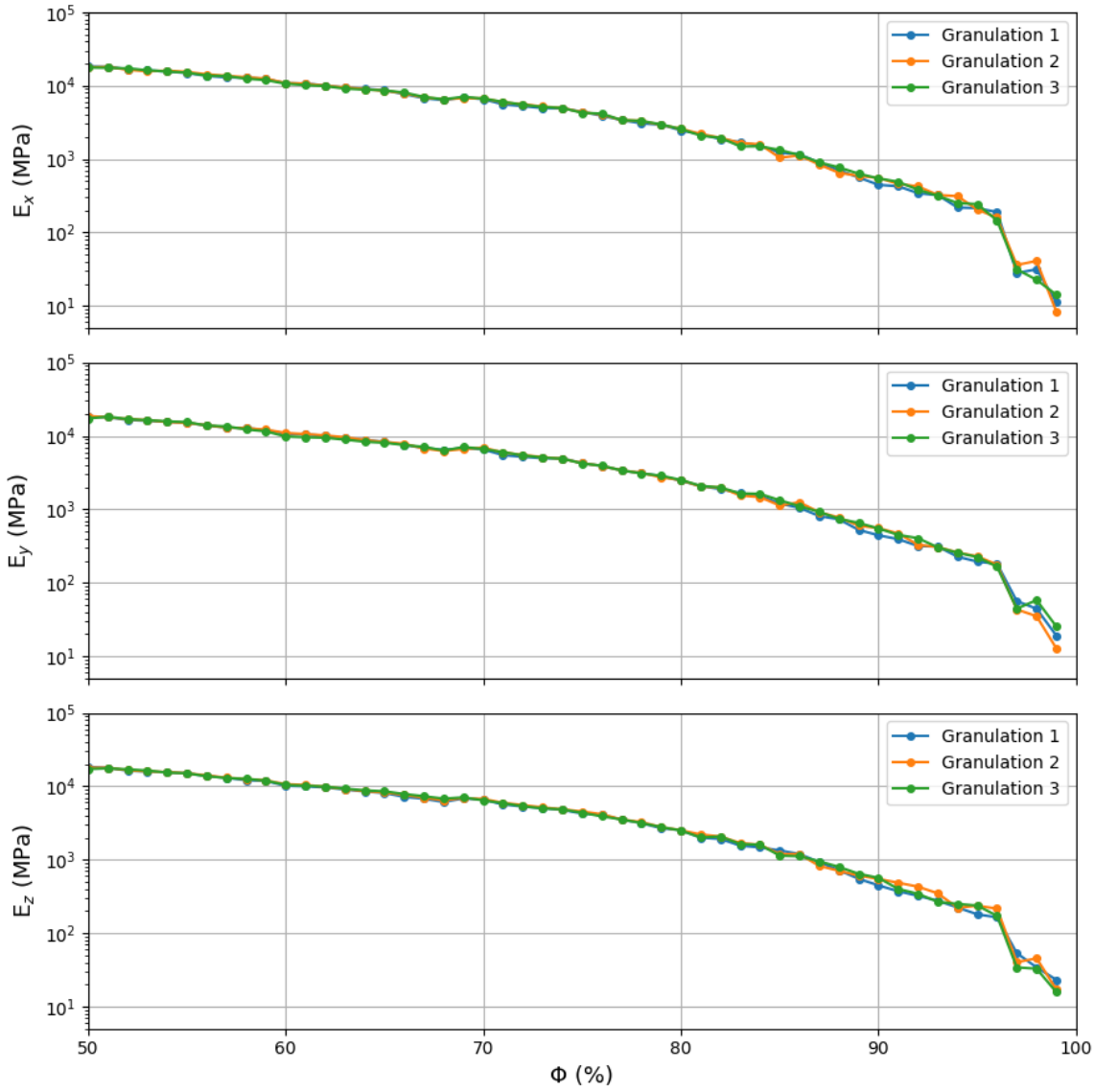

Figure 70: Stiffness moduli as a function of porosity for the three granulation seed numbers

Several important observations and conclusions can be drawn from this study.

The three lines representing different Voronoi seed numbers (Granulation 1, Granulation 2, Granulation 3) are closely aligned across all porosity levels for each directional modulus (E_x, E_y, and E_z). This close alignment indicates that the homogenization process converges consistently regardless of the specific seed number used. The similarity in modulus values among different seed numbers provides confidence in the robustness of the homogenization approach.

The modulus values decrease with increasing porosity, which is expected as higher porosity introduces more voids within the material, reducing its overall stiffness and load-bearing capacity. This trend is consistent across all three directional moduli and for all seed numbers, highlighting the predictable impact of porosity on the mechanical properties of the material.

Despite the variations in porosity, the modulus values for each seed number remain relatively close to each other, especially at lower porosities. This stability in modulus values indicates that the homogenization process achieves reliable convergence across the tested porosity range, ensuring that the material's mechanical behavior can be accurately predicted for different porosity levels.

The study focused on the granulation phase for homogenization convergence because if convergence is achieved in this phase, it is expected that the subsequent, harder tissue stages will also exhibit convergence. The granulation phase, being the initial and less stiff stage, serves as a conservative benchmark. Successful convergence in this phase implies that the material will maintain its mechanical integrity and predictable behavior as it matures and becomes harder. The convergence study involved testing cubes of different sizes for each porosity level using three different Voronoi seed numbers. The results show that the selected cube sizes were sufficient to achieve convergence, as evidenced by the minimal differences in modulus values among the different seed numbers. This selection process ensures that the homogenized material models are representative and reliable for predicting mechanical properties.

Next, studying the standard deviation exhibited by these diagrams is crucial for gaining a clearer and more detailed understanding of the material's behavior under different porosity levels and homogenization conditions. The standard deviation provides a measure of the variability or dispersion of the Young's modulus values, highlighting the degree of consistency or variability in the material's mechanical properties. Additionally, visualizing these deviations can help in pinpointing any anomalies or outliers in the data, ensuring a more robust and reliable analysis [56].

The mean is the average of the Young's modulus values for the three different seed numbers. It is calculated using the formula:

$$\mu_x = \frac{1}{N}\sum_{i=1}^{N} E_{x_i} \tag{17}$$

where E_{x_i} represents the Young's modulus value for the i-th seed number and N is the total number of seed numbers (in this case, $N = 3$). The standard deviation measures the amount of variation or dispersion of the Young's modulus values from the mean. It is calculated using the formula:

$$\sigma_x = \sqrt{\frac{1}{N}\sum_{i=1}^{N}\left(E_{x_i} - \mu_x\right)^2} \tag{18}$$

where E_{x_i} represents the Young's modulus value for the i-th seed number, and μ_x is the mean of these values. The percentage standard deviation is then given by:

$$\text{Percentage Std Dev} = \left(\frac{\sigma_x}{\mu_x}\right) \times 100 \tag{19}$$

This analysis is conducted in the form of a Python script, in order to visualize the percentage standard deviations of the simulated homogenized materials.

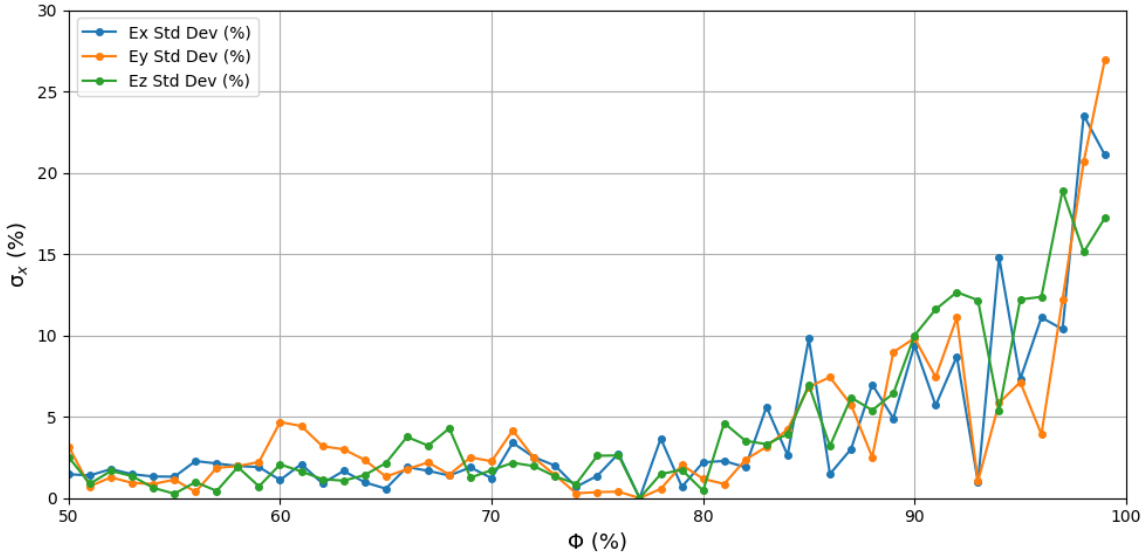

Figure 71: Relative standard deviation between varying seed number Voronoi lattices at granulation stage

At lower porosity levels (50%-80%), the standard deviation percentages for Ex, Ey, and Ez remain relatively low, indicating minimal variability in the Young's modulus values across different seed numbers. This suggests that the material's mechanical properties are consistent and predictable within this porosity range. In this range, the material structure retains sufficient integrity, with voids being relatively small and dispersed. The mechanical properties are less affected by variations in the Voronoi seed numbers, resulting in lower standard deviation percentages.

As porosity increases beyond 80%, the standard deviation percentages for all three moduli begin to rise significantly, reaching their highest values near 100% porosity. This indicates increased variability and reduced predictability of the mechanical properties at higher porosities. At higher porosity levels, the material structure becomes increasingly compromised due to larger and more numerous voids. This structural weakening amplifies the impact of different Voronoi seed configurations on the mechanical properties, leading to higher variability and standard deviation percentages.

The increased variability at higher porosities underscores the necessity for careful consideration when designing materials for use in this range. However, the observed deviations are considered acceptable given the limited computational resources. The current analysis is sufficient for its intended purpose, and further investigation would exceed the scope of this study.

The results of the aforementioned homogenized materials are summarized in the diagram below. Figure 72 displays the directional Young's modulus (E_x, E_y, E_z) representing various stages of bone tissue (indicated by color): granulation, cartilage, immature bone, and mature bone. The x-axis represents the porosity percentage, while the y-axis shows the modulus in megapascals (MPa) on a logarithmic scale.

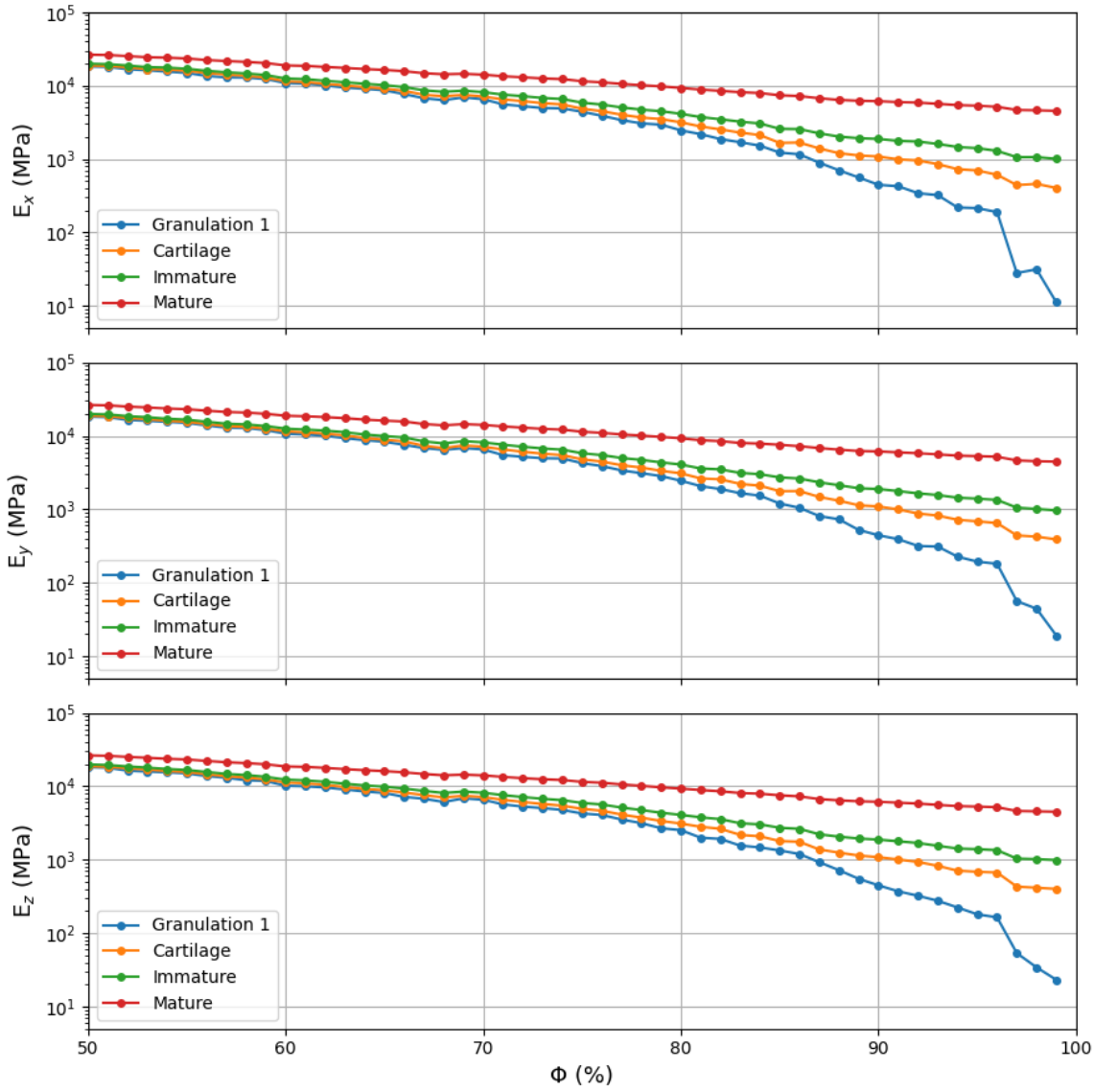

Figure 72: Directional young's moduli as a function of porosity and tissue stage

Several key observations and conclusions can be drawn from these graphs.

The values of E_x, E_y, and E_z are very similar across the porosity range, indicating that the material exhibits isotropic properties. This means that the mechanical properties of the material are uniform in all directions, which is a desirable feature for biomaterials used in bone tissue engineering as it ensures consistent mechanical performance irrespective of the loading direction.

It is worth noting that as the bone matures from granulation to mature bone, there is a clear increase in stiffness, indicated by the higher modulus values. Mature bone consistently shows the highest stiffness across all porosity levels, followed by immature bone, cartilage, and granulation tissue. This reflects the natural process of bone maturation, where the tissue becomes more mineralized and structurally sound, thereby enhancing its mechanical properties.

Mature bone exhibits more stable modulus values with less fluctuation across different porosity levels compared to granulation tissue, cartilage, and immature bone. This indicates that the mechanical properties of mature bone are less sensitive to changes in porosity. The stable convergence of modulus values in mature bone implies that even with variations in porosity, the mechanical integrity remains relatively unaffected, making it a more reliable material for load-bearing applications.

Moreover, as before, there is a noticeable deviation in the modulus values at higher porosity levels, particularly above 90%, even between the various tissue stages. This deviation becomes more pronounced as the porosity increases. The primary reason for this behavior is the weakening of the material structure due to increased voids within the lattice, which significantly reduces its load-bearing capacity and stiffness. At high porosities, the structural integrity is compromised, leading to a substantial drop in the Young's modulus. This is particularly pronounced in the granulation phase, where the surrounding material does not contribute significantly to overall stiffness.

3.3. Yield Stress of Voronoi Homogenized Materials

In this chapter, a plane fit analysis is conducted for the yield stress of a Ti-6Al-4V Voronoi lattice. Following this analysis, the chapter explores the applicability of this plane fit to Voronoi lattices composed of other materials, assessing how the initial findings translate across different material properties.

3.3.1. Analysis of Yield Stress in Ti-6Al-4V Voronoi Lattices

In order to determine the yield strength of the Voronoi lattices made of Ti-6Al-4V, the study by Chao et al. was utilized [34]. In this model, several models of Voronoi lattices with varying porosities (Φ) and seed points spacing (N) were tested. The final results are demonstrated below.

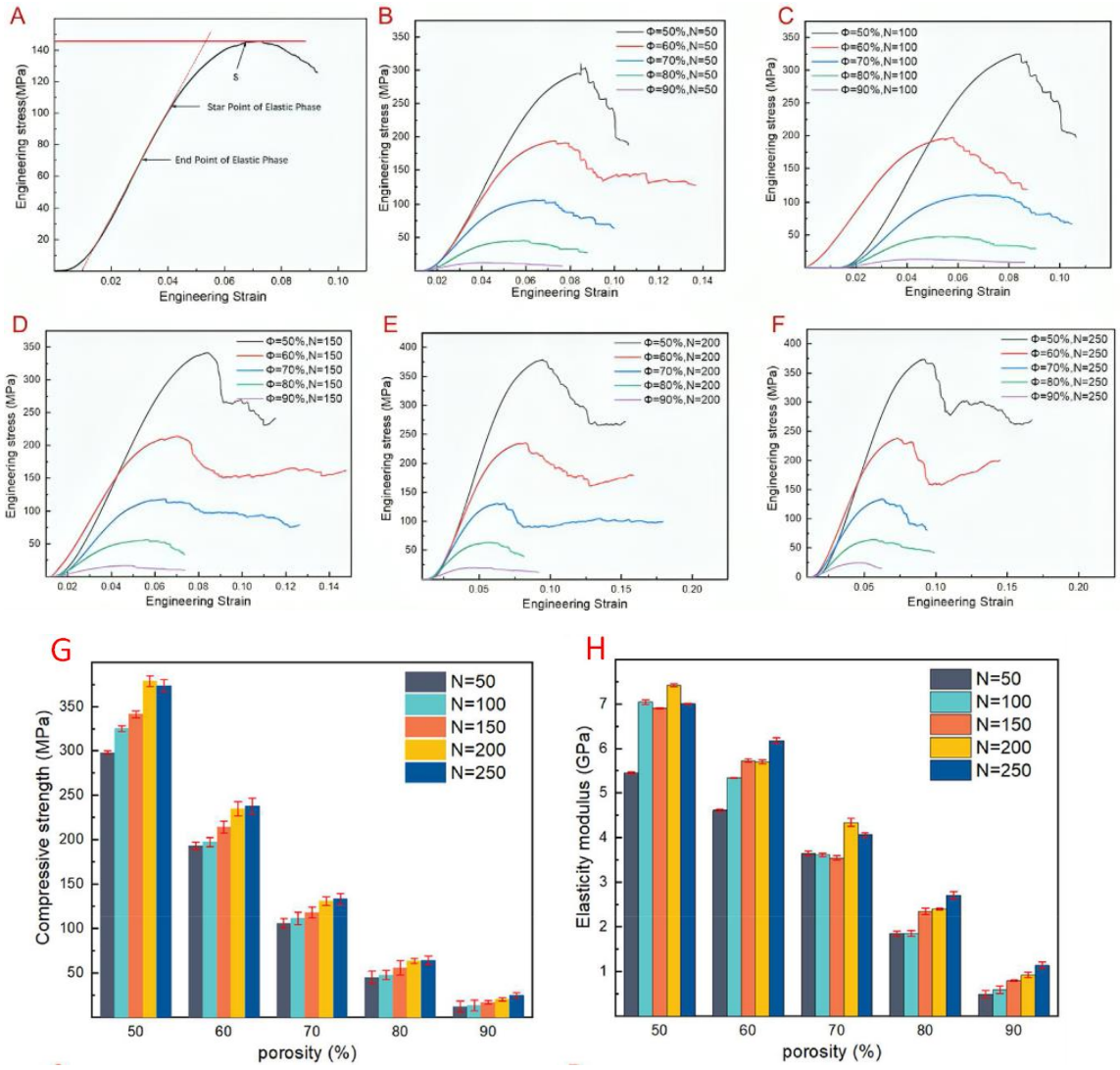

Figure 73: Compression test results at Ti-6Al-4V Voronoi lattices

It is observed that the number of seed points has a minimal impact on yield stress, whereas changes in porosity result in more significant variations. To ensure accuracy, a verification was conducted in nTopology to confirm that the referenced numbers of seed points correspond to the stated porosities for a 10x10x10 cube, which is the dimension used in the study. The results were successfully confirmed, indicating that the parameters are correctly aligned and ready for further analysis.

To further analyze the data, a MATLAB script was developed to perform a 3D plane fit based on the above results. This fit is crucial as it provides a visual and quantitative representation of how yield stress behaves across different variables such as seed points and porosity. By applying a plane fit, it is possible to identify trends and relationships within the data more clearly, offering insights into the mechanical behavior of the materials under study. This method enhances the accuracy of predictions about material performance, especially in varying manufacturing scenarios. The plane is expressed using the expression below.

$$z = 1.3325 \times 10^{3} - 28.7940x + 0.9055y + 0.1581x^{2} - 0.0090xy - 2.5714 \times 10^{-4}y^{2} \quad (20)$$

In the above equation, z expresses the yield strength, x expresses the porosity, while y is the number of seed points. The results of the 3D plane fit are presented below, showcasing a refined approach towards the complexities of material properties in Voronoi lattices.

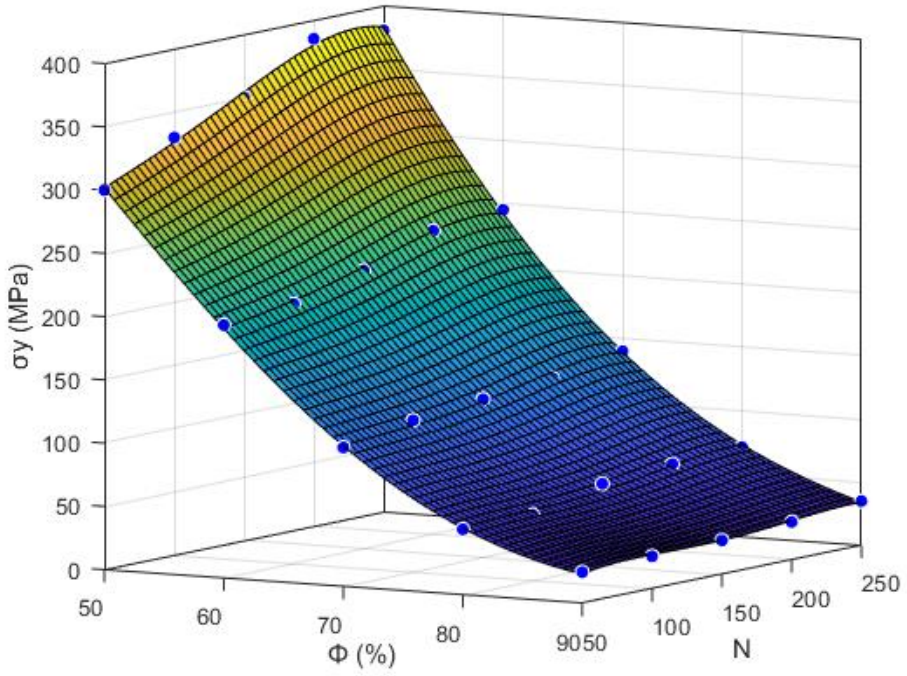

Figure 74: Plane fit of yield strength versus porosity and seed points in Voronoi lattices

3.3.2. Yield Stress Plane Fit Assessment for Different Material Voronoi Lattices

The next step involves exploring whether these findings apply to materials beyond Ti-6Al-4V. To facilitate this exploration, additional research papers were reviewed. The analysis utilizes the yield strength of Ti-6Al-4V solid to determine ratios because this material is the primary focus. However, it is crucial to acknowledge that the derived ratio is adaptable to various other materials, including PLA and Mg. This adaptability underscores that the metric, initially developed for Ti-6Al-4V, is not exclusive to this material but is instead a universal indicator applicable across different materials. This suggests that the results could be indicative of broader material properties, not just those specific to Ti-6Al-4V.

$$\frac{Yield_{Ti-6Al-4V,lattice}}{Yield_{Ti-6Al-4V}} = \frac{Yield_{PLA,lattice}}{Yield_{PLA}} = \frac{Yield_{Mg,lattice}}{Yield_{Mg}} = constant \qquad (21)$$

The first paper by Efstathiadis et al. concerns Voronoi lattices made by PLA [57]. The data indicates that the beam dimensions are $40 \cdot 40 \cdot 40$ mm. Table 14 lists the node counts used in this paper, which represent the number of seed points input directly into MATLAB. Alongside these, it summarizes the corresponding porosities. Inputting these boundary conditions allows for the calculation of the expected percentage.

Table 14: Properties of the biomimetic PLA Voronoi structures by Efstathiadis et al.

Model	$\boldsymbol{\Phi}$ (%)	$\boldsymbol{N}$	$\boldsymbol{\sigma_y}$ $(\boldsymbol{MPa})$
1	60.43 ± 0.43	60	6.26 ± 0.12
2	52.03 ± 0.47	60	8.80 ± 0.12
3	44.25 ± 0.50	60	10.84 ± 0.10
4	50.99 ± 0.28	80	9.47 ± 0.13
5	44.69 ± 0.32	100	11.55 ± 0.40
6	58.04 ± 0.85	60	7.40 ± 0.06
7	54.23 ± 0.21	60	8.57 ± 0.45

The stress-strain curves of this study for the PLA Voronoi lattices are demonstrated below.

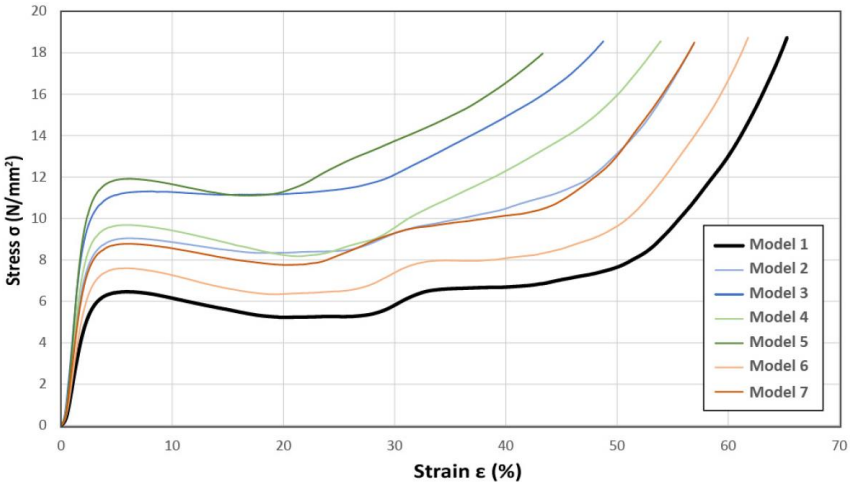

Figure 75: Stress-strain curves for the biomimetic PLA Voronoi models

For instance, in Model 1, there are 60 seed points and a porosity of 60.43%. The stress-strain diagram for this model predicts a specific percentage.

$$\frac{Yield_{lattice}}{Yield_{PLA}} = \frac{6.26}{26} = 24.1\% \quad (22)$$

Using this data, the MATLAB plane fit calculates that the yield will approximate 21% to 22.18% of the material's yield strength. This result is within a reasonable deviation range of 10%, confirming the model's accuracy. The analysis progresses with Voronoi lattices made from Mg by Yue et al., which is more complex as it does not explicitly specify the number of seed points [58]. These must be manually determined using nTopology. The properties of the material used in this study, AZ91, are summarized below.

Table 15: Material properties of AZ91

$\boldsymbol{\rho}$ $(\boldsymbol{kg/m^3})$	$\boldsymbol{E}$ $(\boldsymbol{GPa})$	$\boldsymbol{\nu}$
1810	35	0.3

The data specifies that the specimens are 30x30x30 mm and details the porosities being studied (e.g., V95 = 95% porosity, V83 = 83% porosity). It also includes the strut radius, as indicated in the table below.

Table 16: Properties and geometrical parameters of AZ91 Voronoi lattices

$\boldsymbol{\Phi}$ (%)	83	86	89	92	95
$\boldsymbol{R_{strut}}$ $\boldsymbol{(mm)}$	0.5	0.63	0.78	0.9	1

In nTopology, these geometric parameters inform the lattice design. The methodology involves entering the known thickness and adjusting the point spacing arbitrarily until the target porosity is achieved in the homogenization process. For instance, a porosity of 83% was attained in this example. After reaching the desired porosity, the number of points is noted; for this case, it was 395.

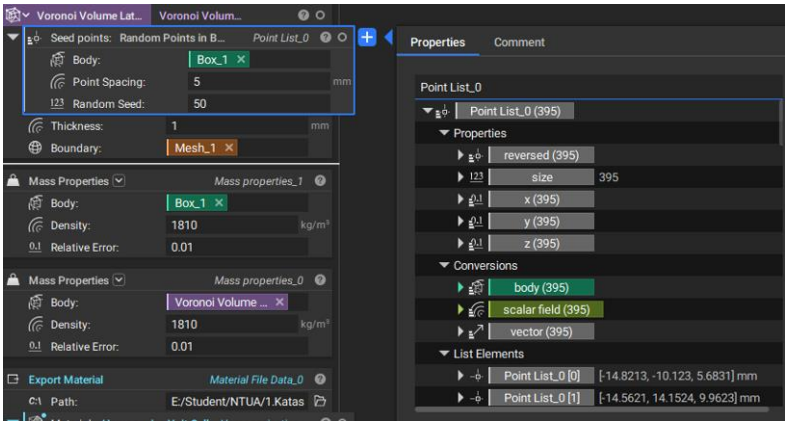

Figure 76: Number of seed points for 83% porosity according to Yue et al.

The paper provides the following diagram illustrating the various Voronoi configurations.

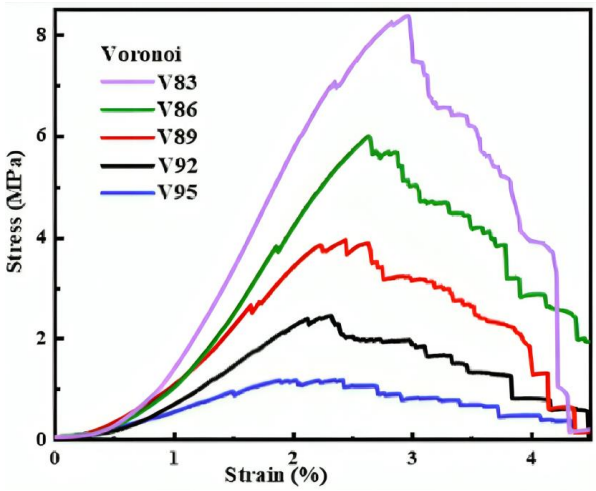

Figure 77: Experimental compressive stress-strain curves for AZ91 Voronoi lattices

With this information, parameters such as a porosity of 83% and 380 seed points are input into MATLAB. Based on the stress-strain diagram for V83, the following yield percentages are anticipated.

$$\frac{Yield_{lattice}}{Yield_{AZ91\,Mg}} = \frac{8.5}{160} = 5.3\% \tag{23}$$

Using this dataset, MATLAB calculates that the yield stress is approximately 6.2% of the material's yield strength, indicating that the model is effective for this material with a deviation around 10%. Consequently, it is reasonable to conclude that the methodology is reliable for materials with a Voronoi lattice configuration, provided that the number of seed points and porosity are known.

It is also important to note that in all calculations, the yield stress percentage was consistently overestimated by 5% due to the presence of tissue instead of air surrounding the lattice. This adjustment was derived from simulation results.

4. Computer Aided Design of Bone and Implants

This section explores the CAD modeling of the femoral bone, with a specific focus on the design elements integral to reconstructive orthopedics. It delves into the porous scaffold and its associated brackets, detailing the implementation of a retrograde intramedullary nailing system. Additionally, attention is given to the distal femur plate, examining its role and integration within the overall CAD model. This comprehensive overview aims to highlight the critical components and their functionalities within the reconstruction of the femoral anatomy.

4.1. Porous Scaffold and Brackets

This chapter addresses the design of the porous scaffold. Due to the complex nature of porous structures, creating an accurate model is impractical. Instead, a solid model representing the scaffold was designed. To ensure the model accurately reflects the mechanical properties of the porous scaffold, material homogenization was employed, assigning appropriate mechanical characteristics to the solid model.

The scaffold design utilized a 10 cm segment of the lateral femur bone to mimic the actual bone defect. Two brackets were sketched and extruded on one side of the scaffold to secure it to the bone, ensuring fit and alignment. Holes were created in the brackets for locking screws, providing a stable and secure connection essential for the implant's success.

Figure 78: Porous scaffold implant with brackets

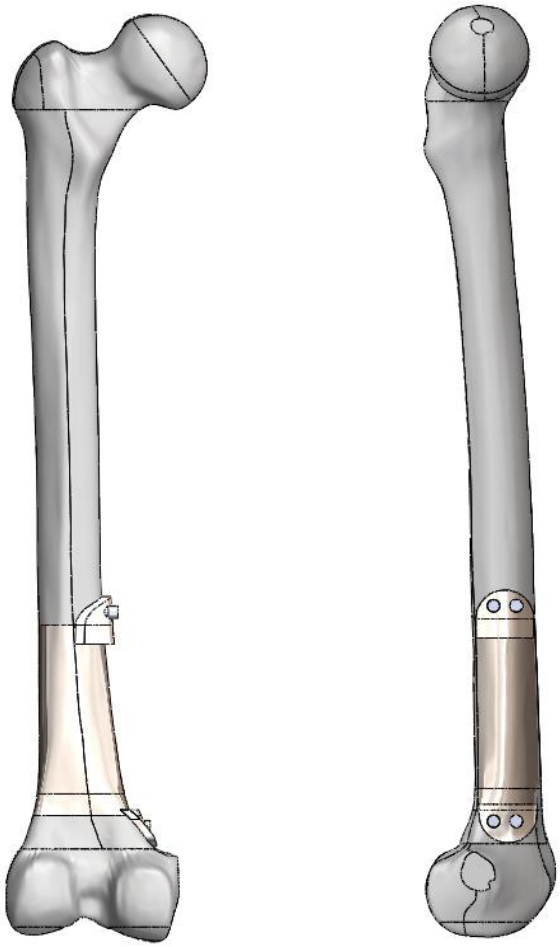

Figure 79: Femoral bone with porous scaffold implant and brackets

The scaffold is secured to the bone using brackets designed for a precise fit and alignment. In practical applications, the scaffold features a Voronoi lattice structure with increased density near the bracket attachment points. This localized density enhances mechanical stability, preventing failure and ensuring a secure fit. Mimicking natural bone density variation, it promotes better integration and load distribution. Combining the scaffold with conventional methods like intramedullary nails or plates provides additional support and stability, crucial for maintaining the scaffold's position during healing. This integration results in a more reliable solution for bone repair and regeneration, directly impacting treatment success and patient recovery.

4.2. Retrograde Intramedullary Nail

This chapter focuses on the design process of the retrograde intermedullary nailing system using Solidworks. The design was inspired by the Alpha Femur Retrograde Nailing System by Stryker. Creating the essential bends in the nail required iterative adjustments and refinements. The final design included necessary holes for locking screws, ensuring stability and promoting healing by securely attaching the nail to the bone.

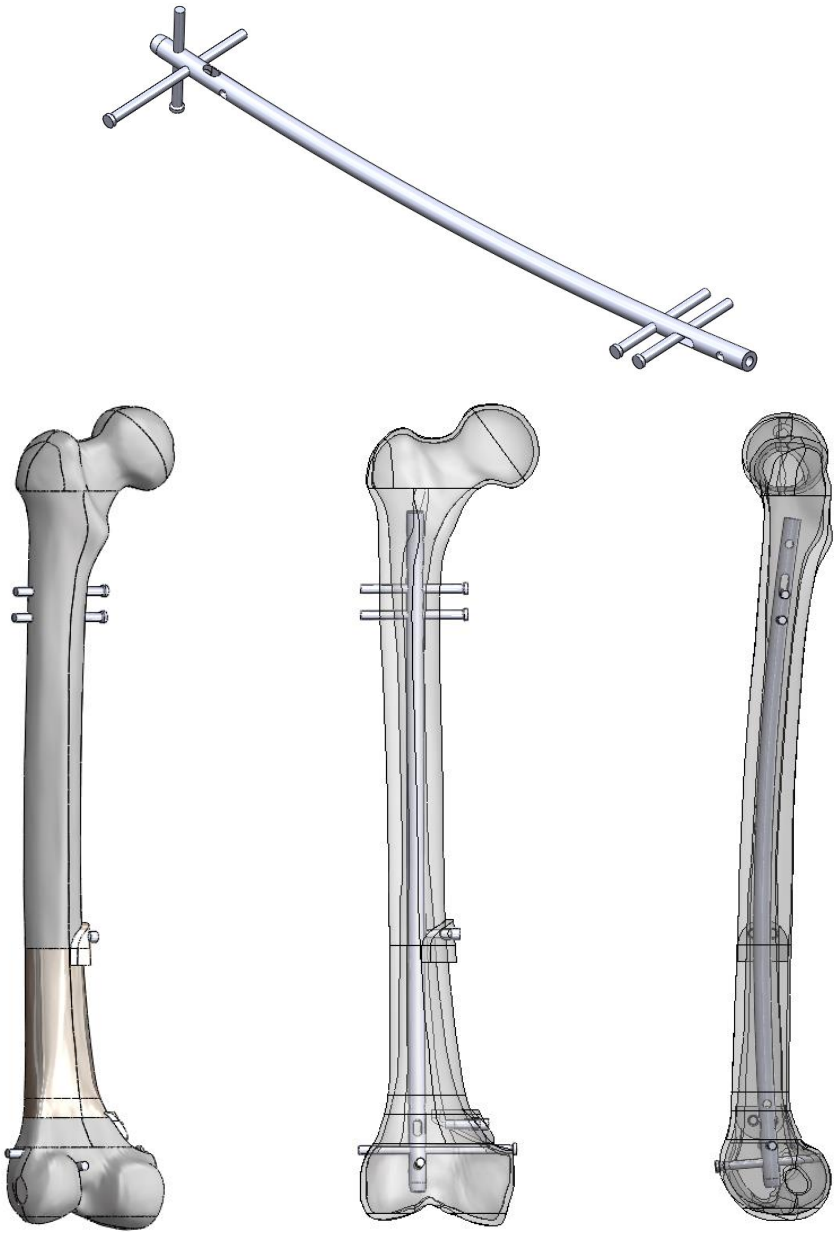

Figure 80: Femoral bone with retrograde intramedullary nail

4.3. Distal Femur Plate

The basic plate design was inspired by the AxSOS 3 Ti Distal Lateral Femur plate from Stryker. Using Solidworks, the outline of the distal plate was sketched and the plate body was created through extrusion to ensure optimal contact with the bone. Necessary holes were added to the plate, resulting in the final design of both the main and secondary plates.

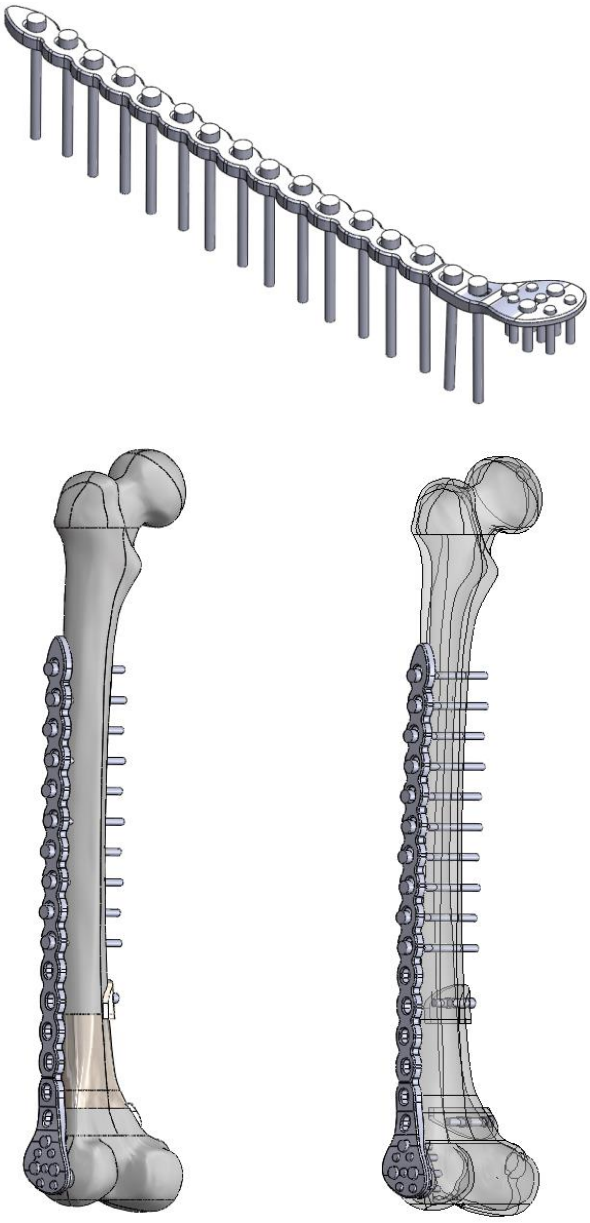

Figure 81: Femoral bone with distal femur plate

4.4. Real Case Scenario CAD

A real-case scenario from Attikon Hospital is also examined and presented, from which a CT scan has been retrieved. The corresponding CAD model shown below. This case features a fracture that is no longer uniform, thereby better reflecting a real-world scenario with a more irregular shape. Adjustments have been made for CAD and FEA purposes; however, these modifications are minor, ensuring that the models accurately represent the real case. The reinforcement method employed is a nail, with a patient weight of 80 kg. The fracture gap has a maximum length of about 14 cm.

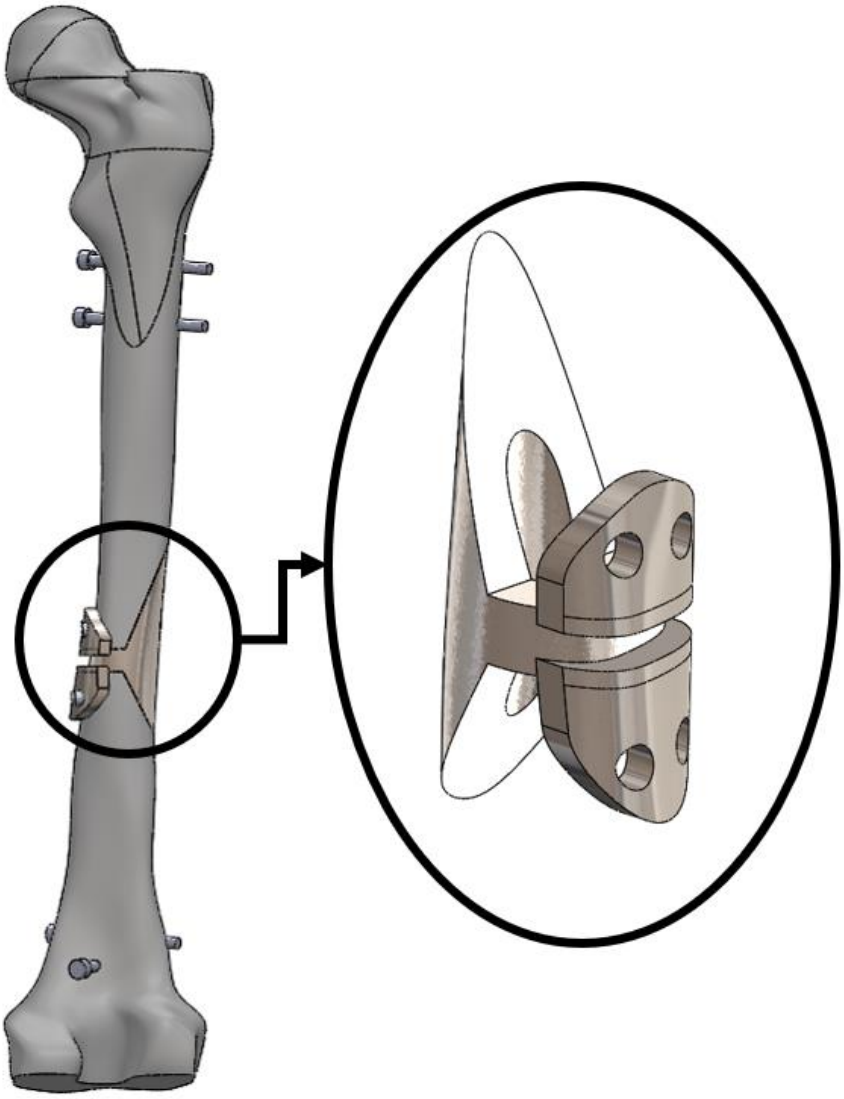

Figure 82: CAD of real case scenario and scaffold

5. Finite Element Analyses and Scaffold Optimization

In this chapter, the discussion will cover several key aspects of the study. It will begin with the model setup, including gait analysis, FEM boundary conditions, and FEM mesh. Following this, the scaffold optimization algorithm will be explored, detailing its functionality and setup, and presenting the FEA results and discussion. Lastly, the constraints and limitations of the methodology will be addressed, outlining the challenges encountered during the research.

5.1. Model Setup

5.1.1. Gait Analysis

The gait cycle is a fundamental concept in the study of human biomechanics, particularly in understanding how individuals walk and run. It includes the series of movements that a person's lower limb undergoes from the initial contact of one foot with the ground until that same foot contacts the ground again. This cycle is divided into two main phases: the stance phase and the swing phase [59], [60].

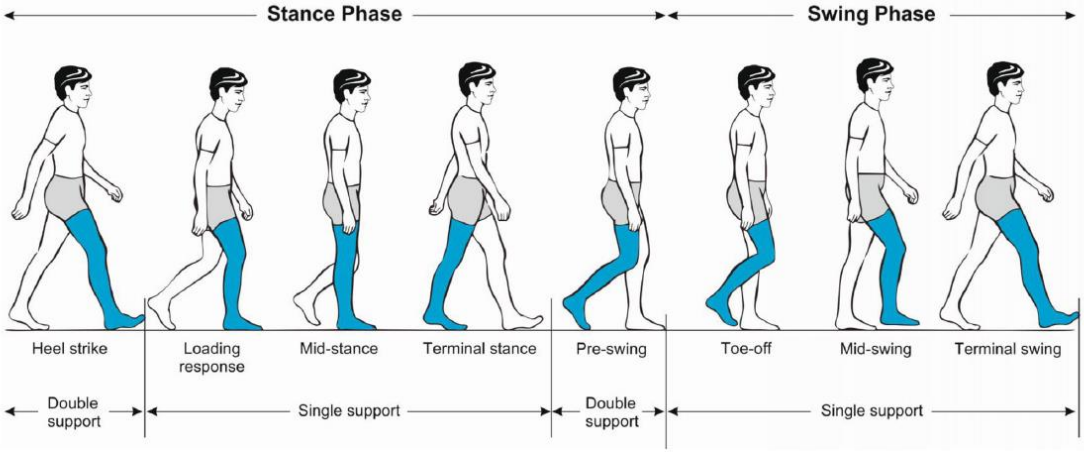

Fig. 1 Phases of the normal gait cycle

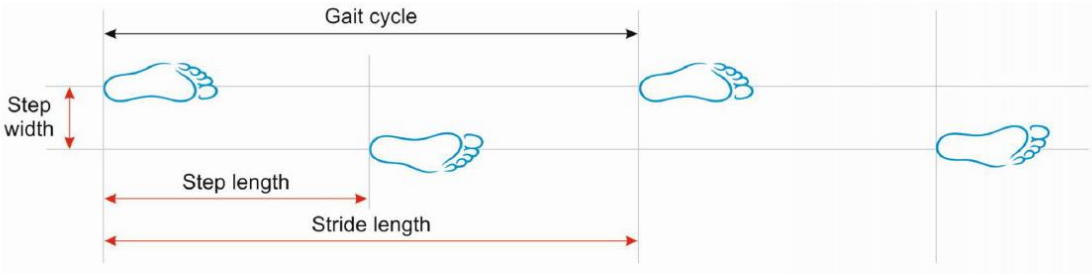

Figure 83: Basic terminology describing the gait cycle

The stance phase of the gait cycle starts with initial contact or heel strike and ends with toe-off, where the foot bears the body's weight and progresses through stages such as loading response, mid-stance, terminal stance, and pre-swing. During these stages, the body absorbs weight, stabilizes, and shifts over the supporting foot, ending as the heel lifts and the weight transitions to the opposite foot for the swing phase. The swing phase entails the foot lifting from the ground and moving through initial, mid, and terminal swing, preparing for the next contact.

A notable aspect of the gait cycle is the peak forces experienced, particularly impacting the femoral head around 16% into the cycle, with forces ranging from 238% to 404% of a person's body weight. Key muscles like the abductors, quadriceps, and iliopsoas are crucial in this phase, exerting forces between 104% and 158% for abductors, 58% to 95% for quadriceps, and 20% to 32% for iliopsoas, significantly affecting force distribution on the femur. This is essential for finite element analysis because it enables precise modeling of the forces exerted on the femur during various walking stages.

The proximal femur connects to the pelvis acetabulum through a ball-in-socket joint, enabling rotation across all cardinal planes: sagittal, transverse, and frontal. This joint is also the most mobile in the body. Movements of the lower limb include flexion and extension in the sagittal plane, rotation in the transverse plane, and abduction and adduction in the frontal plane [60].

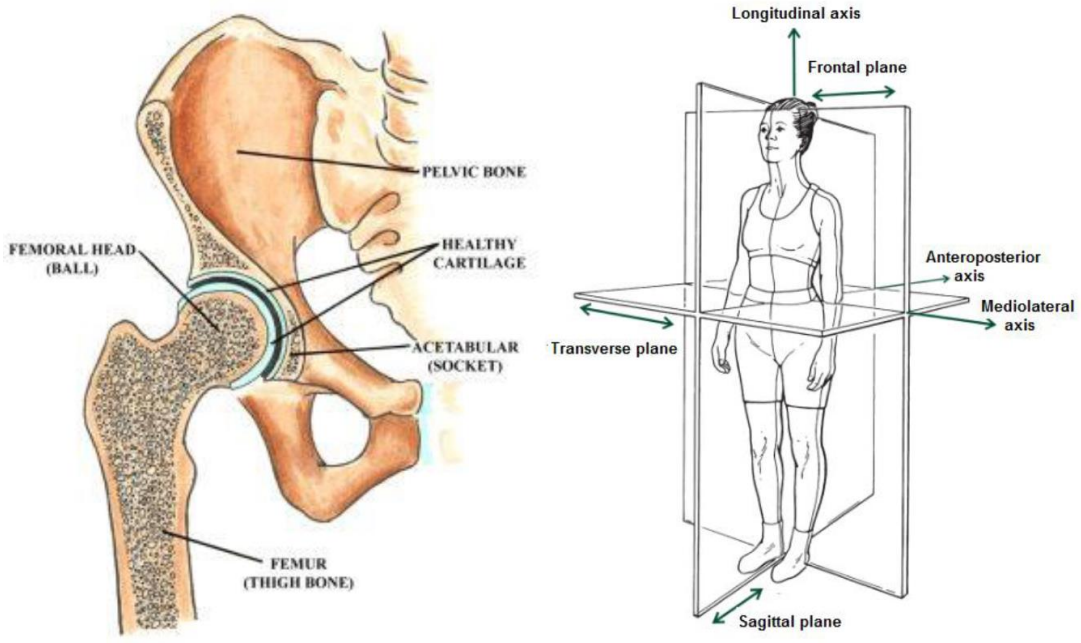

Figure 84: The hip joint is a ball-in-socket and allows movement in the transverse, sagittal and frontal

Surrounding the femur are several important muscle groups, including the quadriceps, hamstrings, and adductors. These muscles are responsible for generating forces that act upon the femur during various activities such as walking, running, and jumping. These forces are essential for movement and help maintain stability and posture by dynamically interacting with the femur and other skeletal structures [61].

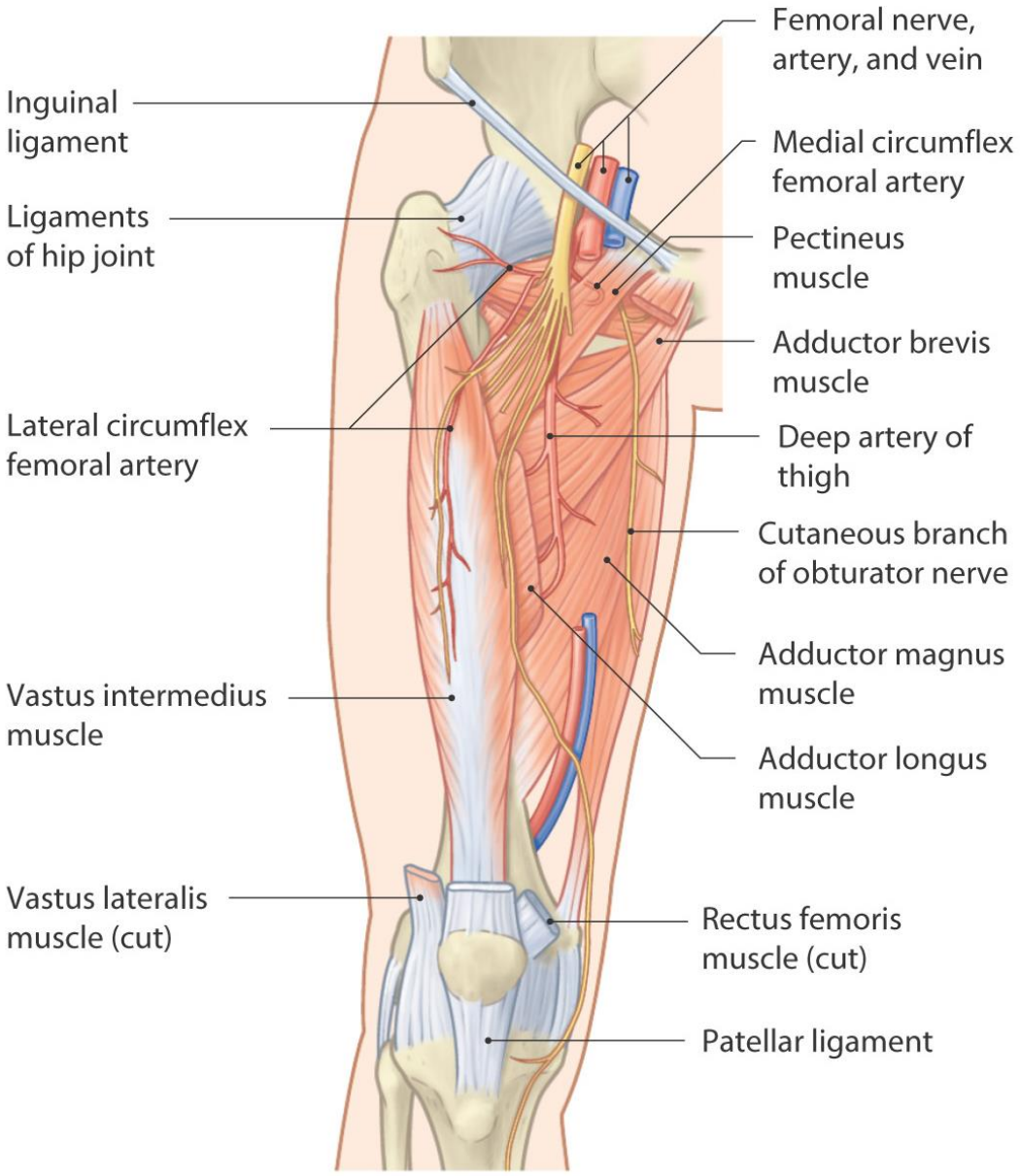

Figure 85: Muscles of the thigh - anterior view

5.1.2. FEM Boundary Conditions

In finite element analysis (FEA), the muscular and weight-induced forces on the femur can be effectively modeled as boundary condition forces. This modeling allows for a detailed analysis of how the femur responds to different types of physical stresses and strains under various conditions. Additionally, fixed support boundary conditions can be applied in the FEA models to simulate the constraints that the body imposes on the femur, such as where it articulates with other bones at the hip and knee joints. These boundary conditions help in predicting how the femur reacts to activities [62].

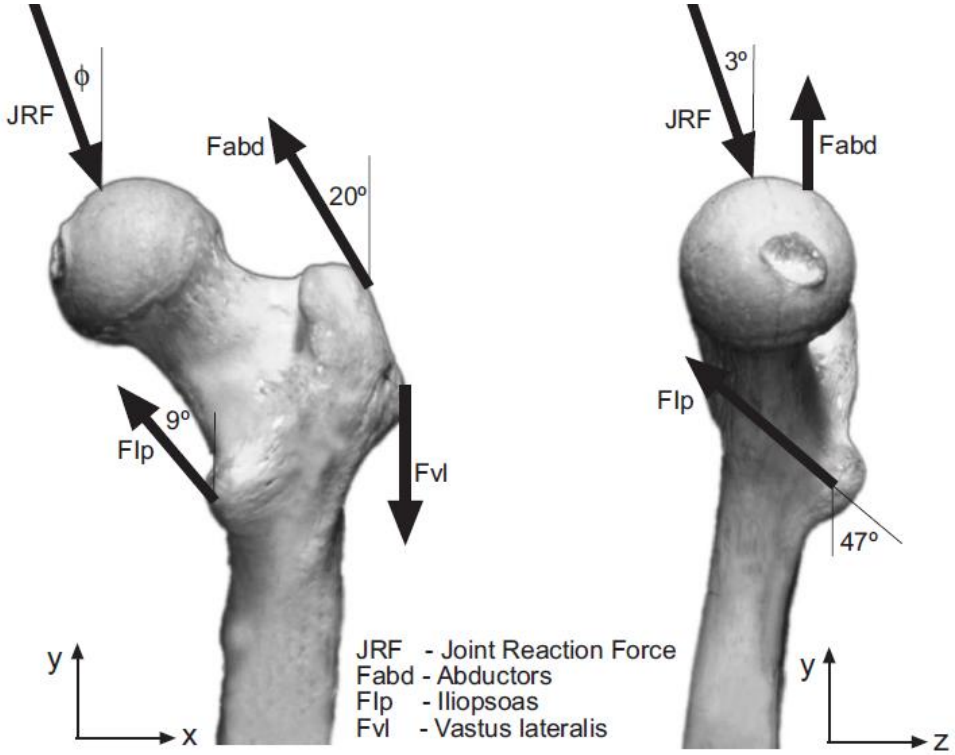

Figure 86: The applied joint reaction and muscle forces

Table 17: Components of the forces acting on the femur

Force	Total (N)	X-Component (N)	Y-Component (N)	Z-Component (N)
Hip Joint	1751	-367	141	1706
Abductors	765	262	0	-719
Quadriceps	427	0	0	427
Iliopsoas	147	15	-106	-100

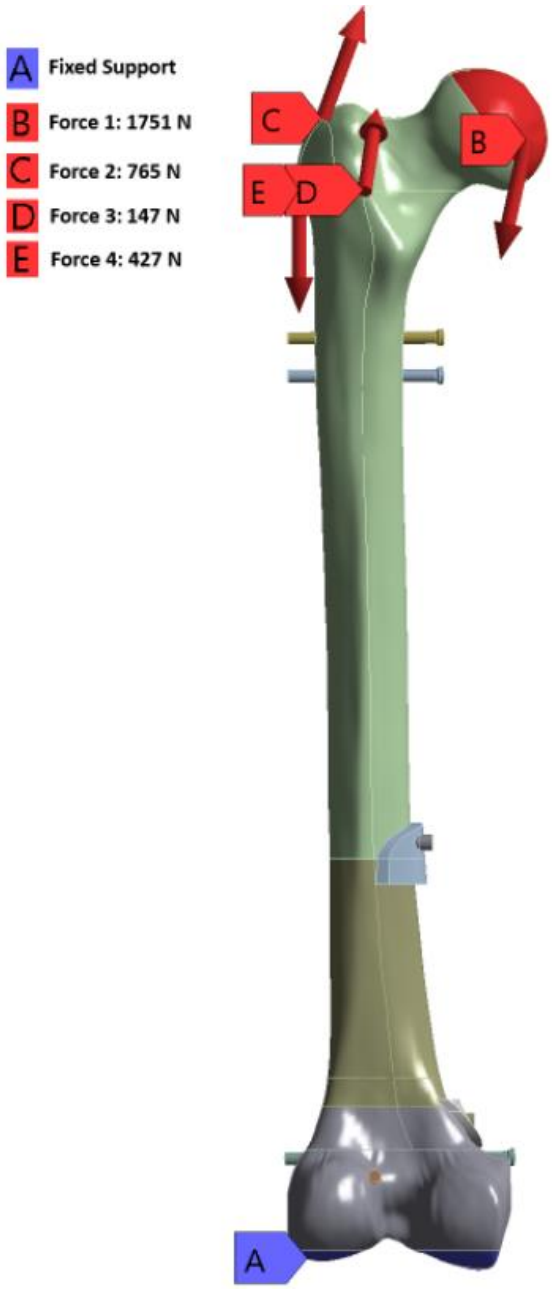

Figure 87: FEM Boundary Conditions for the 80kg benchmark weight

For varying weights, the forces and their components were adjusted by multiplying them by a factor corresponding to the ratio of the new weight to the original weight.

$$F_{new} = \frac{W_{new}}{W_{benchmark}} \cdot F_{benchmark} \tag{22}$$

5.1.3. FEM Mesh and Contacts

The quality of the mesh is crucial because it directly influences the accuracy, efficiency, and reliability of the simulation results. A well-refined mesh ensures that the geometry of the model is precisely represented, particularly around complex shapes or areas of high stress gradients, where small changes in the geometry can significantly affect the outcome of the analysis. Higher mesh quality allows for better approximation of the stress and strain distribution within the material, enabling more accurate predictions of how the structure will behave under various loads.

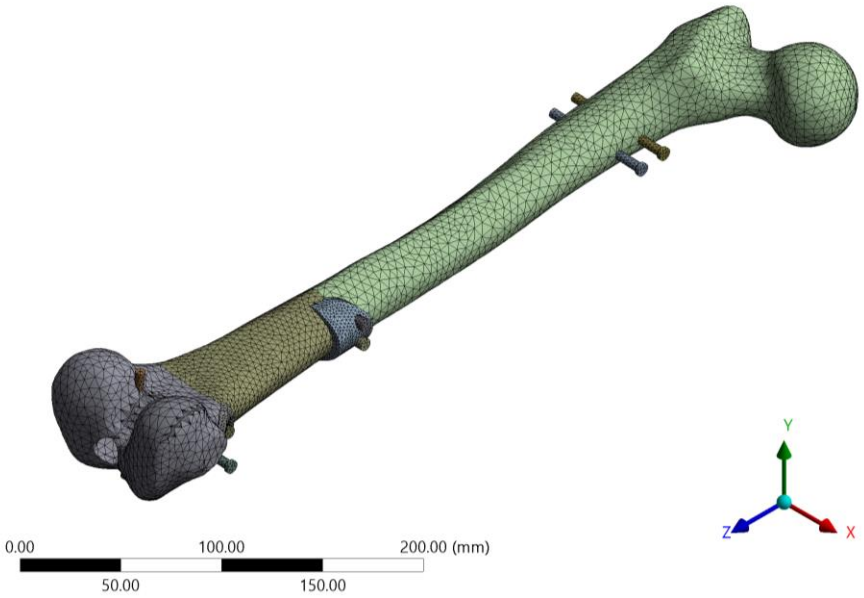

Figure 88: Femur FEM mesh

Table 18 indicates the specific values of the elements used.

Table 18: Mesh size and conforming method per model part

Model Part	Conforming Method	Mesh size (mm)
Implants	Tetrahedrons	2
Scaffold		3.5
Bone		5

It should be noted that all contact interfaces were treated as bonded, with the exception of the interface between the bone/scaffold and the nail or plate, depending on whether the configuration included a nail or a plate, respectively.

5.2. Scaffold Optimization Algorithm

5.2.1. Setup and Hyperparameters

The porosities in this model are treated as material inputs, directly imported from nTopology into the ANSYS engineering data framework. Each porosity configuration is assigned a descriptive name to facilitate easy handling and manipulation within the Python code environment. In the library of materials, a specific coding convention is used to facilitate easier handling within the code: <porosity>_#. In this naming scheme, <porosity> refers to the specific porosity configuration and # is tissue stage.

Table 19: Tissue stage naming scheme

#	Meaning
1	Granulation
2	Cartilage
3	Immature
4	Mature

The hyperparameters of the Python code developed for this project play a crucial role in defining the behavior and outcomes of the scaffold simulation.

- **Strain boundaries**: based on studies such as those by Lacroix and Isaksson, set the limits for acceptable strain within the scaffold regions, ensuring the structural integrity is maintained [45], [46].
- **Split of scaffold regions:** The way scaffold regions are split is another key hyperparameter; regions can be divided based on strain results to ensure uniform distribution, but they can also be split based on volume or the radius of the scaffold to suit different modeling needs.
- **Relaxation functions:** These are employed to manage and reduce stress within these regions, aiding in the realistic simulation of tissue behavior under various conditions.
- **Initialization parameters:** They set the starting conditions for the simulation, providing a baseline from which the model can evolve.
- **Oscillation threshold:** A critical hyperparameter that prevents infinite loops in the code by limiting the number of times porosity can oscillate before adjustments are made, ensuring the simulation progresses efficiently.

- **State matrix:** A vital hyperparameter of the Python code, serving as a comprehensive data structure that manages and tracks the current state of scaffold regions throughout the simulation process.

The state matrix was deemed necessary to ensure organized storage and efficient handling of multiple parameters involved in the simulation, such as porosity, tissue stages, and stress-strain data. By centralizing this information, the state matrix enables the code to make informed decisions about tissue promotion, porosity adjustments, and other critical actions, ensuring the simulation progresses smoothly and accurately. The columns of the state matrix correspond to the number of regions, which are determined by the fracture gap of the bone. The rows of the state matrix are detailed below, each serving a specific function in the simulation process.

- **Row 0: Region Names**
  - Purpose: Stores the names of scaffold regions.
  - Functionality: Helps identify and reference specific regions throughout the simulation.
  - Importance: Essential for tracking which region each data point corresponds to, ensuring accurate updates and operations.
- **Row 1: Tissue Stages**
  - Purpose: Keeps track of the current tissue stage for each region.
  - Functionality: Updated as regions progress through different stages.
  - Importance: Critical for determining promotion eligibility and managing the progression of tissue maturation.
- **Row 2: Porosity Indices**
  - Purpose: Stores the current porosity value for each region.
  - Functionality: Updated based on the patient's weight and other dynamic factors during the simulation.
  - Importance: Essential for assessing mechanical properties and making decisions about porosity adjustments.
- **Row 3: Promotion Eligibility**
  - Purpose: Indicates whether a region is eligible for promotion to the next tissue stage.
  - Functionality: Set to specific values based on the results of stress and strain evaluations.
  - Importance: Helps the code efficiently manage and prioritize regions that need to be upgraded.
- **Row 4: Initial Strain Values**
  - Purpose: Stores initial strain values for each region.

  - Functionality: Used for evaluating stress-strain behavior and adjustments.
  - Importance: Important for ensuring that strain values are within acceptable limits and for detecting any necessary changes.
- **Row 7: Current Boundaries**
  - Purpose: Holds the current boundaries for each tissue stage.
  - Functionality: Updated as the simulation progresses to reflect new thresholds for different tissue stages.
  - Importance: Ensures that the boundaries for promotion and other decisions are accurately maintained.
- **Row 8: Cumulative Relaxation Factor**
  - Purpose: Stores the cumulative relaxation factor for stress management.
  - Functionality: Incremented when needed to alleviate stress in the scaffold.
  - Importance: Crucial for managing mechanical stress and preventing damage to the scaffold regions.
- **Row 9: Last Porosity**
  - Purpose: Records the most recent porosity value for each region.
  - Functionality: Used to track changes in porosity over time.
  - Importance: Helps in detecting trends and potential issues related to porosity adjustments.
- **Row 10: Second Last Porosity**
  - Purpose: Stores the second most recent porosity value for each region.
  - Functionality: Provides a historical record of simulations.
  - Importance: Useful for comparing changes and understanding the impact of adjustments over time.
- **Row 11: Porosity Occurrence Count**
  - Purpose: Counts the occurrences of each porosity value for each region.
  - Functionality: Updated whenever a new porosity value is assigned.
  - Importance: Essential for detecting oscillations and ensuring the simulation does not get stuck in repetitive loops.
- **Row 12: Yield Stress Values**
  - Purpose: Stores yield stress values for each region based on their current porosity.
  - Functionality: Updated using yield stress corresponding to porosity.
  - Importance: Critical for evaluating mechanical performance and making necessary adjustments.

5.2.2. Algorithm Functionality

The primary process loop of the Python code for this project initializes scaffold regions with specific granulation and porosity settings. The code evaluates each region's eligibility for tissue promotion or porosity adjustment based on predefined criteria. This iterative process ensures consistent development of scaffold regions towards their target states, reflecting the logical structure and decision-making mechanisms of the code.

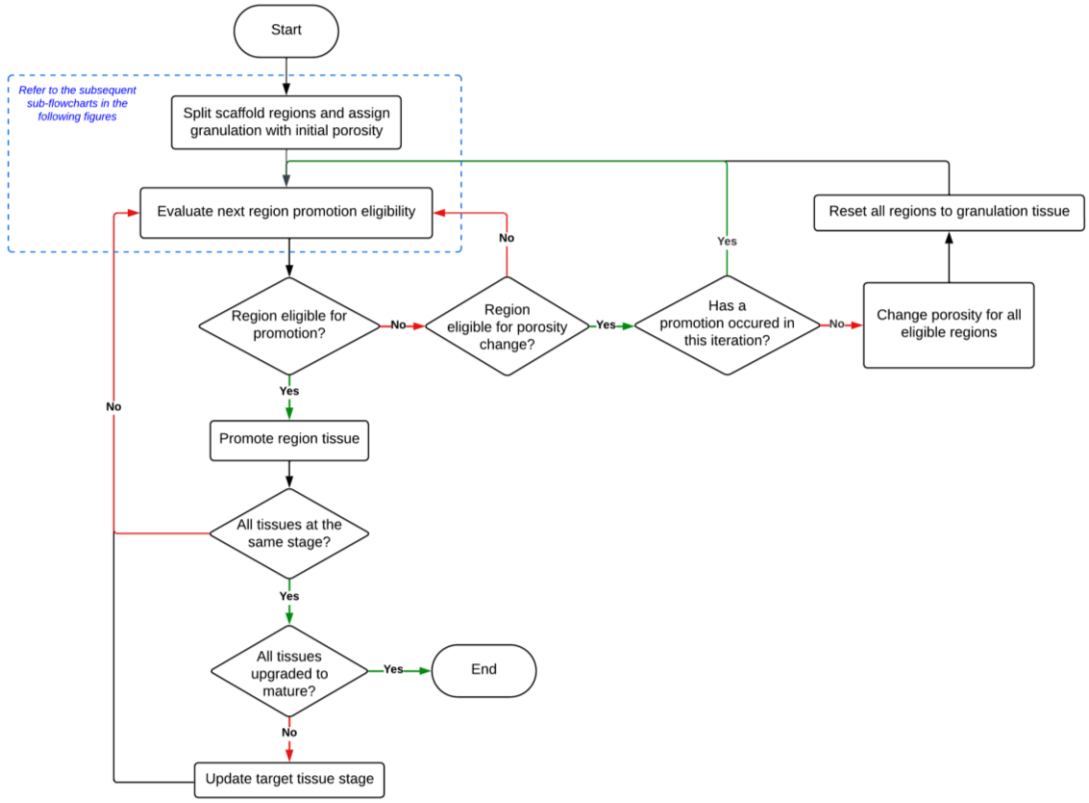

Figure 89: Flowchart for algorithm main process loop

The process continues by assessing the fracture length and allowing the user to define regional restrictions based on X and Z coordinates. The scaffold mesh elements are then split into regions according to these coordinates. The code checks for the presence of a bracket in each region, flagging those with a bracket for stress relaxation. If no bracket is present, the user is prompted to define the patient's weight, which is then used to initialize he region's porosity.

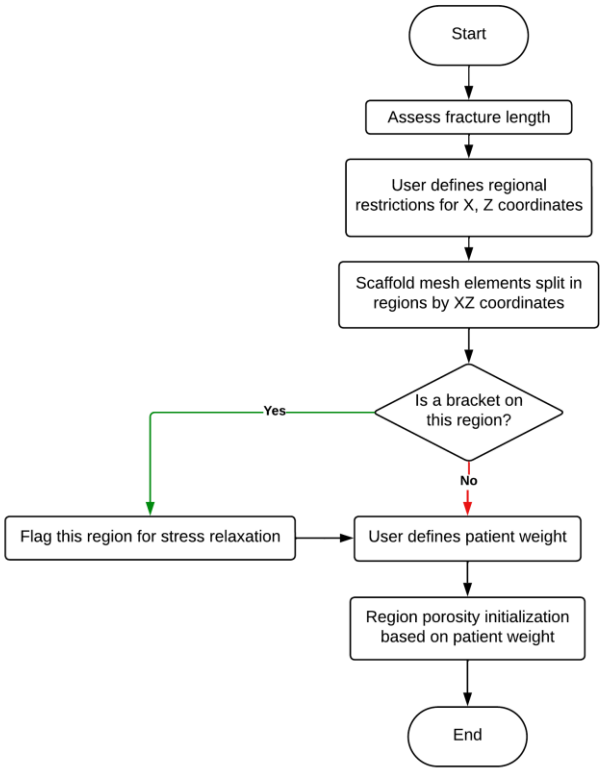

Figure 90: Flowchart for region split and porosity initialization

Regions near the brackets are flagged for stress relaxation due to increased lattice porosity density needed for bracket attachment, which results in higher yield stress. This aspect couldn't be accurately modeled in the finite element method (FEM) because it required specific element treatment that exceeded available computational resources. Therefore, stress relaxation was empirically considered and determined as shown below.

$$\sigma_{relaxation} = \frac{\sigma_{bracket}}{\sigma_{vicinity}} \cong 0.55 \tag{23}$$

The Python code assesses the porosity of each region and determines actions based on predefined thresholds. It checks if the porosity has exceeded the oscillation threshold, applying relaxation if necessary. The code then evaluates if the region is a middle region and examines vertical neighboring regions for possible upgrades. Stress-strain results are reviewed to ensure stress and strain are within acceptable limits. Based on these evaluations, the code adjusts the region's porosity or flags it for an upgrade.

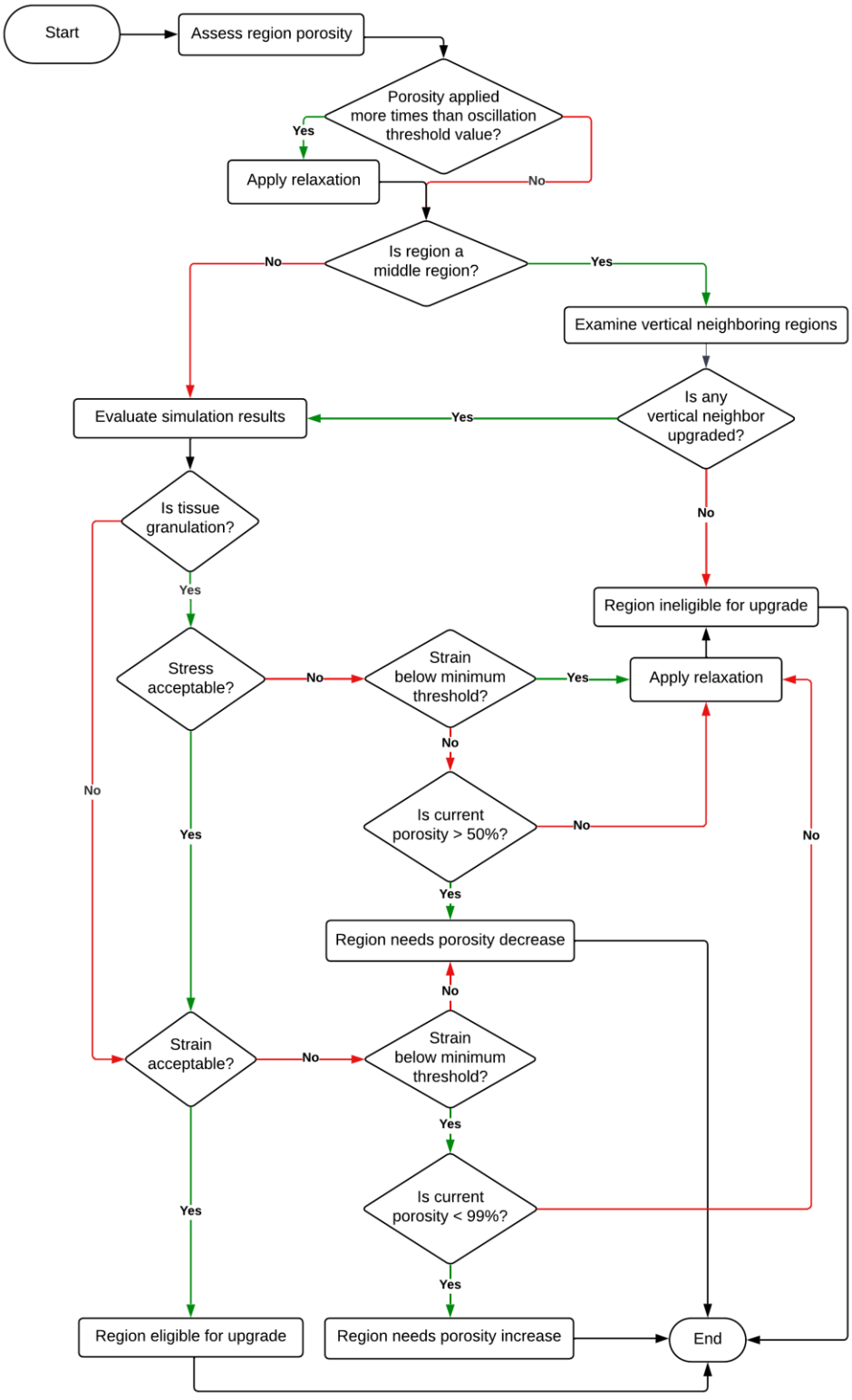

Figure 91: Flowchart for assessing region eligibility for promotion and porosity change

5.3. Optimization Results and Discussion

5.3.1. Properties and Variable Parameters in Parametric Runs

This subchapter delves into the various parameters and properties altered during the parametric runs of the simulation. The discussion will encompass the rationale behind selecting specific parameters, the range of values tested, and the impact of these changes on the overall effectiveness and efficiency of the scaffold design.

Table 20: Benchmark conditions and variable parameters in parametric runs

Parametric Run	Patient Weight (kg)	Fracture Gap (mm)	Conventional Method
Benchmark Conditions	80	100	Nail
Patient Weight	$50 - 150$	100	Nail
Fracture Gap	80	$40 - 240$	Nail
Reinforcement Methods	80	100	Plate, Nail with Plate
Real Case Scenario	80	$\cong 140$	Nail

Studying the parameters listed in the table is crucial for understanding the performance and optimization of 3D printed scaffolds under various conditions. The benchmark run serves as a control, providing a standard against which other parametric runs can be compared. The parametric weight runs explore the effects of different patient weights on scaffold performance, which is essential for personalized medicine as patient weight can significantly influence the mechanical stability and biological response of the scaffold. The parametric gap runs assess how varying fracture gaps impact scaffold efficacy, a critical factor since bone defects can vary widely in size and shape. The parametric reinforcement method runs compare different conventional methods, such as nails and plates, to identify the most effective technique for scaffold integration. By systematically varying these parameters, the study aims to optimize scaffold design and improve outcomes in bone regeneration therapies. Finally, the real case scenario run addresses the complexity of real-world bone fractures, which often do not present as uniform gaps, thus providing insights into the performance of scaffolds in more realistic scenarios.

5.3.2. Detailed Optimization Results of Benchmark Conditions

In this chapter, the focus will be on presenting the detailed results, stiffness map and contours of benchmark conditions for the scaffold after running the optimization. The porosity distribution per scaffold region for these particular conditions are presented below.

The following image showcases the final scaffold under the benchmark conditions. The image reveals that different regions of the scaffold have varying porosities, a crucial feature for adapting to localized mechanical and biological requirements. However, these variations are subtle and not easily discernible to the naked eye due to their small differences. This highlights the importance of precision in the design and optimization process to achieve the desired structural and functional properties.

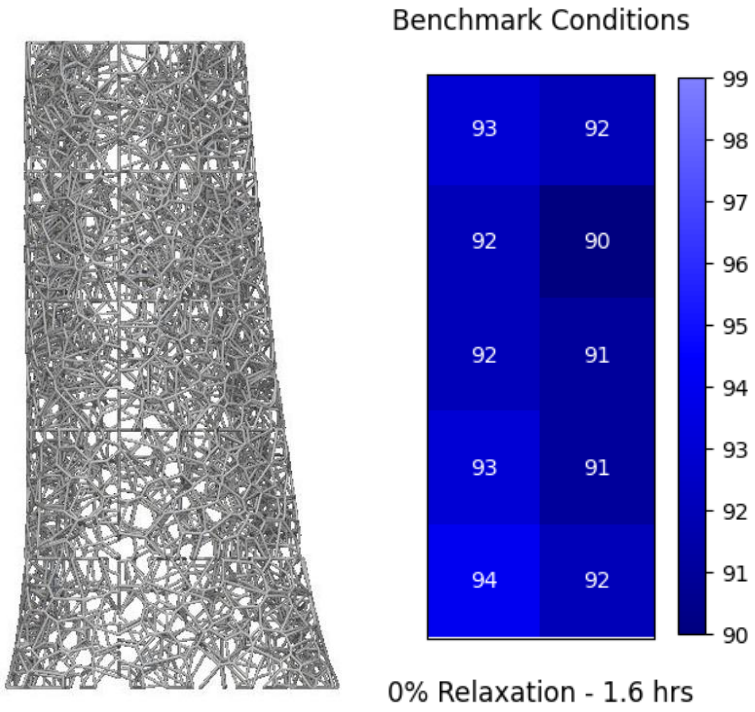

Figure 92: Stiffness map of benchmark conditions

The graphical representations and contour maps illustrating stress distributions and strain profiles across the scaffold are featured below, based on the aforementioned porosities.

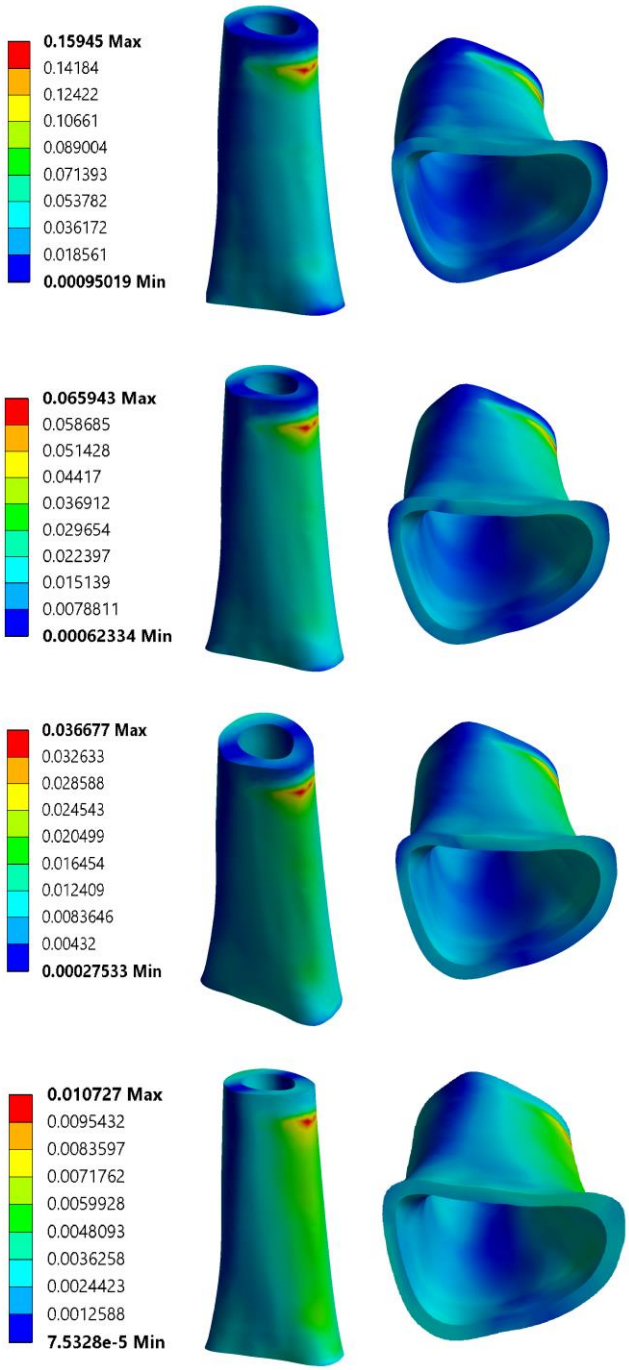

Figure 93: Scaffold strain contours - benchmark conditions (granulation-cartilage-immature-mature from top to bottom)

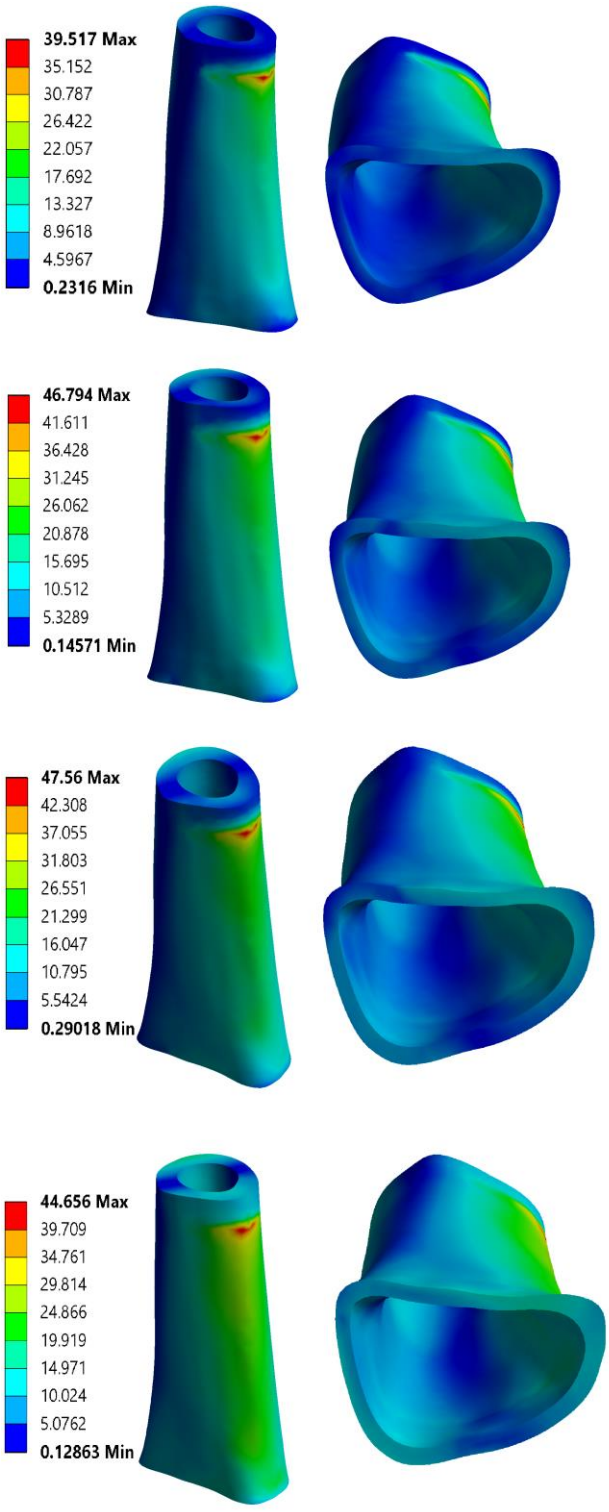

Figure 94: Scaffold stress contours - benchmark conditions (granulation-cartilage-immature-mature from top to bottom)

In the granulation stage, strains are the highest, with the highest strain regions located near the top. The stress distribution follows a similar pattern, concentrating stress near the same regions. This stage exhibits higher strain and stress concentrations because granulation tissue is soft and less capable of distributing loads efficiently. Visible larger deformations in the contour maps indicate the scaffold's high flexibility and inability to uniformly distribute stress. The stresses in this stage are relatively low because the reinforcement method (here, the nail), the brackets, and the implants absorb more of the stress. The soft granulation tissue deforms easily and does not bear much stress, as the more rigid titanium implants provide the primary load-bearing support.

During the cartilage stage, strains are lower, reflecting the stiffer nature of the tissue compared to granulation. The maximum stress increases, indicating that the scaffold is beginning to handle higher loads. The distributions are still concentrated at similar regions as in the granulation stage but are less pronounced due to the increased stiffness of the cartilage tissue. The contours show less visible deformation, indicating better load distribution and less overall deformation. The stress values remain similar in magnitude to those in the granulation stage, but the local maximum stress is higher. Additionally, as the tissue becomes more rigid, stress distribution improves, showing that the implants are bearing less load.

In the immature bone stage, strains are lower. The scaffold's ability to distribute loads improves as the tissue matures, leading to more evenly distributed stress and strain concentrations. This stage marks a transition toward a more stable and load-bearing structure. The deformations continue to decrease, showcasing a more rigid structure between the lattice's gaps, resulting in a more uniform distribution. The stress values are consistent with previous stages, with the local maximum being higher. The relationship between increased tissue stiffness and stress distribution is evident as the tissue matures.

Finally, in the mature bone stage, strains are the lowest. The local maximum stress is lower, due to the more rigid nature of the tissue. This happens because the mature bone is the stiffest and most capable of distributing mechanical loads effectively. This stage represents the optimal load-bearing condition of the scaffold, with the material properties of mature bone providing the best mechanical support. The deformation is minimal, indicating the highest rigidity and uniform stress distribution.

It is crucial to understand that the stresses in higher tissue stages are not inherently larger; rather, the local maximum stress is higher (except in the mature stage), and the

varying color bars can create a misperception. The magnitude of stresses remains similar across the stiffer tissues due to their distribution towards the implants.

The implemented stress relaxation near the brackets was designed to account for the higher density and yield strength that would be present in real-life conditions. In practice, the brackets would be denser and more capable of withstanding greater stresses, but modeling this accurately would require a finite element analysis at an extremely detailed level, which was not feasible due to computational constraints. Instead, the stress relaxation was applied through the code to simulate this effect. This was done by examining the stresses in the vicinity of the local maximum stress points and normalizing this region by a factor of 0.55 as shown below.

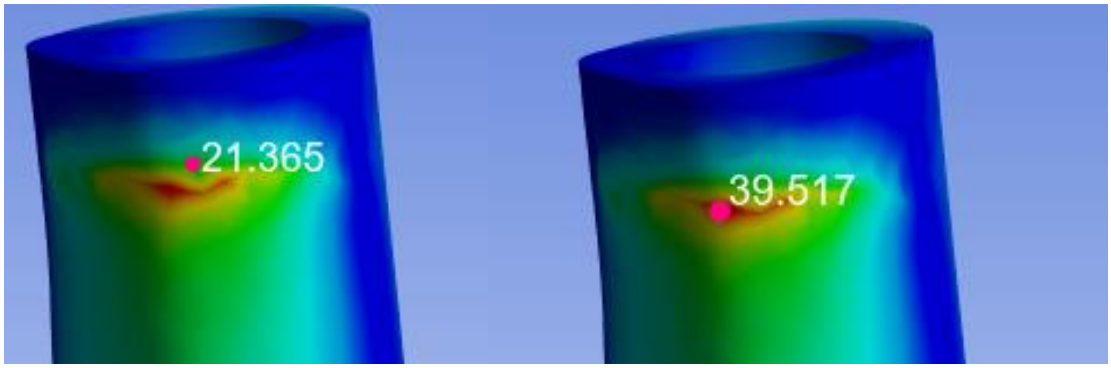

Figure 95: Stress contours near brackets at granulation stage

This normalization aims to mimic the higher yield strength and ensure that the stress distribution reflects the increased support provided by the denser brackets, thereby maintaining the structural integrity of the scaffold under realistic conditions.

5.3.3. Summarized Parametric Weights Optimization Results

In this subchapter, the results of the parametric optimization study are presented and analyzed, with a particular focus on the impact of patient weight on the titanium scaffold implant design. The subsequent sections will delve into various diagrams and datasets, illustrating the relationship between patient weight, fracture gap and methods, as functions of key parameters, such as porosity, relaxation factor, and simulation run time.

This examination begins with the parametric runs concerning patient weight. To ensure the successful operation of these parametric runs, it was necessary to adjust the boundary condition forces applied to the femur, using a factor previously analyzed in earlier sections.

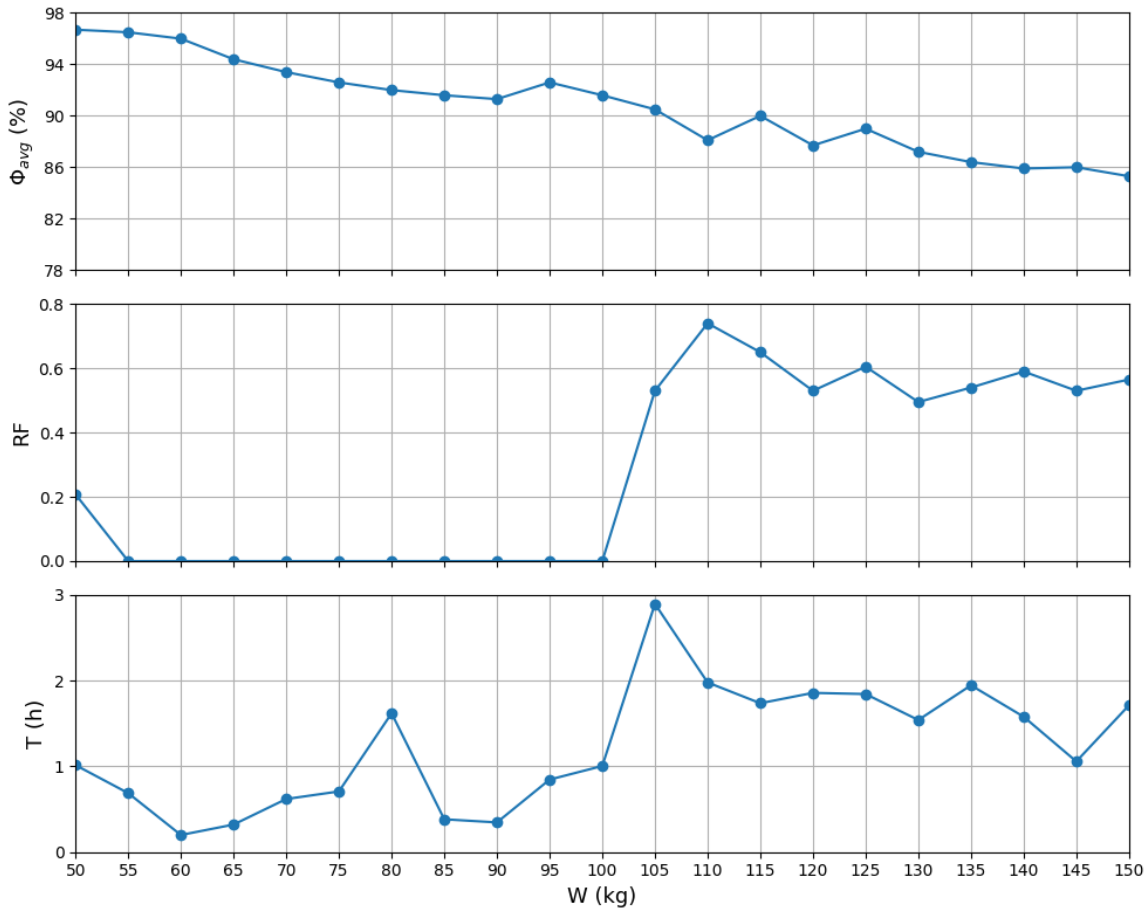

Figure 96: Parametric patient weight results

The chart is divided into three subplots, each illustrating different parameters: average porosity (%), relaxation factor, and run time (h) as the weight of the patient (kg) varies from 50 kg to 150 kg. In further tissue stages (from cartilage to mature bone), yield stresses are not checked, as acceptability at the granulation stage ensures adequacy in later stages.

The first subplot shows that as patient weight increases, average scaffold porosity decreases from about 96% at 50 kg to around 84% at 150 kg. This indicates that heavier patients require scaffolds with lower porosity for sufficient mechanical strength and stability. At 50 kg, relaxation occurs because ideal strain did not exist for all regions. The algorithm initially set the porosity at 97%, but strains were too large; adjusting to 96%, the strains became too small, leading to relaxation as the algorithm detected oscillation. At higher weights, the scaffold couldn't withstand the stresses, necessitating lower porosity, which still did not meet required strains, thus requiring relaxation.

The spikes and noise in the first subplot arise from the non-linear relationship between modulus of elasticity (E) and porosity, with significant deviations due to possible homogenization inaccuracies at high porosities (90%+). Additionally, the order by which regions are upgraded varies by weight, introducing randomness and disconnection. Approximations for weights and force components also contribute to errors, and the relaxation method introduces uncertainty depending on iterations. Another factor that might sometimes affect the results is the hyper-parameter for stress relaxation in the regions with brackets. This has been universally set at 0.55 as parameterizing it was computationally intensive. However, this introduces uncertainty for the upper right region and the exact optimal porosity at which it converges.

The second subplot shows the relaxation factor, which is zero at lower weights but increases significantly after 100 kg, peaking around 0.74 at 110 kg, and fluctuating at higher weights. This rise corresponds to higher stresses at greater weights, requiring more aggressive relaxation to maintain feasible solutions.

The third subplot indicates the optimization algorithm's run time, remaining low and stable up to 90 kg, then increasing and peaking at about 2.9 hours for 105 kg. This reflects higher complexity and more iterations needed at higher weights with greater stresses. The discrepancy between run time and relaxation factor is primarily due to the porosity initialization, a user-defined hyper-parameter. Better initialization in some runs led to faster convergence. Additionally, in some bone gaps, the oscillation loop is encountered earlier in corresponding regions (e.g., edge vs. middle regions), prompting earlier relaxation.

5.3.4. Parametric Fracture Gap Optimization Results

Next, the parametric results for the variable fracture gaps are presented. To ensure the successful operation of these parametric runs, it was necessary to adjust the user-defined variables in the optimization code, as illustrated in the flowcharts in earlier sections.

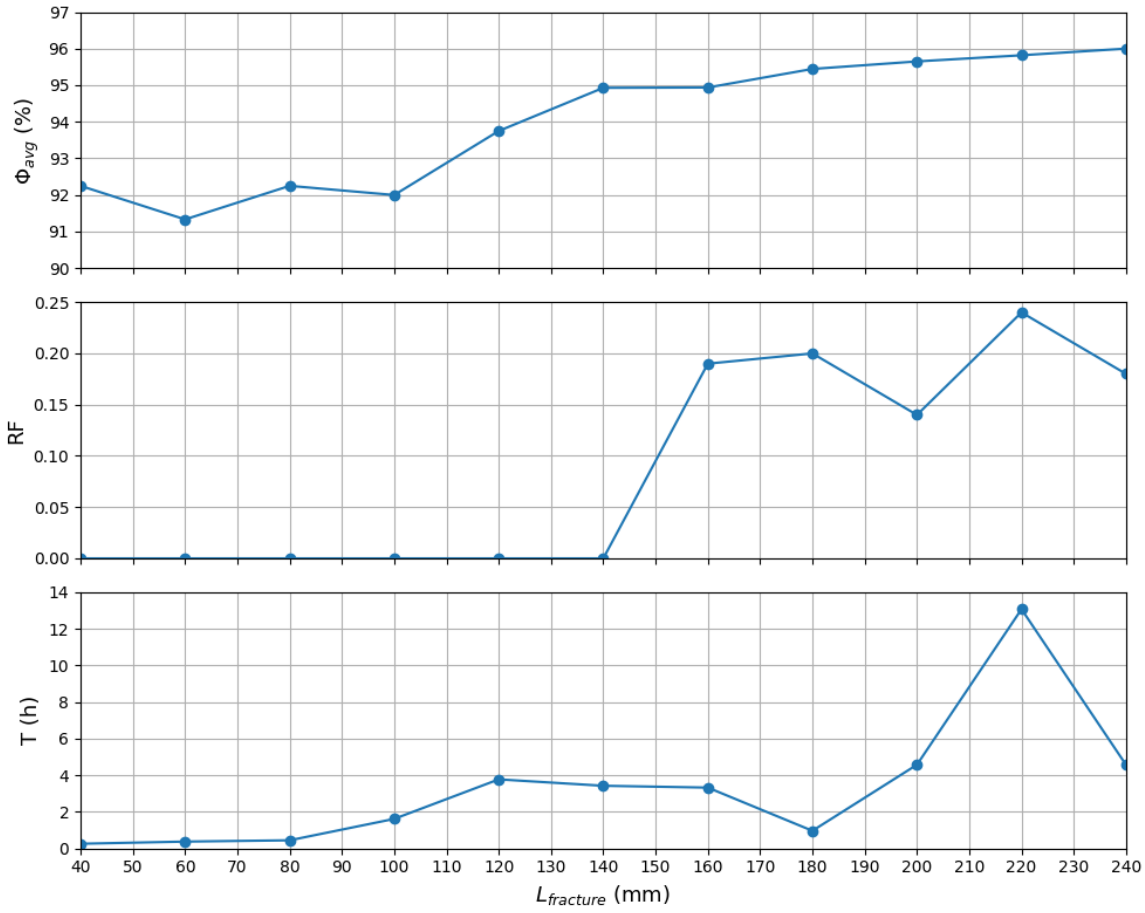

Figure 97: Parametric fracture gap results

The chart is divided into three subplots, each illustrating different parameters: average porosity (%), relaxation factor, and run time (h) as the fracture gap (mm) varies from 40 mm to 240 mm.

The first subplot displays the relationship between fracture gap size and average scaffold porosity. As the fracture gap increases, the average porosity shows an increasing trend, starting from about 92.5% at 40 mm and reaching around 96% at 240 mm. This trend suggests that larger fracture gaps allow for higher porosity, possibly due to the reduced mechanical load per unit area, allowing for a more porous scaffold

while maintaining structural integrity. However, there is some variability in the data, indicating that other factors may influence the optimal porosity, as the ones mentioned in the parametric weight results. These spikes and noise can be attributed to the non-linear relationship between modulus of elasticity (E) and porosity, homogenization inaccuracies at high porosities, variability in the sequence of upgrades, approximations in weights and force components, and the uncertainty introduced by the relaxation method.

The second subplot shows the relaxation factor given to the optimization algorithm. Initially, the relaxation factor is equal to zero for fracture gaps up to 140 mm. Beyond this point, there is a significant increase, peaking around 0.25 at 220 mm, and fluctuating around this value for larger gaps. This increase corresponds to the higher mechanical demands and the need for the algorithm to apply relaxation to achieve convergence for larger gaps.

The third subplot indicates the optimization algorithm's run time, which remains low and stable for fracture gaps up to 130 mm before increasing, peaking at about 13 hours for 220 mm, corresponding to the highest relaxation factor as well. This increase reflects the higher complexity and more iterations needed for convergence at larger fracture gaps. As before, the run time does not directly correlate with the relaxation factor due to the user-defined initialization of porosity. For instance, at 180 mm, the run time was just 1 hour because the porosities were initialized exceptionally well, with actual values precisely coinciding with the initialization of 95%. Thus, a precise initialization significantly reduces computational time. If the porosity initialization is not good, then the same computational efficiency is not obtained.

Additionally, in some bone gaps, the oscillation threshold was set to 2 (meaning if a porosity value is encountered three times, the algorithm considers it in a loop and applies relaxation). This empirical setting was found not to compromise the integrity of the analysis in these specific cases, and it was employed to reduce computational time and resources. However, using a higher oscillation threshold would yield more reliable results for new or unknown cases.

5.3.5. Summarized Parametric Reinforcement Methods Optimization Results

Next, the parametric results for the methods are presented. To ensure the success of these parametric runs, the geometry of the FEM was adjusted in stages: first with a nail, then with a plate, and finally with both. This involved a total of three runs.

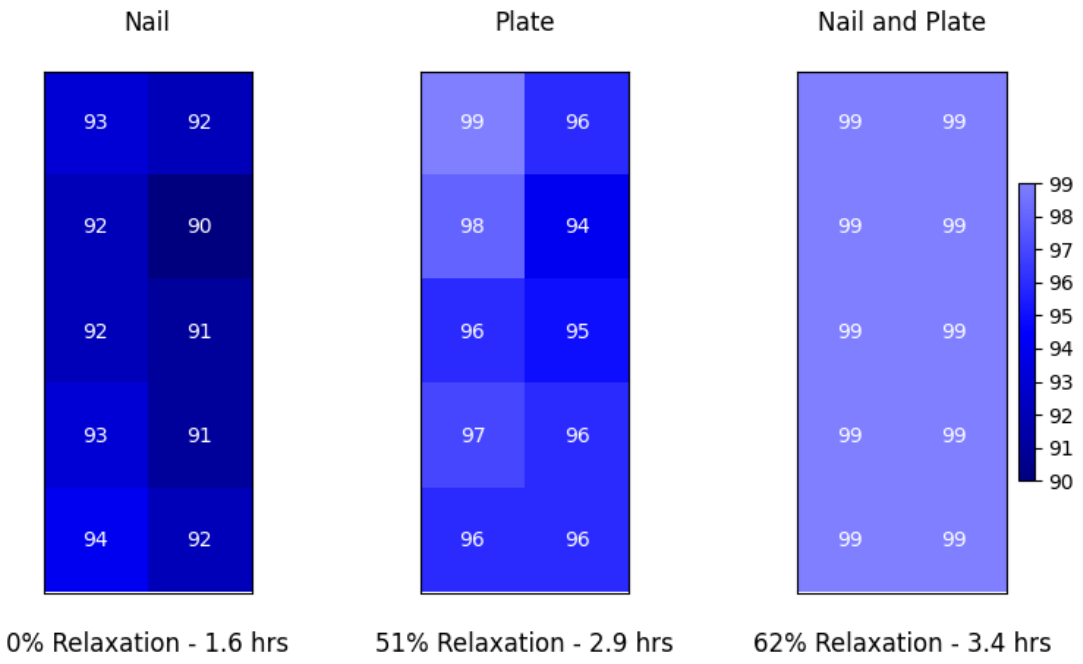

Figure 98: Stiffness maps of parametric reinforcement methods

The stiffness maps provide a visual representation of the porosity values per region for three different scaffold reinforcement methods: using a nail, a plate, and a combination of both. The porosity values are color-coded, with darker shades representing lower porosity and lighter shades indicating higher porosity. Each method is also associated with a specific relaxation percentage, which affects the overall porosity distribution.

In the first stiffness map, corresponding to the use of a nail with 0% relaxation, the porosity values vary across the regions, ranging from 90% to 94%. The top and bottom regions exhibit higher porosity values (93-94%), while the central regions have lower porosity values (90-92%). This distribution suggests that using the nail alone does not evenly distribute the mechanical load, resulting in varying porosity values to maintain structural integrity. The absence of relaxation implies that the algorithm did not need to adjust the porosity further to achieve convergence, likely because the mechanical

stresses were relatively balanced by the nail's support. Notably, the outer regions generally have higher porosity due to the way the forces are applied on the femur.

The second stiffness map, representing the plate method with 51% relaxation, shows a higher and more uniform porosity distribution compared to the nail method. Porosity values range from 94% to 99%, with the majority of regions showing values above 96%. The regions in the lateral sides also exhibit higher porosities, due to the existence of the plate near them. The topmost region reaches 99%, a value the algorithm ideally wants to exceed, but since this is not possible, relaxation is applied to achieve convergence at this value. This is due to inaccuracies in homogenization convergence, especially at such high porosities. To avoid this, the plate ideally needs compression to increase strains, given the low stresses and the capacity to withstand greater forces, but this was beyond the scope of this study.

The third stiffness map shows the combined use of both a nail and a plate with 62% relaxation. Here, the porosity values are uniformly high, at 99% across all regions. Having all regions at 99% indicates a significant issue. Beyond homogenization errors and plate compression, the scaffold would greatly benefit from being made of a material with a lower Young's modulus to develop higher strains for optimal functionality. This high relaxation percentage (62%) indicates that substantial adjustments were needed to achieve these optimal porosity values, reflecting the combined method's need to accommodate significant adjustments.

5.3.6. Real Case Scenario Detailed Optimization Results

The results of the scaffold porosities for the real case scenario from Attikon Hospital are summarized in the stiffness map below. The algorithm was extensively tested to evaluate its capabilities by applying it to this new, real-case scenario.

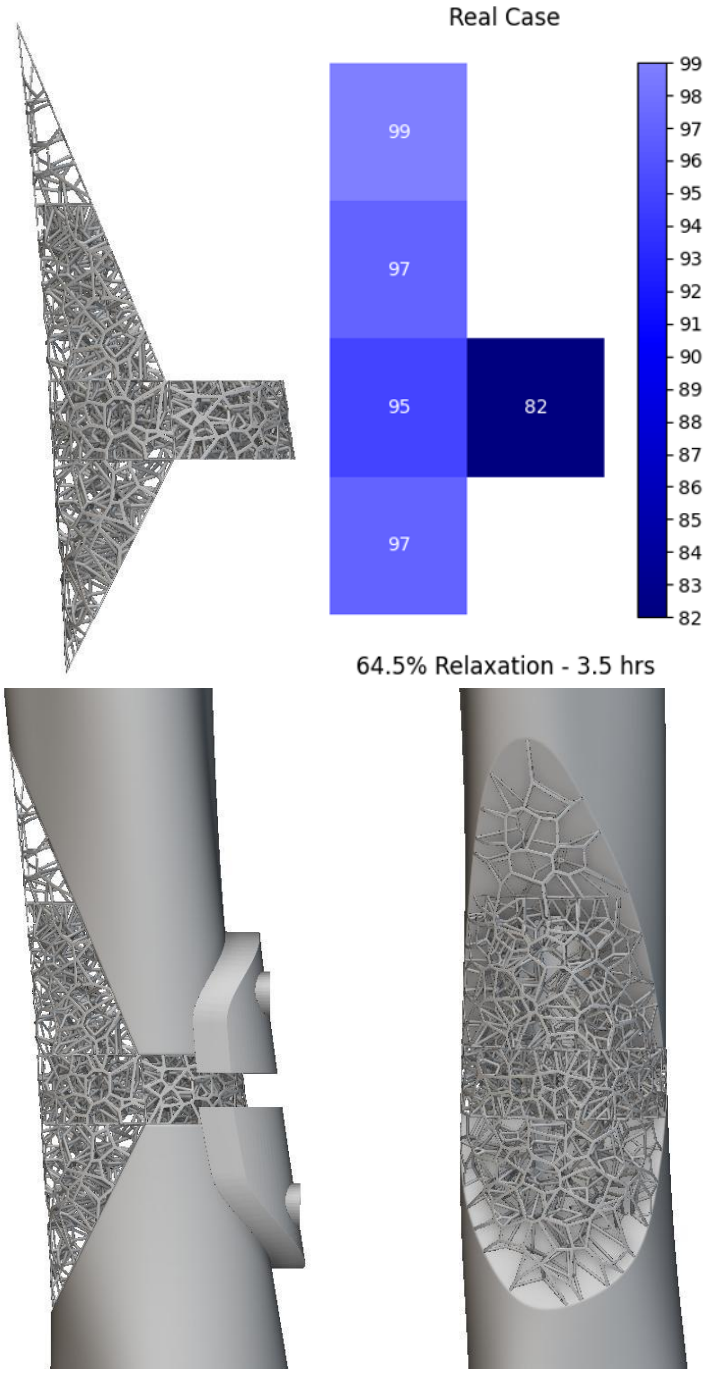

Figure 99: Stiffness map of real case scenario

The results of the FEA simulations, according to the aforementioned stiffness map, are presented below. These contours illustrate the distribution of stress and strain across the scaffold under the specified conditions, providing a detailed view of the mechanical performance and structural integrity in the real-case scenario.

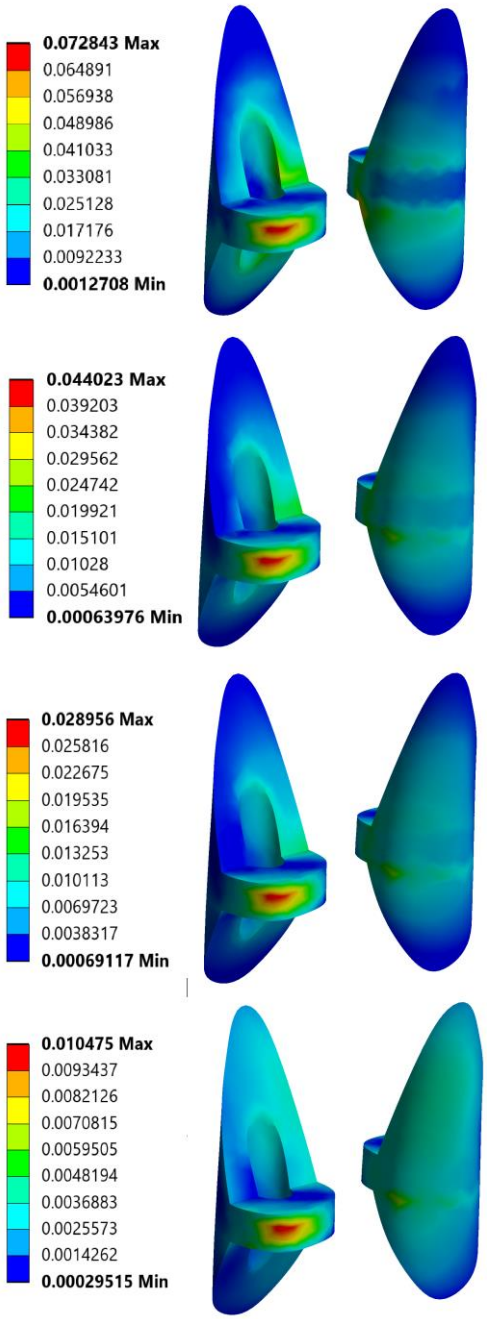

Figure 100: Scaffold strain contours – real case (granulation-cartilage-immature-mature from top to bottom)

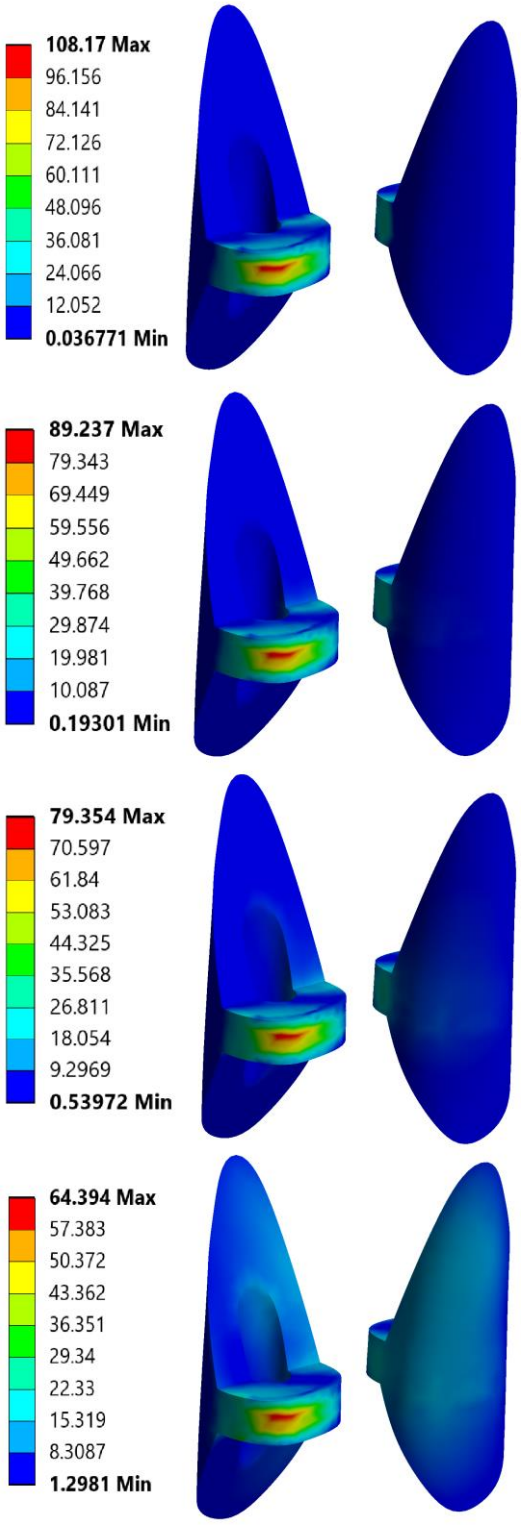

Figure 101: Scaffold stress contours – real case (granulation-cartilage-immature-mature from top to bottom)

The detailed stress-strain contours of the femur bone, illustrated alongside the scaffold integration with the whole femur, provide crucial insights into the mechanical behavior under physiological loads.

The top left region of the scaffold experiences markedly lower forces and stresses, triggering a relaxation response in the optimization algorithm. As the tissue matures and becomes more rigid, there is a noticeable decrease in the stress distribution across the scaffold, a change attributed to the scaffold's limited spatial capacity to compact further. In the initial granulation phase, despite the tissue's inherently lower Young's modulus, which typically allows more deformation and higher load to the implants, the confined scaffold area is subjected to high stress levels due to the scaffolding material's inability to distribute loads effectively. As the tissue stiffens, the role of the implants in load-bearing diminishes, with the bone itself becoming capable of bearing more load due to increased stiffness and structural integrity.

The scaffold is attached to the bone through a notably thin region, where the reduced geometrical robustness results in significant concentrations of mechanical stresses and strains. This localized increase in mechanical demands leads to reduced porosity in the area, reinforcing structural integrity where it is most compromised. The stress relaxation implemented near the brackets simulates the higher density and yield strength typically found in real-life conditions. Due to computational constraints, a detailed finite element analysis to model the denser brackets wasn't feasible. Therefore, stress relaxation was incorporated into the model by normalizing the stresses around the local maximum stress points with a factor of 0.55 as shown below.

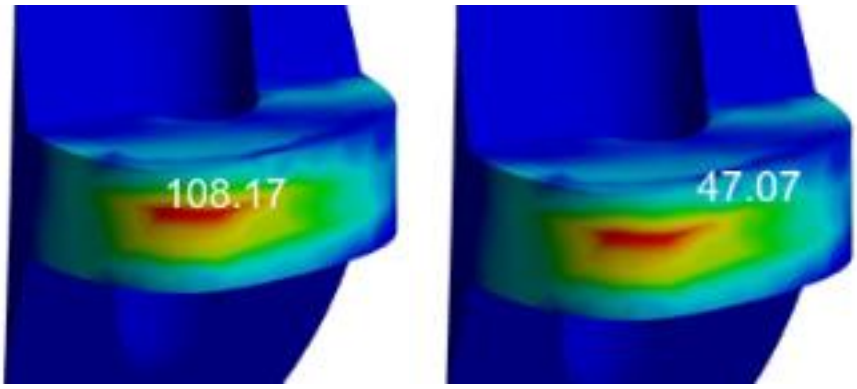

Figure 102: Stress contours near brackets at granulation stage at real case scenario

5.4. Constraints and Limitations of the Optimization Methodology

While the proposed method holds considerable promise for the analysis and optimization of 3D printed scaffolds, it is crucial to acknowledge several limitations to provide a comprehensive understanding of its current capabilities and areas for future enhancement.

One of the primary constraints is the necessity for manual definition of hyperparameters, such as the number of scaffold regions. This manual intervention can introduce variability and a potential for user error, impacting the consistency and reproducibility of the results. An automated approach using advanced algorithms or machine learning techniques could significantly enhance the robustness of this method by reducing human intervention.

Another significant limitation is the requirement for manual pre-processing of materials, attributed to the lack of direct integration between nTopology and ANSYS. This disjointed workflow complicates the setup process, extends the preparation time, and increases the risk of inconsistencies between material models used across different software platforms. Developing a seamless integration between nTopology and ANSYS would streamline operations and bolster simulation accuracy.

Currently, the model simplifies the biological environment by allowing no more than two tissue types to coexist within the scaffold. This assumption fails to capture the true complexity of biological interactions, where multiple tissue types may coexist in a random and heterogeneous manner. Future research should focus on modeling each scaffold element on a finite element basis, thus allowing for more complex material interactions and a more accurate representation of biological heterogeneity.

The exclusion of fluid dynamics modeling during osteogenesis presents another notable omission. Fluid flow is essential for nutrient transport and cell signaling during bone regeneration. Integrating fluid dynamics into the model would offer a more detailed understanding of osteogenic processes and enhance the predictive accuracy of the simulations.

Additionally, the computational demands of the method, including extended computing times and challenges related to mesh refinement and independence studies, limit its practical application, especially for large or complex scaffolds. Optimizing computational algorithms and exploring more efficient meshing techniques could mitigate these issues.

The application of empirical relaxation factors to regions with increased density introduces another approximation layer. While this approach compensates for the current limitations of finite element modeling, it does not fully capture the mechanical behavior of these regions. Developing advanced modeling techniques that can simulate the behavior of bracketed regions accurately without empirical adjustments would improve the method's precision.

Additionally, the regions have been segmented with the objective of maintaining uniform average strain throughout. While this method aims for consistency, it may inadvertently introduce uncertainties. The exploration of alternative segmentation strategies has been limited. There is potential to refine this approach by reducing the size of the regions, while simultaneously attempt to strike a more effective balance between region size and computational efficiency.

Lastly, the model has shown limitations when applied to patients of low (<55 kg) and high (>100 kg) body weights, often necessitating adjustments to manage discrepancies. This issue could be addressed by refining the yield stress calculations for all tissue stages and conducting more detailed studies on stress concentrations near scaffold brackets, for example studying element by element.

For large fracture gaps exceeding 140mm, the duration of simulations increases substantially, necessitating more frequent application of relaxation techniques. Such gaps introduce weaknesses, as the algorithm must often resort to relaxation to accommodate the extensive gap size. Addressing issues such as refining the implementation of yield stress and enhancing the modeling of stress concentrations could alleviate these computational demands.

Additionally, the current model operates under the assumption of a uniform fracture gap, lacking geometric parameterization, which does not accurately reflect the varied real-world scenarios. Although a study involving a real-case scenario has been conducted, its reliance on an unrealistically high porosity rate of 99% highlights the limitations of using a single model to represent complex clinical geometries. Expanding the research to include multiple case studies would improve the model's robustness and accuracy. Moreover, exploring various materials and additional reinforcement methods could provide deeper insights into their behavior and effectiveness in practical applications.

6. Conclusion and Future Work

This thesis has addressed the design and optimization of patient-specific 3D-printed scaffolds for the regeneration of significant femoral osseous defects, leveraging the synergy of computational modeling with advanced manufacturing techniques. The study concentrated on refining scaffold geometry and material composition, utilizing Voronoi lattices to emulate the natural trabecular structure of bone and deploying Ti-6Al-4V alloys recognized for their robust mechanical properties and biocompatibility.

An approach to material homogenization was explored, with specific advancements in merging two materials within nTopology software, providing a refined method to address the multifaceted requirements of bone regeneration. The yield stress parameters for the homogenized Voronoi structures were thoroughly assessed through comprehensive literature reviews, enriching the scaffold's design with empirical data.

Finite element analysis ensured that the scaffold designs would withstand physiological loads, promoting effective bone integration while also ensuring sufficient structural endurance during the bone healing process. Furthermore, the development and application of a tailored optimization algorithm on a CT-scanned femur was developed. This algorithm was applied to various parametric runs, such as variable patient weights, fracture gaps, and reinforcement methods.

The practical application of these methodologies was validated through a real-case scenario at Attikon Hospital. The results yielded significant variations between the scaffold’s regions, showcasing the necessity of the optimization algorithm.

Based on the constraints and limitations outlined in the previous sections, the future work for enhancing the analysis and optimization of 3D printed scaffolds can be focused to address these areas effectively. The following points highlight the key directions for future research:

- **Automation and Machine Learning Integration:** To reduce human error and variability, future efforts should concentrate on automating the definition of hyperparameters, such as the number of scaffold regions, using advanced algorithms and machine learning techniques. This approach will enhance the robustness and reproducibility of the results.
- **Software Integration:** Enhancing the workflow between nTopology and ANSYS by developing a seamless integration could significantly streamline the setup

process, reduce preparation time, and eliminate inconsistencies between material models across different software platforms.

- **Complex Biological Modeling:** Current models simplify the biological environment significantly. Future studies should aim to model each scaffold element on a finite element basis, allowing for the inclusion of multiple tissue types within a scaffold to more accurately represent the biological heterogeneity and interactions.
- **Fluid Dynamics Modeling:** Incorporating fluid dynamics into the model will provide a deeper understanding of nutrient transport and cell signaling during bone regeneration, improving the predictive accuracy of osteogenic processes.
- **Optimization of Computational Resources:** Addressing the computational demands through optimization of algorithms and exploration of more efficient meshing techniques, especially for handling large or complex scaffolds.
- **Advanced Mechanical Behavior Modeling:** Developing techniques that accurately simulate the mechanical behavior of regions with increased density without relying on empirical relaxation factors will decrease the reliance on approximations.
- **Segmentation Strategies:** Exploring and implementing alternative strategies for segmenting regions within the scaffold could mitigate uncertainties introduced by current methods. This involves refining the balance between region size and computational efficiency.
- **Handling Large and Small Patient Weights:** Refining yield stress calculations for all tissue stages and conducting detailed studies on stress concentrations, particularly for patient weights outside the typical range, will enhance model accuracy.
- **Handling Large Fracture Gaps:** For large fracture gaps, improving the implementation of yield stress and enhancing the modeling of stress concentrations are necessary to reduce the need for relaxation and shorten simulation durations.
- **Geometric Parameterization:** To more accurately reflect real-world scenarios, the model should incorporate variable fracture gaps rather than assuming uniformity. Conducting multiple case studies with different geometries and porosities will help in validating the model against complex clinical conditions.
- **Material and Reinforcement Method Exploration:** Further research into various materials and reinforcement methods.

References

[1] A. Wiese and H. C. Pape, “Bone Defects Caused by High-energy Injuries, Bone Loss, Infected Nonunions, and Nonunions,” *Orthopedic Clinics of North America*, vol. 41, no. 1. pp. 1–4, Jan. 2010. doi: 10.1016/j.ocl.2009.07.003.

[2] A. S. Cole, G. A. Hill, T. N. Theologis, C. L. M. H. Gibbons, and K. Willett, “Femoral nailing for metastatic disease of the femur: a comparison of reamed and unreamed femoral nailing.” [Online]. Available: www.elsevier.com/locate/injury

[3] J. Lu, S. C. Guo, Q. Y. Wang, J. G. Sheng, and S. C. Tao, “J-bone graft with double locking plate: A symphony of mechanics and biology for atrophic distal femoral non-union with bone defect,” *J Orthop Surg Res*, vol. 15, no. 1, Apr. 2020, doi: 10.1186/s13018-020-01636-3.

[4] D. Abdulaziz, A. D. Anastasiou, V. Panagiotopoulou, E. M. Raif, P. V. Giannoudis, and A. Jha, “Physiologically engineered porous titanium/brushite scaffolds for critical-size bone defects: A design and manufacturing study,” *J Mech Behav Biomed Mater*, vol. 148, Dec. 2023, doi: 10.1016/j.jmbbm.2023.106223.

[5] A. K. Nandakumaran, “An Overview of Homogenization,” 2007. [Online]. Available: https://www.researchgate.net/publication/228808003

[6] Z. W. Hou, M. Xu, K. Zheng, and X. C. Yu, “Classification and reconstruction of femoral bone defect in the revision of aseptic loosening of distal femoral endoprostheses: a 10-year multicenter retrospective analysis,” *BMC Musculoskelet Disord*, vol. 23, no. 1, Dec. 2022, doi: 10.1186/s12891-022-05885-7.

[7] O. Jones, “The Femur.” Accessed: Jun. 11, 2024. [Online]. Available: https://teachmeanatomy.info/lower-limb/bones/femur/#section-66688e6c08e5b

[8] S. M. Chang, Z. H. Wang, K. W. Tian, G. X. Sun, X. Wang, and Y. F. Rui, “A sophisticated fracture classification system of the proximal femur trochanteric region (AO/OTA-31A) based on 3D-CT images,” *Front Surg*, vol. 9, Aug. 2022, doi: 10.3389/fsurg.2022.919225.

[9] S. Bernoudina, “Winquist classification of femoral shaft fractures.” Accessed: Jun. 11, 2024. [Online]. Available: https://radiopaedia.org/cases/winquist-classification-of-femoral-shaft-fractures

[10] F. Seinsheimer, “Fractures of the distal femur,” *Clin Orthop Relat Res*, vol. 3, pp. 169–179, 1980.

[11] D. A. Ibrahim and N. D. Fernando, “Classifications In Brief: The Paprosky Classification of Femoral Bone Loss,” *Clin Orthop Relat Res*, vol. 475, no. 3, pp. 917–921, Mar. 2017, doi: 10.1007/s11999-016-5012-z.

[12] Y. B. Ibrahim *et al.*, “Risk factors, classification, and operative choices of femur fractures at a Tertiary Hospital: first report from Somalia,” *Sci Rep*, vol. 13, no. 1, Dec. 2023, doi: 10.1038/s41598-023-39671-9.

[13] A. C. Hollis, S. R. Ebbs, and F. N. Mandari, “The epidemiology and treatment of femur fractures at a northern tanzanian referral centre,” *Pan African Medical Journal*, vol. 22, Dec. 2015, doi: 10.11604/pamj.2015.22.338.8074.

[14] F. D. Cojocaru, V. Balan, and L. Verestiuc, “Advanced 3D Magnetic Scaffolds for Tumor-Related Bone Defects,” *International Journal of Molecular Sciences*, vol. 23, no. 24. MDPI, Dec. 01, 2022. doi: 10.3390/ijms232416190.

[15] Direct Orthopedic Care, “Strategies to Help Heal Your Broken Bones.” Accessed: Jun. 12, 2024. [Online]. Available: https://www.directorthocare.com/strategies-to-help-heal-your-broken-bones/

[16] J. R. Sheen, A. Mabrouk, and V. V. Garla, “Fracture Healing Overview,” *National Library of Medicine*, Apr. 2023, Accessed: Jun. 12, 2024. [Online]. Available: https://www.ncbi.nlm.nih.gov/books/NBK551678/

[17] T. Yuling, C. Xiao, Z. Junxia, J. Jun, and L. Xinghua, “Effect of different composite plates on the healing of femoral fractures,” *J Mech Behav Biomed Mater*, vol. 151, Mar. 2024, doi: 10.1016/j.jmbbm.2023.106356.

[18] A. Soni and B. Singh, “Design and Analysis of Customized Fixation Plate for Femoral Shaft,” *Indian J Orthop*, vol. 54, no. 2, pp. 148–155, Apr. 2020, doi: 10.1007/s43465-019-00025-1.

[19] G. Chandra, A. Pandey, and S. Pandey, “Design of a biodegradable plate for femoral shaft fracture fixation,” *Med Eng Phys*, vol. 81, pp. 86–96, Jul. 2020, doi: 10.1016/j.medengphy.2020.05.010.

[20] K. Garala *et al.*, “Distal femoral fractures: A comparison between single lateral plate fixation and a combined femoral nail and plate fixation,” *Injury*, vol. 53, no. 2, pp. 634–639, Feb. 2022, doi: 10.1016/j.injury.2021.11.011.

[21] S. J. Song, W. J. Song, D. K. Kim, and D. K. Bae, “Treatment of distal femur fractures with locking plates: Comparison of periprosthetic fractures above total knee arthroplasty and non-periprosthetic fractures,” *National Library of Medicine*, 2014.

[22] P. V. Giannoudis, H. C. Pape, and M. Schütz, “MIO - Bridge plating (LISS or LCP).” Accessed: Jun. 12, 2024. [Online]. Available: https://surgeryreference.aofoundation.org/orthopedic-trauma/adult-trauma/femoral-shaft/segmental-intact-distal-1-3-fractures/mio-bridge-plating-liss-or-lcp

[23] W. M. Ricci, C. Bellabarba, B. Evanoff, D. Herscovici, T. DiPasquale, and R. Sanders, “Retrograde Versus Antegrade Nailing of Femoral Shaft Fractures,” 2001.

[24] D. Horwitz, “ANTEGRADE VS. RETROGRADE FEMORAL NAILING,” Phoenix, 2013.

[25] N. Hussain *et al.*, “Antegrade versus retrograde nailing techniques and trochanteric versus piriformis intramedullary nailing entry points for femoral shaft fractures: A systematic review and meta-Analysis,” *Canadian Journal of Surgery*, vol. 60, no. 1, pp. 19–29, Feb. 2017, doi: 10.1503/cjs.000616.

[26] SYNTHES, “Expert Retrograde / Antegrade Femoral Nail (R/AFN).” Accessed: Jun. 12, 2024. [Online]. Available: https://www.aofoundation.org/approved/approvedsolutionsfolder/2004/expert-retrograde--antegrade-femoral-nail-rafn#tab=instruments;

[27] SYNTHES, “EXPERT Nailing System Technique Guide.”

[28] B. J. Passias *et al.*, “Treatment of Distal Femur Fractures with a Combined Nail-Plate Construct: Techniques and Outcomes,” 2021. [Online]. Available: www.begellhouse.com

[29] J. L. Wilson, M. Squires, M. McHugh, J. Ahn, A. Perdue, and M. Hake, “The geriatric distal femur fracture: nail, plate or both?,” *European Journal of Orthopaedic Surgery and Traumatology*, vol. 33, no. 5, pp. 1485–1493, Jul. 2023, doi: 10.1007/s00590-022-03337-5.

[30] O. Başci, A. Karakaşli, E. Kumtepe, O. Güran, and H. Havitçioğlu, “Combination of anatomical locking plate and retrograde intramedullary nail in distal femoral fractures: Comparison of mechanical stability,” *Eklem Hastaliklari ve Cerrahisi*, vol. 26, no. 1, pp. 21–26, 2015, doi: 10.5606/ehc.2015.06.

[31] N. Shahrubudin, T. C. Lee, and R. Ramlan, “An overview on 3D printing technology: Technological, materials, and applications,” in *Procedia Manufacturing*, Elsevier B.V., 2019, pp. 1286–1296. doi: 10.1016/j.promfg.2019.06.089.

[32] L. Zhao *et al.*, “Bionic design and 3D printing of porous titanium alloy scaffolds for bone tissue repair,” *Compos B Eng*, vol. 162, pp. 154–161, Apr. 2019, doi: 10.1016/j.compositesb.2018.10.094.

[33] E. Maevskaia, C. Ghayor, I. Bhattacharya, J. Guerrero, and F. E. Weber, “TPMS Microarchitectures for Vertical Bone Augmentation and Osteoconduction: An In Vivo Study,” *Materials*, vol. 17, no. 11, p. 2533, May 2024, doi: 10.3390/ma17112533.

[34] L. Chao *et al.*, “Design of porous structure based on the Voronoi diagram and stress line for better stress shielding relief and permeability,” *Journal of Materials Research and Technology*, vol. 25, pp. 1719–1734, Jul. 2023, doi: 10.1016/j.jmrt.2023.05.282.

[35] G. Wang *et al.*, “Design and Compressive Behavior of Controllable Irregular Porous Scaffolds: Based on Voronoi-Tessellation and for Additive Manufacturing,” *ACS Biomater Sci Eng*, vol. 4, no. 2, pp. 719–727, Feb. 2018, doi: 10.1021/acsbiomaterials.7b00916.

[36] Z. Li, Q. Wang, and G. Liu, “A Review of 3D Printed Bone Implants,” *Micromachines*, vol. 13, no. 4. MDPI, Apr. 01, 2022. doi: 10.3390/mi13040528.

[37] X. Hou, Z. Liu, B. Wang, W. Lv, X. Liang, and Y. Hua, “Stress-strain curves and modified material constitutive model for Ti-6Al-4V over thewide ranges of strain rate and temperature,” *Materials*, vol. 11, no. 6, Jun. 2018, doi: 10.3390/ma11060938.

[38] Q. Li, Q. Li, S. Lu, and D. Pan, “Spatial Topological Structure Design of Porous Ti–6Al–4V Alloy with Low Modulus and Magnetic Susceptibility,” *Nanomaterials*, vol. 13, no. 24, Dec. 2023, doi: 10.3390/nano13243113.

[39] X. Yue, J. Shang, M. Zhang, B. Hur, and X. Ma, “Additive manufacturing of high porosity magnesium scaffolds with lattice structure and random structure,” *Materials Science and Engineering: A*, vol. 859, Nov. 2022, doi: 10.1016/j.msea.2022.144167.

[40] M. Shinde, I. E. Ramirez-Chavez, D. Anderson, J. Fait, M. Jarrett, and D. Bhate, “Towards an Ideal Energy Absorber: Relating Failure Mechanisms and Energy Absorption Metrics in Additively Manufactured AlSi10Mg Cellular Structures under Quasistatic Compression,” *Journal of Manufacturing and Materials Processing*, vol. 6, no. 6, Dec. 2022, doi: 10.3390/jmmp6060140.

[41] A. Efstathiadis, I. Symeonidou, K. Tsongas, E. K. Tzimtzimis, and D. Tzetzis, “3D Printed Voronoi Structures Inspired by Paracentrotus lividus Shells,” *Designs (Basel)*, vol. 7, no. 5, Oct. 2023, doi: 10.3390/designs7050113.

[42] Y. Yuan *et al.*, “Deformation and failure of additively manufactured Voronoi foams under dynamic compressive loadings,” *Eng Struct*, vol. 284, Jun. 2023, doi: 10.1016/j.engstruct.2023.115954.

[43] E. Andreassen and C. S. Andreasen, “How to determine composite material properties using numerical homogenization,” *Comput Mater Sci*, vol. 83, pp. 488–495, Feb. 2014, doi: 10.1016/j.commatsci.2013.09.006.

[44] V. Karageorgiou and D. Kaplan, “Porosity of 3D biomaterial scaffolds and osteogenesis,” *Biomaterials*, vol. 26, no. 27. Elsevier BV, pp. 5474–5491, 2005. doi: 10.1016/j.biomaterials.2005.02.002.

[45] D. Lacroix and P. J. Prendergast, “A mechano-regulation model for tissue differentiation during fracture healing: analysis of gap size and loading,” 2002.

[46] H. Isaksson, W. Wilson, C. C. van Donkelaar, R. Huiskes, and K. Ito, “Comparison of biophysical stimuli for mechano-regulation of tissue differentiation during fracture healing,” *J Biomech*, vol. 39, no. 8, pp. 1507–1516, 2006, doi: 10.1016/j.jbiomech.2005.01.037.

[47] ANSYS, “Volumetric and Deviatoric Strain Volumetric and Deviatoric Behavior.”

[48] Σ. Πολιτικων Μηχανικων Εργαστηριο Εδαφομηχανικης, “Experimental Study of the Anisotropic Flow Deformation and Critical State of Sand ΕΘΝΙΚΟ ΜΕΤΣΟΒΙΟ ΠΟΛΥΤΕΧΝΕΙΟ,” 2020.

[49] A. Chauhan and A. D. Bhatt, “Effect of unit cell features on mechanical properties of lattice structures at constant porosity levels: A general mixture rule based interpretation,” *Mater Today Proc*, vol. 56, pp. 1–8, Jan. 2022, doi: 10.1016/j.matpr.2021.11.323.

[50] S. Sorohan, D. M. Constantinescu, M. Sandu, and A. G. Sandu, “On the homogenization of hexagonal honeycombs under axial and shear loading. Part I: Analytical formulation for free skin effect,” *Mechanics of Materials*, vol. 119, pp. 74–91, Apr. 2018, doi: 10.1016/j.mechmat.2017.09.003.

[51] W. Miller, C. W. Smith, and K. E. Evans, “Honeycomb cores with enhanced buckling strength,” *Compos Struct*, vol. 93, no. 3, pp. 1072–1077, 2011, doi: 10.1016/j.compstruct.2010.09.021.

[52] V. Kaajakari, “Silicon as an anisotropic mechanical material-a tutorial.” [Online]. Available: http://www.kaajakari.net/

[53] M. S. Ghiasi, J. E. Chen, E. K. Rodriguez, A. Vaziri, and A. Nazarian, “Computational modeling of human bone fracture healing affected by different conditions of initial healing stage,” *BMC Musculoskelet Disord*, vol. 20, no. 1, Nov. 2019, doi: 10.1186/s12891-019-2854-z.

[54] H. J. Kim, S. H. Chang, and H. J. Jung, “The simulation of tissue differentiation at a fracture gap using a mechano-regulation theory dealing with deviatoric

strains in the presence of a composite bone plate," *Compos B Eng*, vol. 43, no. 3, pp. 978–987, Apr. 2012, doi: 10.1016/j.compositesb.2011.09.011.

[55] materialise, "Design Guidelines for Metal 3D Printing." Accessed: Jun. 17, 2024. [Online]. Available: https://www.materialise.com/en/academy/industrial/design-am/stainless-steel-ss316l

[56] A. W. Ayeni, "Empirics of Standard Deviation," 2014, doi: 10.13140/2.1.1444.6729.

[57] A. Efstathiadis, I. Symeonidou, K. Tsongas, E. K. Tzimtzimis, and D. Tzetzis, "3D Printed Voronoi Structures Inspired by Paracentrotus lividus Shells," *Designs (Basel)*, vol. 7, no. 5, Oct. 2023, doi: 10.3390/designs7050113.

[58] X. Yue, J. Shang, M. Zhang, B. Hur, and X. Ma, "Additive manufacturing of high porosity magnesium scaffolds with lattice structure and random structure," *Materials Science and Engineering: A*, vol. 859, Nov. 2022, doi: 10.1016/j.msea.2022.144167.

[59] W. Pirker and R. Katzenschlager, "Gait disorders in adults and the elderly: A clinical guide," *Wiener Klinische Wochenschrift*, vol. 129, no. 3–4. Springer-Verlag Wien, pp. 81–95, Feb. 01, 2017. doi: 10.1007/s00508-016-1096-4.

[60] M. Björnsdóttir, "Influence of Muscle Forces on Stresses in the Human Femur."

[61] Basicmedical Key, "Anteromedial Thigh." Accessed: Jun. 20, 2024. [Online]. Available: https://basicmedicalkey.com/anteromedial-thigh/

[62] J. A. Simões, M. A. Vaz, S. Blatcher, and M. Taylor, "Influence of head constraint and muscle forces on the strain distribution within the intact femur," 2000. [Online]. Available: www.elsevier.com/locate/medengphy

Appendix A.1 – Optimization Code

Appendix A.2 – Results Visualization Code